University of South Carolina
Scholar Commons

Theses and Dissertations

2017

High Resolution Gravity, Helicopter Magnetic, and Electromagnetic Study, Haile Gold Mine, South Carolina

Saad Saud Alarifi
University of South Carolina

Follow this and additional works at: https://scholarcommons.sc.edu/etd

 Part of the Geology Commons

Recommended Citation

Alarifi, S. S.(2017). *High Resolution Gravity, Helicopter Magnetic, and Electromagnetic Study, Haile Gold Mine, South Carolina.* (Master's thesis). Retrieved from https://scholarcommons.sc.edu/etd/4135

This Open Access Thesis is brought to you by Scholar Commons. It has been accepted for inclusion in Theses and Dissertations by an authorized administrator of Scholar Commons. For more information, please contact dillarda@mailbox.sc.edu.

www.manaraa.com

High Resolution Gravity, Helicopter Magnetic, and Electromagnetic Study, Haile Gold Mine, South Carolina

by

Saad Saud Alarifi

Bachelor of Science
King Saud University, 2010

Submitted in Partial Fulfillment of the Requirements

For the Degree of Master of Science in

Geological Sciences

College of Arts and Sciences

University of South Carolina

2017

Accepted by:

James N. Kellogg, Director of Thesis

Camelia C. Knapp, Reader

Gene M. Yogodzinski, Reader

Cheryl L. Addy, Vice Provost and Dean of the Graduate School

www.manaraa.com

© Copyright by Saad Saud Alarifi, 2017
All Rights Reserved.

www.manaraa.com

DEDICATION

First of all, thanks to almighty God who has given me strength throughout my life to complete this thesis.

I gratefully thank my parents, brother, and sister. Special thanks to my lovely wife Dona and son Ryan for standing with me during the entire period of my studies.

www.manaraa.com

ACKNOWLEDGEMENTS

I would like to thank Dr. James Kellogg for ongoing support in his capacity as a mentor and adviser, as well as my other M.S. thesis committee members Dr. Camelia Knapp, and Dr. Gene Yogodzinski.

Furthermore I would to thank my colleagues who helped me whenever I had questions. Thanks for the support of the staff of the Andean Geophysical Laboratory.

I would like to thank James Berry, OceanaGold Exploration Head Geologist, and Ken Gillian, for the high resolution gravity, magnetic and electromagnetic datasets and the regional geological map.

Also, thanks go to Geosoft Inc. for donating academic licenses for the Oasis montaj and 2-D GMSYS software.

I would not have had this opportunity without the full scholarship support from King Saud University.

www.manaraa.com

ABSTRACT

The goal of this research was to calibrate and test geophysical methods for the detection of disseminated sulfides in the area of the Haile Gold Mine, South Carolina. The work focused on the calibration of high resolution gravity, and helicopter electromagnetic (EM) and magnetic data provided by OceanaGold. While high resolution potential field data (gravity and magnetics) has not been proven to be effective at small scales in exploration for disseminated sulfides, there is a strong regional correlation between high amplitude gravity and magnetic anomalies and the most productive gold mines in the Carolina terrane. Helicopter EM methods have been shown to be effective in distinguishing sedimentary from volcanic-dominated sediments in the metamorphic rocks of the Carolina terrane. The interpretation of the gravity and magnetic data utilized tilt derivatives, reduced to pole anomalies (RTP), shaded relief, Power spectrum, Analytical signal, Source parameter imaging (SPI), 3-D Euler deconvolution, upward continuation, and 2-D forward density modeling. The most surprising result was that over the Haile Mine, the residual gravity anomalies, tilt derivatives, and analytic signal show positive anomalies correlated with the location of a disseminated ore body. The gravity field over the ore body can be interpreted as produced by 4% pyrite and molybdenite. Electromagnetic (EM) anomalies are also spatially associated with the Haile ore bodies. Cultural signals in the EM data can be minimized with high pass filtering. The edges of a granite pluton are clearly illuminated by the shaded relief, tilt derivative, Euler

www.manaraa.com

deconvolution, and analytic signal of the high resolution magnetic field. The RTP magnetic field shows NW-trending Jurassic dikes as well as ENE-trending Alleghanian dikes. An oval pattern in the magnetic SPI outlines the Brewer gold mine area.

www.manaraa.com

TABLE OF CONTENTS

www.manaraa.com

www.manaraa.com

LIST OF TABLES

www.manaraa.com

LIST OF FIGURES

www.manaraa.com

www.manaraa.com

www.manaraa.com

www.manaraa.com

www.manaraa.com

CHAPTER 1

INTRODUCTION

1.1 Hypothesis

- The meta-volcanic rocks of the Haile Mine area (Persimmon Fork Formation) are characterized by slightly higher gravity, magnetic, and conductivity anomalies than the meta-sedimentary rocks of the Haile Mine area (Richtex Formation).
- The largest magnetic anomalies are associated with Jurassic mafic dikes.
- Positive magnetic and EM anomalies are spatially associated with the Haile ore bodies. These are produced by molybdenite, pyrite, or other disseminated ore associated minerals.

1.2 Background

The Haile Gold Mine property, the Brewer gold mine to the northeast, and the Ridgeway gold mine to the southwest, are located in the Carolina terrane (Figure 1.1), part of a volcanic island arc that formed off the coast of Gondwana, hundreds of miles from North America (Laurentia). The Carolina terrane extends for more than 500 km from Virginia to Georgia, with a maximum width of 140km in central North Carolina. All the gold deposits are hosted in similar geologic settings near the contact between metamorphosed volcanoclastic and metamorphosed sedimentary rocks of Neoproterozoic to Early Cambrian age. The Carolina terrane was accreted during Paleozoic time during

www.manaraa.com

the Acadian-Neoacadian orogenic event. An intrusive magmatic and metamorphic overprint is found mostly in the western portions of the Carolina terrane as a result of oblique accretion with Laurentia, progressing from north to south. The Carolinia terrane is separated from the Appalachian Inner Piedmont by the Central Piedmont low-angle shear zone (Dennis and Wright 1997; Hibbard 2000; Hibbard et al. 2002).

The Carolina terrane is considered unrelated to other Appalachian terranes because of differences in age and composition. Cambrian-age rocks with limestone and shale formations comprise much of the Appalachian terranes. The Carolina terrane contains low-grade meta-igneous and meta-sedimentary rocks of Neoproterozoic to Late Cambrian age (Secor et al., 1983). The Carolina terrane is composed of greenschist facies metamorphosed sedimentary and volcanic rocks bounded by amphibolite grade rocks of the Charlotte belt to the northwest and the Kiokee belt to the southeast **(**Feiss, 1982), Figure 1.2.

By U-Pb dating of zircon and the fossil evidence, the Carolina terrane is dated as late Neoproterozoic to Cambrian age, 630 to 520 Ma (Hibbard et al. 2002). Rock type transitions from felsic to mafic submarine volcanics (Persimmon Fork Formation) and mudstones to turbidite clastics (Ritchtex Formation) suggest an intra-arc basin tectonic setting (Ayuso et.al., 2005). U-Pb zircon dating of the meta-sediment and meta-volcanic units at the Haile mine give an age range of 530 to 550 Ma, and Rhenium-Osmium dating of the molybdenite minerals, and $^{40}Ar/^{39}Ar$ dating of biotite indicate that the mineralization occurred from 552 to 558 Ma (Mobley et al., 2014).

www.manaraa.com

In the eastern Carolina terrane in South Carolina, the Long Town granite dated at 550 Ma intrudes the Persimmon Fork Formation. Dennis and Wright (1997) reported that plutonic mafic- ultramafic complexes intruded the northwestern Carolina terrane along the Piedmont suture. U-Pb gives ages for these complexes between 580 to 535Ma. They are therefore not a result of accretion to North America, but occurred as a result of arc rifting when the Carolinia terrane was located in peri-Gondwana.

The regional magnetic map of South Carolina is divided into two provinces along a line known as the Fall Line: the Appalachian piedmont province is characterized by highly deformed and metamorphosed sedimentary and igneous rocks of Precambrian and Paleozoic age, and the Atlantic coastal plain sediments province consists of semi-consolidated young sedimentary rocks of upper Cretaceous to recent age (Bell et al, 1974; Snoke et al., 1977; Popenoe and Zietz 1977). The Coastal plain sand overlies older igneous and metamorphic rocks. Popenoe and Zietz (1977) compiled a coastal plain thickness map based on the well and seismic data (figure A.1). The coastal plain thickness increases to the southeast. Near the Fall line, the basement rocks have a similar composition to the Piedmont rocks (Daniels 1974). In general, mafic rocks are more magnetic than felsic varieties, but this is “not always true” (Popenoe and Zietz 1977).

West of the Fall Line where the sources are exposed, two granite plutons (Liberty Hill and Pageland) exhibit high magnetic and low gravity anomalies. Based on their magnetic signature, these plutons were interpreted to have been emplaced after the last regional metamorphic event. Northwest magnetic trends over the Atlantic coastal plain are correlated with diabase dikes of Jurassic or Triassic age (Popenoe and Zietz 1977). Figure A.2 is a dike distribution map from Popenoe and Zietz (1977).

www.manaraa.com

1.3 Stratigraphy

Three metavolcanic-dominated sequences of Neoproterozoic to Cambrian age (Figure 1.3) comprise the bulk of the Carolina terrane. These sequences formed separately in distinct tectonic settings (Snider et al. 2014, Hulse 2008).The Virgilian sequence is the oldest, from north-central North Carolina to South-central Virginia, interpreted to have been deposited in shallow water (Hibbard et al. 2002).

The Albemarle sequence extending from North Carolina to Georgia is the youngest, and it contains the units that host most of the known gold deposits and most of the new discoveries. It is estimated to be greater than 15 km thick (Nora et al 2012, Hibbard et al 2002). The sequence is covered by onlapping sediments of the Atlantic Coastal Plain which run right up against the gold deposits in the vicinity of Haile and Brewer (Foley et al. 2002).

The Albemarle sequence in South Carolina is composed of four formations. The metasedimentary rocks, which consist of 5 km of the Richtex, Emory, and Asbill Pond formations overlie a 3-km thick sequence of the Persimmon Fork Formation (Hibbard et al 2002; Mobely et al. 2014). The Persimmon Fork Formation is mainly composed of felsic volcanic rocks, originally rhyodacitic to andesitic in composition. The main minerals within this unit are quartz, albite, white mica, chlorite, and biotite; deposited in a subaerial environment (Snider et al 2014). The Richtex Formation components are beds of thin metamorphosed siltstones, mudstones, wackestones, and turbidite deposits. The main minerals within this unit are quartz, white pyrite (generally less than 10 percent), mica (up to 50 Percent), pyrrhotite, and chlorite, with lesser amounts of calcite and biotite

www.manaraa.com

when strongly mineralized, the metasiltstone is highly silicified (Dennis and Wright 1997; Hibbard et al., 2002; Mobely et al., 2014).

The Richtex Formation and Emory Formation are equivalent in age. Regional mapping shows that the Asbill pond is separated from the underlying Richtex by an angular unconformity (Hibbard et al 2002). The Persimmon Fork appears to be conformable with the overlaying Richtex and Emory Fm., based on regional map and drill core observations (Mobley et al. 2014). The Richtex Formation occurs to the northwest, while the Asbill pond Formation to the southeast with a regional anticline of Persimmon Fork Formation separating them (Hibbard et al. 2002; Mobley et al 2014).

The Richtex and Persimmon Fork formations are the main rock elements found in the study area. These formations are dissected by northwest diabase dikes, and intruded by Carboniferous granites. Coastal Plain sediments and Saprolite of variable thickness covered the units (Snider et al 2014). The Coastal Plain sands thin toward the west and have a thickness of 23 m in the Haile area. Thick saprolite, a structureless, unconsolidated, kaolin-rich, red-brown to white residuum has been derived from weathering of the underlying bedrock. The saprolitic cover of the Haile site is thick over the metavolcanic unit and thin over the metasedimentary unit, Figure 1.4 (Mobley et al. 2014; Berry et al 2015).

1.4 Mineralization

The deposit at Haile consists of multiple discontinuous ore bodies. The gold mineralization is disseminated and associated with pyrite, pyrrhotite and molybdenite. The mineralization occurs in silica rich rocks. The ore bodies trend northeast-southwest with the trend of the Carolina Terrane. Within the mineralization zones, quartz is

www.manaraa.com

dominant, pyrite is lesser (3 to 10 percent), and sericite is variable. Moving away from the mineralized zone, quartz and pyrite decrease while sericite increases in abundance (Snider et al 2014, Hulse et al. 2008). In North Carolina at Deep River Gold, based on the vertical drill holes at depth between 92 and 236 m from Carolina Gold crop., Ltd, the gold mineralization coincides with a zone of silicified rock, and dips shallowly to the southwest (Rapprecht 2010). The Richtex Formation is the main host rock for gold mineralization, where the gold deposits are located at or near the contact between felsic volcanics and sedimentary sequences.

The Brewer mine is interpreted as a high sulfide epithermal porphyry while the Haile mine is interpreted as a low sulfide epithermal pyrite deposit, from subvolcanic intrusive to subaerial deposits, (Nora et al., 2012**).** Berry et al. (2016) indicated that the Haile mine shows a low sulfide signature with the potassium feldspar present, but the disseminated ore suggests a high sulfide deposit.

The Re-Os age of mineralization at the Haile Mine is 548.7±2 Ma, close to the age of the host rocks at Haile and Ridgeway, 553±2 and 556±2 Ma, respectively (Mobely et al 2014). The Haile ore is interpreted as a low-sulfidization style, hydrothermal deposit driven by magmatism not by the later metamorphic events. Thus, the mineralization occurred while the Carolina terrane was still located in a peri-Gondwana site (Mobely et al 2014).

1.5 Structure

The Carolina terrane is bounded by late Paleozoic shear zones, the Modoc between the Carolina Slate Belt and Kiokee Belt, the Nutbush Creek, and the Gold Hill shear zones (Figure 1.3, Foley et al., 2012).

www.manaraa.com

Thin Alleghanian age (311 Ma) alkaline dikes less than 2 m wide, some of them lamprophyric in composition, are observed rarely in the area (Mobley et al 2014). These ages are similar to the 314 ± 2 Ma age of the Dutchman Creek Gabbro that extends 500 km from North Carolina to Georgia. The correspondence of the ages indicates that the lamprophyre dikes and the gabbro were produced during an episode of mafic magmatism that occurred in the Haile area during the early Alleghanian (Mobley et al. 2014, Berry et al. 2016). The Carboniferous (300 Ma) Pageland and Liberty Hill granites intruded within a few miles of the mine area (Tuten 2013).

Many folds in the Haile Mine area are asymmetric with moderately dipping northwestern limbs and steep to overturned southeastern limbs, (Mobley et al., 2014; Snider et al., 2014), and the foliation in the region strikes east-northeast. NW-trending diabase dikes of Jurassic age crosscut the Haile units. The diabase dikes vary from a few cm to 40 m in thickness.

Figure 1.1: Gold mine locations in the Carolina Terrane from (Hibbard et al. 2002). (Mobley et al., 2014)

www.manaraa.com

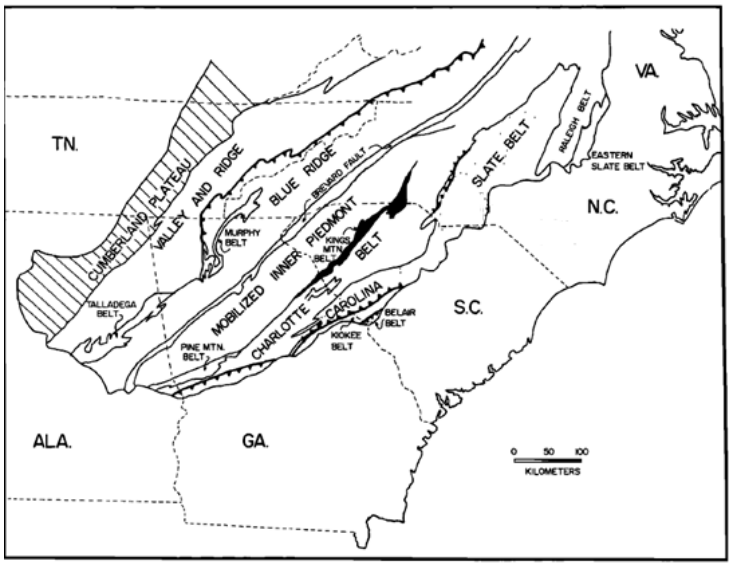

Figure 1.2: Map of the southeastern United States showing the Carolina and Appalachian terranes; modified after Vick et al. (1987).

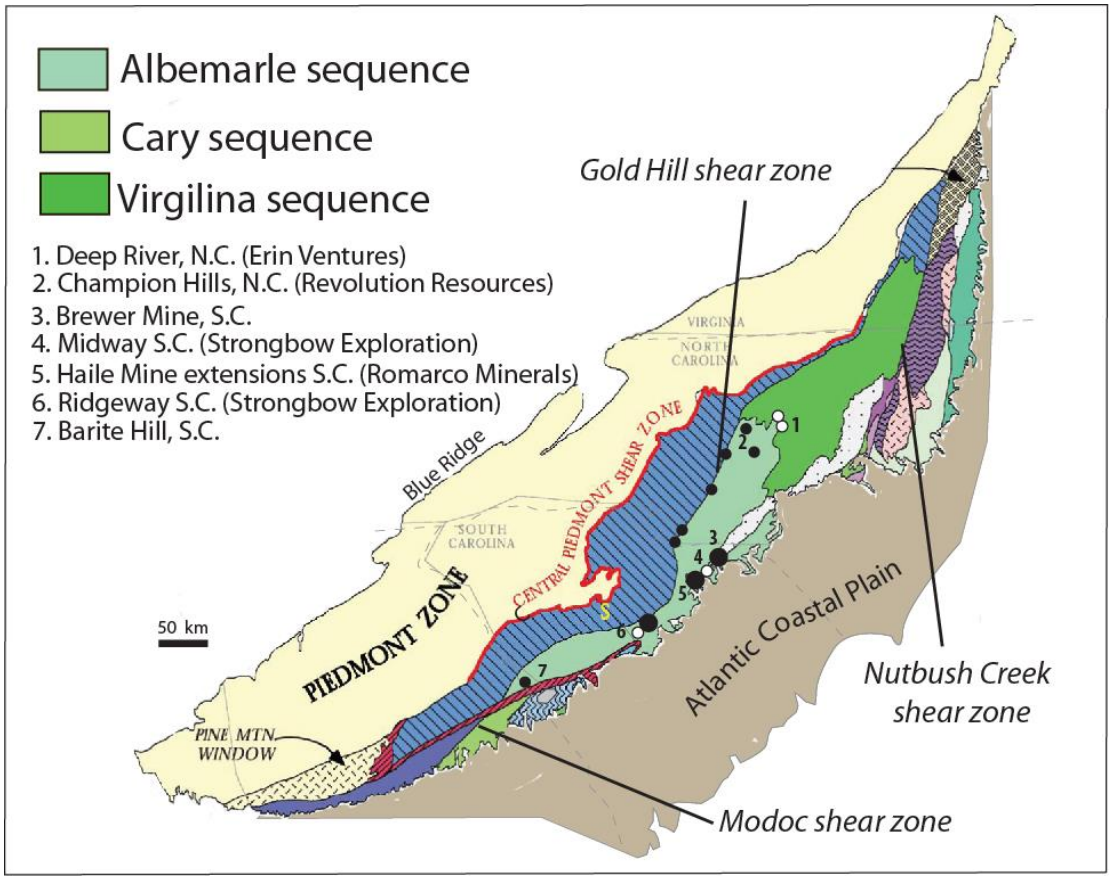

Figure 1.3: Geology of Carolina Terrane with the shear zones (Foley et al. 2012)

www.manaraa.com

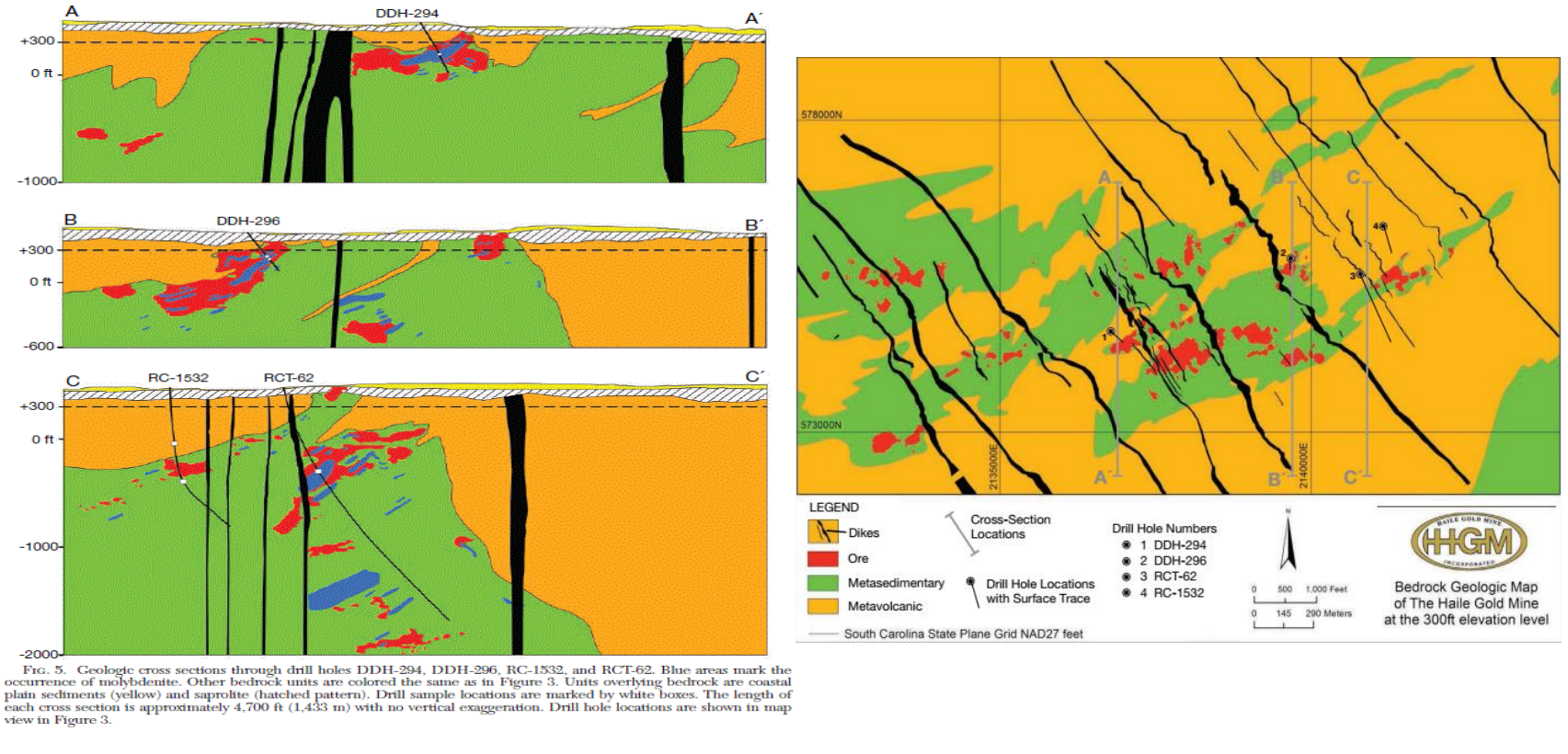

FIG. 5. Geologic cross sections through drill holes DDH-294, DDH-296, RC-1532, and RCT-62. Blue areas mark the occurrence of molybdenite. Other bedrock units are colored the same as in Figure 3. Units overlying bedrock are coastal plain sediments (yellow) and saprolite (hatched pattern). Drill sample locations are marked by white boxes. The length of each cross section is approximately 4,700 ft (1,433 m) with no vertical exaggeration. Drill hole locations are shown in map view in Figure 3.

Figure 1.4: A geologic map of Haile Mine area at 300ft above sea level. On the left side three geological cross sections (Mobley et al., 2014)

www.manaraa.com

CHAPTER 2

DATA ACQUISITION

2.1 Introduction

The study area (Figure 2.1) is located in the northern part of South Carolina between Kershaw to the southwest and Jefferson to the northeast. The survey area consisted of a single block with an area of 131 km² (50.3 sq. miles) over flat low lying terrain in the 150-200m (500-650 ft) region. The survey block boundary co-ordinates are tabulated in table 2.1. The base of survey operations was in Camden, approximately 25 km (15 miles) south of the survey area.

2.2 Data source

The high resolution land gravity data, collected over the study area in 2010, was provided for this study by James Berry, Head Geologist, Haile Gold Mine, OceanaGold Inc. Gravity data has been merged with USGS gravity datasets by Tuten (2013).

The high resolution helicopter EM and Magnetic survey was flown with a line spacing of 328 ft (100 meters) in the eastern section and 164 ft (50m) in the west. The control (tie) lines were flown perpendicular to the survey lines with a spacing of 3280 ft (1000m) and 1640 ft (500 m). The data was acquired by AeroTEM in 2010, figure 2.2.

The nominal EM bird terrain clearance is 98.4 ft (30 meters), but can be higher in more rugged terrain due to safety considerations and the capabilities of the aircraft. A

www.manaraa.com

magnetometer sensor is mounted in a smaller bird connected to the tow rope 70.2 ft (21.4 meters) above the EM bird and 49.9 ft (15.2) meters below the helicopter, Figure 2.3. A second magnetometer is installed on the tail of the EM bird. Nominal survey speed over relatively flat terrain is 46.6 miles/hr (75 km/hr) and is generally lower in rougher terrain.

Scan rates for ancillary data acquisition is 0.1 second for the magnetometer and altimeter, and 0.2 second for the GPS determined position. The EM data is acquired as a data stream at a sampling rate of 36,000 samples per second and is processed to generate final data at 10 samples per second. The 10 samples per second translate to a geophysical reading about every 4.9 to 8.2 ft (1.5 to 2.5 meters) along the flight path.

The geological map produced by OceanaGold (figure 2.4) was used to constrain the geologic interpretation.

Table 2.1: Survey block Boundaries.

X	Y
537098	3827584
539401	3823489
546654	3826603
548147	3824854
553864	3828992
555230	3827584
558387	3829248
553054	3837354

www.manaraa.com

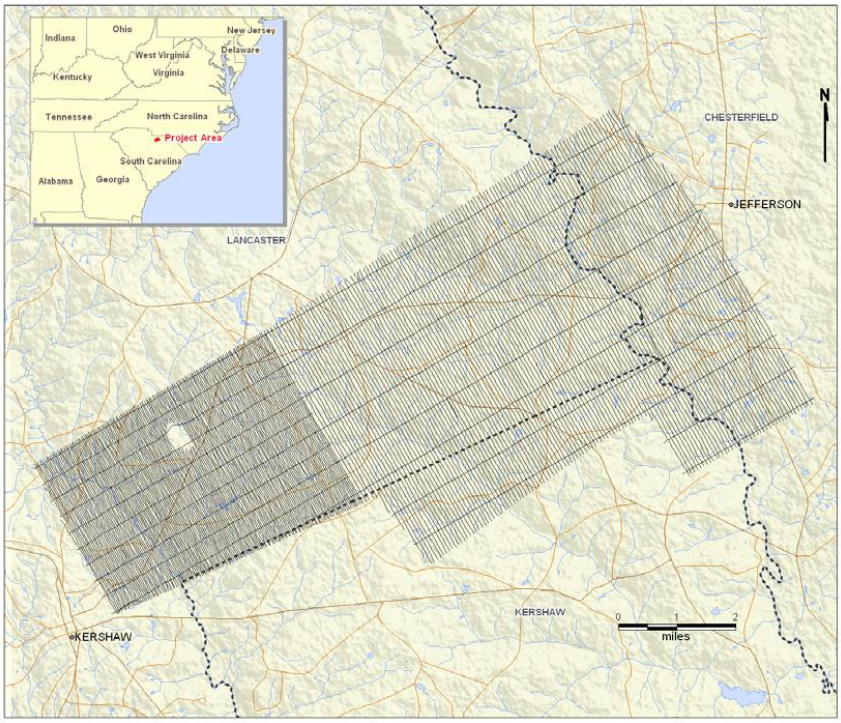

Figure 2.1: The study area location.

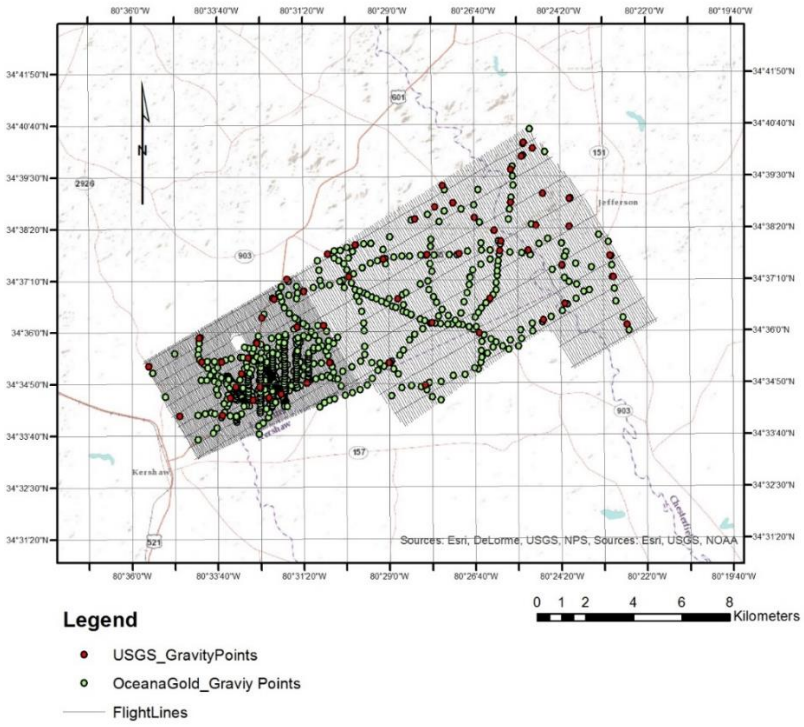

Figure 2.2: The flight lines (EM and Magnetic) and the gravity observation point map. Red color is from the USGC and green color is high resolution gravity from OceanaGold. The coordinates are (34 ˚ 42’0”-34 ˚32’0”’N and 80 ˚ 36’0”-80 ˚ 22’0”W).

www.manaraa.com

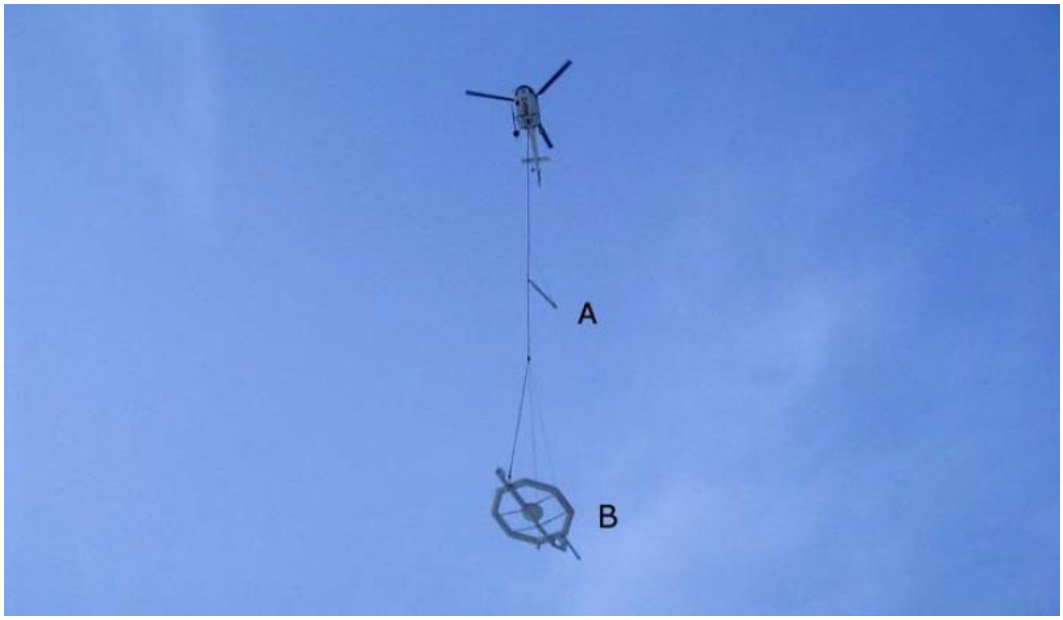

Figure 2.3: A) The magnetometer bird. B) The AeroTEM II EM bird, from the Aeroquest report for Haile Mine June 2010.

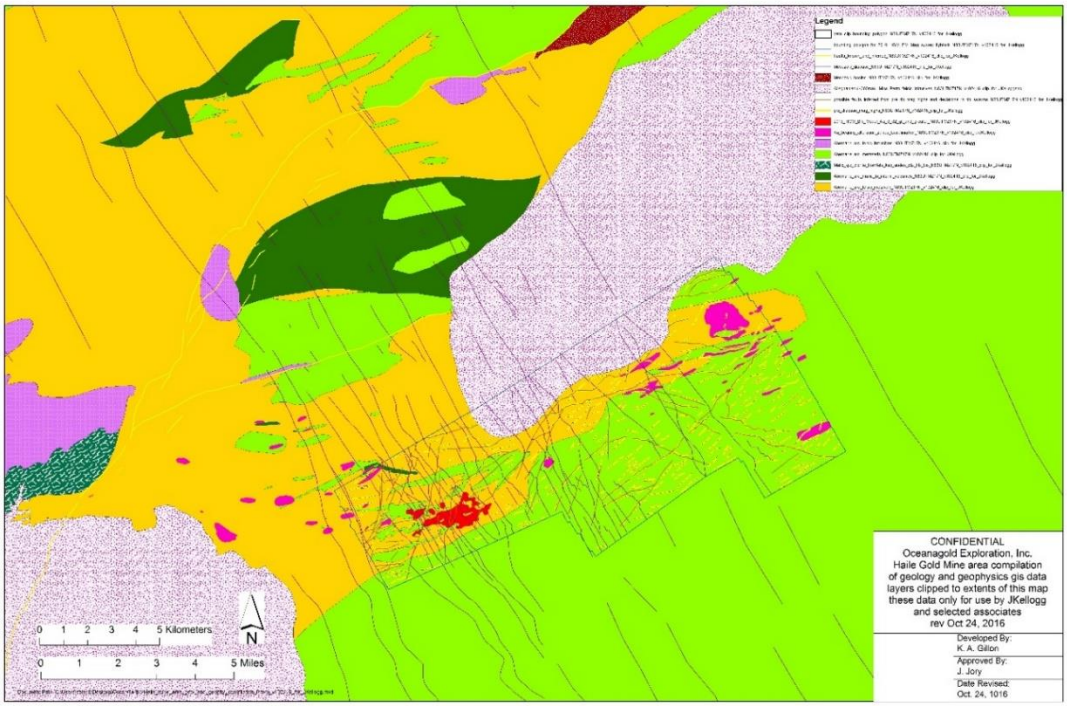

Figure 2.4: Geological map from OceanaGold

www.manaraa.com

CHAPTER 3

METHODOLOGY

3.1 Gravity method:

The gravity method is based on the measurement of variations in the gravitational field of the earth to provide a better understanding of subsurface geology. Gravity anomalies are often caused by deep-seated features, and the changes in the anomalies are related to lateral variations in density (Telford et al 1976). A bar graph (figure 3.1) has been prepared by J. Peters (Dobrin 1960) illustrating the average density of rocks obtained from laboratory measurements on core and surface samples. Generally, basic igneous and metamorphic have higher densities than sedimentary rocks (Dobrin 1960).

Gravity prospecting is usually used as a secondary method in mineral exploration for detailed follow-up of magnetic and electromagnetic anomalies during integrated base-metal surveys. Gravity and magnetic methods cover a large area with low cost compared to other methods, such as seismic surveys. The gravity density variations are small and uniform compared to changes in magnetic susceptibility, and the gravity anomalies are much smaller and smoother than magnetic anomalies (Telford et al 1976).

The applications of gravity surveys to mineral deposit exploration includes rock types, structures, and occasionally, ore bodies themselves (Wright, 1981; Hoover et al. 1995). Gravity data have proven a useful technique in the study of mineralized epithermal

www.manaraa.com

systems (Irvine and Smith 1990; Feebrey et al 1998; Morrel et al 2011). Morrel et al. (2011) observed a positive gravity anomaly over an epithermal mine in New Zealand.

Also, in Iceland, Idaho and Japan, positive gravity anomalies were observed over mines by Hochstein and Hunt, 1970, Criss et al. 1985, and Izawa et al. 1990 (Morrel et al., 2011). Hinze (1960) showed that a positive gravity anomaly differential reflects the greater density of the iron ore minerals as compared to the minerals of country rocks, where the iron ore minerals have densities of 5.1 g/cc, while the country rock mostly range between 2.6 to 3.0 g/cc.

Gravity applications are still widely used in the mining industry as an exploration tool to map subsurface geology and to estimate ore reserves for some massive sulfide ore deposits. Additionally, the gravity technique is sometimes applied to detect shallow faults and paleochannels in hydrologic investigation (Nabighian et al. 2005, 65ND).

3.1.1 Basic theory:

3.1.1.1 Newton's law

The theory behind gravitational is expressed by Newton's law, which is based on the force of mutual attraction between two particles of masses m1 and m2 which is directly proportional to the product of the masses and inversely proportional to the square of the separation r between the centers of mass:

$$F= \gamma \frac{m_1 m_2}{r^2} r_1$$

www.manaraa.com

Where F is the force on $m_{2,}$ r_1 is a unit vector directed from m^2 toward m_1, r is the separation between $m^1$and m_2 , and γ is the universal gravitational constant. (Telford et al 1990).

3.1.1.2 Acceleration of gravity

The acceleration g of a mass m_2 due to the presence of a mass m_1 can be found simply by dividing the force attraction F by the mass m_2:

$$g= \frac{\gamma m_1}{r^2} r_1$$

The acceleration of g belongs to the gravitational force per unit mass due to m_1. If m_1 is the mass of the Earth, M_c, g becomes the acceleration of gravity and is given by

$$g= \left(\gamma M_c / R^2_c\right) r_1$$

R_c is the radius of the Earth and r_1 extending downward the center of the Earth.

The acceleration value of gravity at the earth's surface is about 980 cm/s^2 (980gals). The g unit is milligal (mGal), where 1Gal = 1cm/s^2= 0.01 mGal. (Telford et al 1990)

3.1.2 Theoretical gravity:

The surface of the earth is defined as an oblate ellipsoid. The average gravity value varies from 978031.85 mGal to 983217.72 mGal between the equator and the pole at sea level with the land above it removed. The formula can be written to describe the theoretical value of gravity, given by the International Association of Geodesy 1967

www.manaraa.com

g_t= 978031.85 (1+ 0.005278895 $\sin^2 \emptyset$ + 0.000023462 $\sin^4 \emptyset$) mGal; where $\emptyset$ is latitude of observe point (degree) (Telford et al 1990).

3.2 Magnetic method:

Magnetic prospecting is the oldest method of geophysical exploration, and it is used in searching for oil and minerals. In oil prospecting it is used to define the thickness of the sedimentary sequence, as it is less magnetic than metamorphic basement rocks, and it can be used to estimate the depth to basement. Now, virtually all magnetic prospecting for oil and minerals is carried out with aero-magnetic instruments (Dobrin 1960).

The magnetic method has much in common with the gravitational method, but the magnetic field is much more complicated and variable. The magnetic field is bipolar, non-vertical in direction, with sharp local anomaly variations, while the gravity field is unipolar, vertical in direction, with smoother and regional anomalies (Telford et al 1976).

The sources of local magnetic anomalies cannot be very deep, the magnetic depth is limited by the Curie isotherm of crustal rocks ≈ 550 C^0, where rocks lose their magnetic properties. Therefore, the sources of local magnetic anomalies must be associated with features of the upper crust (Telford et al 1990).

In sedimentary regions, especially where the basement depth exceeds 1.5 km, the magnetic contours are normally smooth and variations are small, reflecting the basement sources rather than near-surface features. Larger magnetic anomalies commonly reflect the susceptibility variations of basement rather than the basement relief (Telford et al 1990). The regions where igneous and metamorphic rocks predominate usually show

www.manaraa.com

complex magnetic variations. Deep features are frequently camouflaged by higher frequency magnetic effects originating nearer the surface (Telford et al 1990).

The separation of contour lines often provide a useful criterion for structure, the closer the contours, the shallower the source. Any abrupt change in the contour spacing suggests a discontinuity at depth, possibly a fault. In mineral prospecting where ore zones are smaller and shallower, a flight-line spacing of 1.6 km or less is necessary to make sure that an anomaly between the flight-lines will not be lost (Dobrin 1960).

The angle between the total field (F) and its horizontal component (H) is called inclination (I). The total magnetic field pointed vertically downward at the north magnetic pole is $+90^0$ inclination, and pointed vertically upward at the south magnetic pole is -90^0 inclination. The field pointed horizontally at the magnetic equator is 0^0 inclination. The magnetic declination (D) of the total field is the angle between its horizontal component (H) and the geographic north (X) (Dobrin 1960; Lillie 1999).

Magnetic susceptibility is the most significant property of rocks. A bar graph (figure 3.2) has been prepared by J. Peters (Dobrin 1960) illustrating the average magnetic susceptibilies of rocks from laboratory measurements on a large number of rock samples, igneous, metamorphic, and sedimentary. Generally, igneous and metamorphic rocks have higher susceptibilities than sedimentary rocks.

In mineral prospecting it is not usually possible to detect minerals other than pyrrhotite, ilmenite, or magnetite (Dobrin 1960). Alteration zones are commonly evident as ovoid or circular magnetic low. Usually, epithermal mineralization deposit are in weakly magnetic sedimentary units. In this case, magnetic survey may not be effective

www.manaraa.com

due to the lack of magnetic contrast (Irvine and Smith 1990). Hydrothermal alteration can destroy magnetite, creating a broad, smooth magnetic low (Ford et al 2007). For example, alteration in the Waihi-Waitekauri region caused a destruction of magnetism (Morrell et al. 2011).

3.3 The helicopter time domain electromagnetic method (HTEM):

The electromagnetic survey is a very useful tool in mineral, groundwater and hydrocarbon exploration (Smith 2010). All electromagnetic methods are based upon the fact that the magnetic field varies in time - the primary field - and so, according to the Maxwell equations, induces an electrical current in the conducting surroundings. The associated magnetic and electrical fields are called the secondary fields. After the transmitter is turned off, the secondary field from the current in the ground is equivalent to the primary field (Sørensen et al. n.d). In other words, the transmitter loop generates the primary EM field, while the receiver coil receives the secondary field (rock body), (figure 3.3). The EM main method is inductive electrical conductivity, which is a measure of how easily electrical current can pass through a material (Lane 2002).

In mineral prospecting, electromagnetic methods have been used quite successfully in the mining industry. Helicopter systems have been effective in near-surface mapping, but depth penetration is limited in areas with conductive overburden. The HTEM systems are similar to ground electromagnetic systems (Allard 2007).

Fixed-wing time domain systems use high moment transmitters and have no rigid geometry. These systems have much greater depth and less spatial resolution than a helicopter born frequency domain system. Since 1995, a number of attempts have been

www.manaraa.com

made to adopt the advantage of the fixed-wing time domain to the helicopter. The AeroTEM system is based on a rigid geometry, where the receiver coil is placed in the middle of the transmitter loop. The transmitter is 40 m below the helicopter and 30 m above the terrain. The magnetometer is separately towed at 10 m above the EM system. The system also contains bucking coil, laser altimeters, and a global positioning system (GPS) (figure 3.4) (Balch et al. 2003). The bucking coil is used to reduce the primary field at the receiver (Allard 2007). Finally, the AeroTEM has the same advantages as airborne and helicopter EM systems of achieving much greater depth penetration and having excellent spatial penetration (Balch et al. 2003). The conductivity measurement shows that the igneous and metamorphic rocks have a low conductivity compared to the sulfides ($> 10^5$ - conductor; $< 10^{-8}$ - insulator; $>10^{-8} < 10^5$ - semiconductor) (figure 3.5).

The electromagnetic system used in the study area is an Aeroquest AeroTEM II time domain towed-bird system. The current AeroTEM II transmitter dipole moment is 50 kNIA. The AeroTEM bird is towed 36.6 meters (120 ft.) below the helicopter. The wave-form is triangular with a symmetric transmitter on-time pulse of 1.10 ms and a base frequency of 150 Hz. The current alternates polarity every on-time pulse. During every Tx on-off cycle (300 per second), 120 contiguous channels of raw X and Z component of the received waveform are measured. Each channel width is 27.78 microseconds starting at the beginning of the transmitter pulse. This 120 channel data is referred to as the raw streaming data. The AeroTEM system has one EM data recording streams, the newly designed AeroDAS system which records the full waveform, (figure 3.6) (Aeroquest, 2010).

www.manaraa.com

Overall, the electrical current flow is through moist or saturated pore space in soil or rock. So, the bulk conductivity of geologic units is much greater than the minerals they are composed of (Stewart 1981). Ore bodies are not the only cause for a high conductivity signal, graphite, faults, shears, bodies of water, and man-made features can also result in a high conductivity signal (Keary et al. 2002). Cultural noise "man-made features" such as power lines, pipelines, buried pipes etc. generate an electromagnetic field (Qian and Boerner, 1995). This cultural noise can be reduced by applying high spatial frequency or Butterworth filters (Al-Fouzan et al. 2004). In general, resistivity is low with hydrothermal alteration, when sulfides are concentrated and connected at about 5-percent volume or more, and with faulting. A high resistivity is associated with silicification or intrusive zones (Hoover et al 1992).

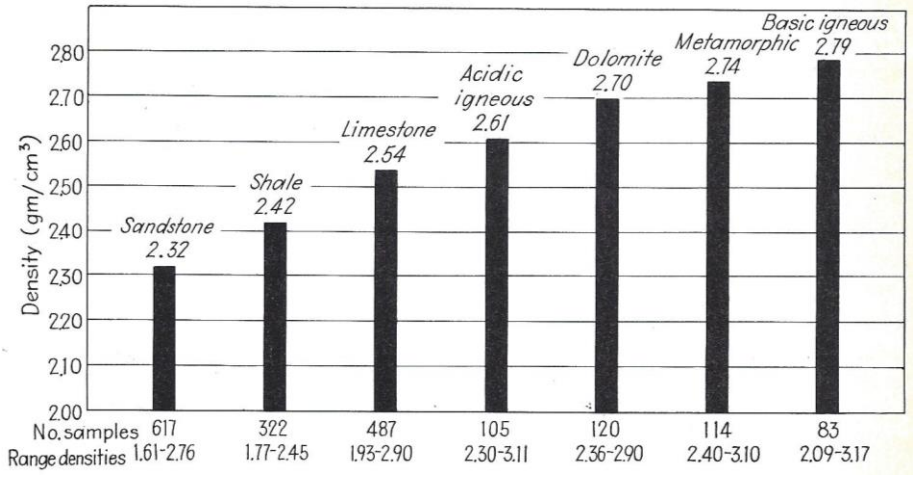

Figure 3.1: Average densities of surface samples and cores based on laboratory measurements, prepared by J. Peters from Dobrin (1960).

www.manaraa.com

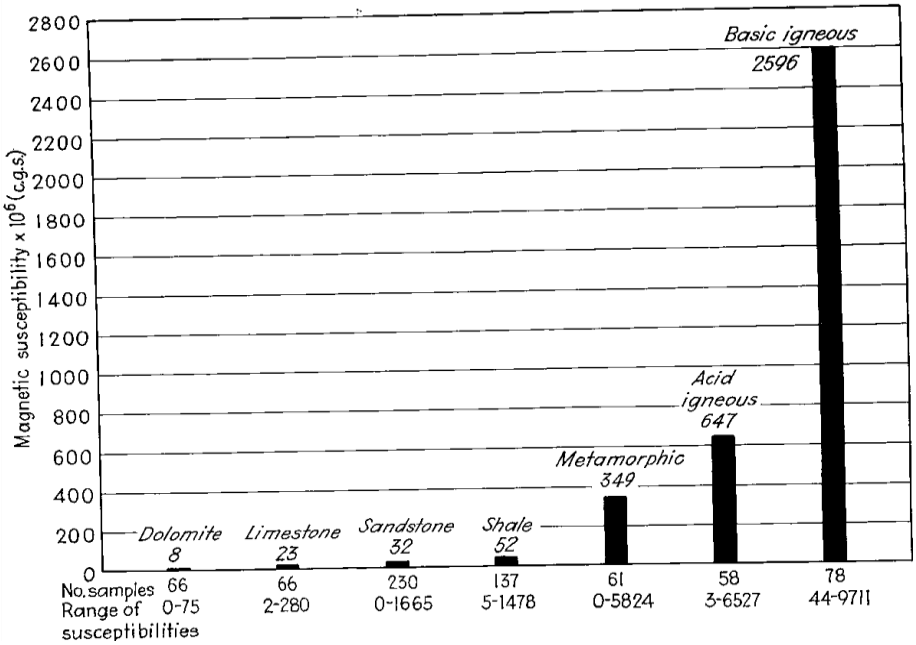

Figure 3.2: Magnetic susceptibility of source samples and cores from laboratory measurements, prepared by J. Peters from Dobrin (1960).

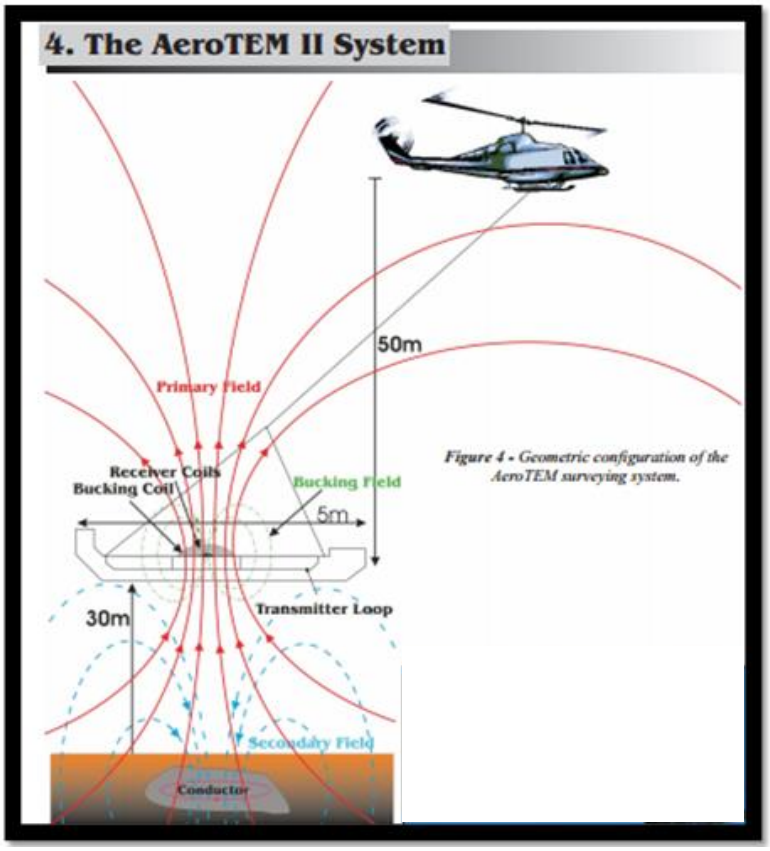

Figure 3.3: The principle of helicopter method, shows the primary (induced) field related to the transmitter and the secondary (measured) field related to geology, Anshütz (2014).

www.manaraa.com

Figure 3.4: AeroTEM system (Balch et al. 2003).

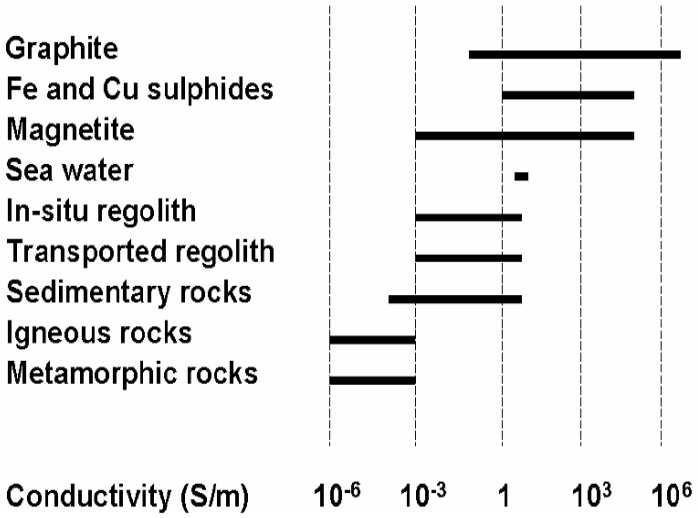

Figure 3.5: Rock conductivity parameters (Lane 2002).

www.manaraa.com

Figure 3.6: AeroTEM II instrument rack.

www.manaraa.com

CHAPTER 4

INTERPRETATION METHODS

The main goal of interpretation of potential field data is to map subsurface structures, e.g., faults and contacts. The interpretation in this study is constrained by geological mapping by OceanaGold.

Much can be learned from potential field data through enhancement techniques filters. These filters can be applied in either space or Fourier domain. The data is converted from spatial-domain to wave-number domain by using fast Fourier transform technique, then filters are applied. Next, the data is transformed back to space domain (Whitehead and Musselman 2011; Reeves 2005).

The interpretation and analysis of potential field data was accomplished by applying the following techniques: Tilt derivative, Reduced to the pole, shaded relief, Power spectrum, Analytical signal, Source parameter image, Euler deconvolution, Upward continuation, and 2D modeling.

Power Spectrum technique:

Several authors, such as Spector and Grant (1970) and Bhattacharya (1965), explain the power spectrum method, based on using fast Fourier transform (FFT) to analyze the potential field data. The FFT transformed the grid from space domain into wavenumber domain. Then, it is multiplied by the wavenumber response of the

www.manaraa.com

appropriate digital filter. Finally, the transform result of the Fourier coefficients is inverted back into space domain, (figure 4.1) (Hildenbrand 1983; Reeves 2005).

Spectral analysis of the potential anomaly field indicates an ensemble average depth to the different sources of anomalies (Rama Rao et al. 2011; Whitenhead and Musselman 2011; Reeves 2005). Two dimension analysis of the power spectrum of field data is a helpful tool to estimate the average depths of different magnetic horizons with distinct changes in magnetic properties (Spector and Grant, 1970; Reddi et al., 1988).

In general, the curves of the power spectrum consist of two parts of linear segments. The first part, which relates to deeper sources, is in the low frequency end where the rate of power decay is linear and can be approximated by straight line. The second part is in the high frequency end and relates to shallower sources (Spector and Grant 1970; Reeves 2005).

This methodology is advantageous because it is statistically oriented, averaging source depths over a region containing complex anomalies. Also, as it is based entirely on the analysis of the wavelengths of anomalies, it is less affected by interference due to overlapping anomalies and high-frequency noise than other methods (Hinze et al. 2013/p-368). This method has been used to map the depth of the Curie point isotherm (about 580 ^{0}C) where the rocks lose their ferromagnetic properties (Hinze et al. 2013/p-371).

Spector and Grant (1970) indicate that the relationship between the power logarithm and wavenumbers is used to estimate the depth of the source body. The logarithm of this factor is a linear slope approximately twice the depth of the linear segment.

www.manaraa.com

Low-pass filters, the deep-crustal or sub crustal sources in the regional field, pass the long-wavelength anomalies (broad slow changes in the potential-field data), where the high-pass filters pass the short-wavelength anomalies (residual) that usually belong to shallow features. Thus, wavelength filters are used to isolate the deep seated anomalies from the shallower anomalies. This isolation is based on the assumption that the cutoff wavelength of this filter is related to the maximum depth of the source (Dobrin and Savit, 1988; Whitenhead and Musselman 2011**;** [2]Geosoft).

To separate the regional and residual components of the potential fields, the Butterworth filter tool was used. The Butterworth filter is excellent for applying straightforward high-pass and low-pass filters to potential data as it can easily controls the degree of filter roll-off (degree of the sharpness of the cutoff wavenumbers) while leaving the central wavenumber fixed (Whitenhead and Musselman 2011). The Butterworth enable rejection of the desired central range while keeping the low and high "extremes" of frequency continuum **(**Whitenhead and Musselman 2011; [2]Geosoft).

Tilt Derivative (TDR):

Tilt derivative is another method used to enhance the shallow geological sources and to estimate the depth. Tilt derivative or tilt angle, or local phase, was first described by Miller and Singh (1994) and refined by Verduzco et al. (2004) and has been developed by Salem et al (2007; 2008). TDR is a normalized derivative based on the ration of the vertical and horizontal derivatives of the field (Salem et al 2007). The method is not based on the moving window study approach as in the Euler deconvolution method (Hinz et al. 2013-p385). The TDR method assumes the source structures have buried 2D vertical contacts (Salem et al 2007; 2008).

www.manaraa.com

The tilt derivative (Miller and Singh 1994; Verduzco et al. 2004) is defined as:

$$TDR = \tan^{-1}\left(\frac{VDR}{THDR}\right)$$

Where VDR and THDR are first vertical and total horizontal derivatives, respectively, of the total magnetic intensity T.

$$TDR = \tan^{-1}\left(\frac{dT/dz}{\sqrt{\left(\frac{dT}{dx}\right)^2+\left(\frac{dT}{dy}\right)^2}}\right)$$

Where T is the 1st derivative of the field, while dT/dz, dT/dx, and dT/dy are 1st derivative of the field in directions of x, y and z, respectively (Salem et al 2007, 2008).

The tilt depth technique (Salem et al. 2007) uses the reduced magnetic field and supposes buried 2D vertical contacts, defined as

$$Tilt = \tan^{-1}\left(\frac{h}{z}\right)$$

Where h is horizontal distance (over contact) and z is the depth to the top of the contact. This equation indicates that when the value of the tile angle is 0^0 (h=0) this is the location of contact and equal to 45^0 when h=z and -45^0 when h=-z.

The tilt derivative range is between $\pm 90^o$ regardless or $-\pi/2$ and $\pi/2$ (radian) of the amplitude of the vertical derivative or the absolute value of the total horizontal gradient (Salem et al. 2007; 2008).

The zero contour of the tilt derivative map can be used to delineate the edges of source bodies, and its negative values are outside the source (Miller and Singh 1994). Furthermore, the horizontal distance from 45^o to 0^o position of tilt derivative is equal to

www.manaraa.com

the depth to the top of the contact, half the physical distance between $\pm 45^{o}$ contours (Salem et al. 2007; 2008).

Salem et al. (2008) indicated that tilt derivative can be used on a magnetic grid to estimate the depth and location of anomaly sources without prior knowledge of the geometry of the sources. The result contains no information on either the geomagnetic field strength or the susceptibility of source bodies, so by implication contains no information on the subsurface magnetization. Nevertheless, the method contains information on the depth of the source of the anomaly (Salem et al. 2010).

Salem et al. (2007) presented magnetic modeling that relates to a simple magnetic body with vertical contact and magnetization (magnetic inclination of 90). The TDR response is +90 above the source body and -90 away from these source body. To remove the inclination dependency, the tilt derivative is applied to the reduction of the total magnetic intensity map.

This method has some advantages: 1) it is dependent on the first order derivatives, and thus is less subject to noise than other methods requiring higher-order derivatives; 2) it can be used on a magnetic grid to estimate the depth and location of anomaly sources without prior knowledge of the geometry of the sources; and 3) unlike the Euler method, there is no need to choose and move window size, nor is there a problem of solution clusters to contend with (Salem et al. 2007).

3-D Analytical signal method:

Analytic signal is a linear equation derived to provide the source location parameters of a 2D magnetic body without a priori information about the nature of the

www.manaraa.com

source, Salem (2005). This technique is used to estimate the depth and locate the edges of an anomaly's source and approximate its geometry (Salem and Ravat, 2003). Analytic-signal was first used by Nabighian (1972) and Blakely (1995).

This method assumes that causative sources are 2D geological structures, such as contacts, dikes and horizontal cylinders (MacLeod et al. 1993; Salem 2003). It depends on the 1st order derivatives of the horizontal and vertical of magnetic field, and the source direction causing the anomalies. It shows maxima over magnetization contacts (Roset et al. 1992) and a maximum value over the edge of the fault/contact.

Roset et al. (1992) indicated that the absolute amplitude value of the 3-D analytic signal is easily derived by calculating the three derivatives of magnetic anomalies at locations (x,y) using the expression

$$AS = \sqrt{\left(\frac{\partial f}{\partial X}\right)^2 + \left(\frac{\partial f}{\partial Y}\right)^2 + \left(\frac{\partial f}{\partial z}\right)^2}$$

The analytic signal (AS) is the square root of the sum of the squares of the derivatives in the x, y and z directions. Where əf/əx, əf/əy and əf/əz are the first vertical and horizontal derivatives of the observed magnetic field. MacLeod et al. (1993) mentioned that the use of a 3-D perspective presentation is to exhibit how the anomaly of the AS peaks over the edges of the source.

The analytic signal can be used for delineating geological boundaries, as analytic signal relies upon the strength and not the direction of the source's magnetism (Dentith and Mudge 2014). The amplitude of the analytical signal and its derivatives are

www.manaraa.com

calculated in the frequency domain using the fast Fourier transform technique (Blakely 1995; Salem 2004). An advantage of this method is that the magnetization direction does not need to be known, because anomalies will be shifted properly over the top of the source bodies (Hsu et al. 1998). Finally, the application of analytic signal does not have to be limited to magnetic anomalies; it can also be applied to gravity, Roest et al. (1992).

3-D Euler deconvolution (ED) technique:

The Euler deconvolution is a common technique used in the interpretation of magnetic and gravity data and to produce a map shows the depths and locations of the geologic sources of the magnetic or gravity anomalies observed in a 2D grid. It's an inversion method used to estimate the depth and outline the boundaries of the source bodies. For mineral exploration, the depth estimates are used to define the location and depth of source that cause a magnetic or gravity anomaly (Whitehead 2010).

The method was developed by Thomson (1982) to interpret 2D pole reduced magnetic profile and extended by Reid et al. (1990) to be applied to gridded data. An advantage of the Euler deconvolution method is that it is independent of field direction, dip, or strike of the anomaly feature, so the reduction to pole is unnecessary, as the source positions can be accurately reproduced. Also, this technique assumes no particular geological model.

The 3D Euler deconvolution is based on the Euler's homogeneity equation, an equation that relates the potential field (magnetic or gravity) and its gradient components to the location of the source, with the degree of homogeneity N, which may be interpreted as a structural index. The structural index (SI) is a measure of the rate of

www.manaraa.com

change with distance of a field. For example, the magnetic field of a narrow 2-D dyke has a structural index of N=1, while a cylinder or vertical pipe gives N=2. The step and contact have a structural index of N=0 in magnetic. In a gravity field, a pipe has a structural index of 1, while a sphere has a structural index of 2. The three gradients (vertical and two horizontal gradients) of the potential field are normally calculated using the Fast Fourier transform (FFT) (Thompson, 1982; Whitehead 2010).

The depth estimation resulting in Euler deconvolution relies mainly on structure index (SI) choice. The SI parameter value relies on the source body type and the potential field, table 4.1 summarizes the structural indices for simple models for magnetic and gravity field (Whitehead 2010). Reid et al. (1990) indicated a structural index value of 0 for gravity data to detect faults, table 4.2 summarize the structural index for gravity of simple mass model. The Euler solutions are located outside of the study area, due to instability of the moving window of Euler solution. Can be taken into account in the interpretation as fare as these solutions show good clustering (Saibi et al. 2006).

The depth tolerance determines which solutions are accepted (i.e. accepts solutions with error estimate smaller than the specified tolerance). The default is 15 percent — typically a good starting value for a first pass at analyzing the data. A smaller tolerance will result in fewer but more reliable solutions. The Window size determines the area (in grid cells) used to calculate the Euler solutions. All points in the window are used to solve Euler's equation for a source position (Whitehead 2010).

The Euler deconvolution in 3D is given by Reid et al. (1990)

$$(x-x_0)\,\partial T/\partial x + (y-y_0)\,\partial T/\partial y + (z-z_0)\,\partial T/\partial z = N\,(B-T)$$

www.manaraa.com

Where (x_0, y_0, z_0) is the position of a magnetic source whose total field T observed at (x, y, z). The total field has a regional value of B (background value). N is the structural index (SI). The gradients ∂T/∂x, ∂T/∂y and ∂T/∂z are the first derivatives in the direction of x, y and z.

The ED's system uses a least squares method to solve Euler's equation simultaneously for each grid position within a sub-grid (window). It is inverted the Euler's homogeneity equation over a window at every grid data, (Whitehead 2010).

Table 4.1: Structural indices parameter values after Whitehead (2010).

SI	Magnetic field	Gravity field
0.0	contact	sill/dyke/step
0.5	thick step	ribbon
1.0	sill/dyke	pipe
2.0	pipe	sphere
3.0	sphere	

Table 4.2: Structural indices N for the gravity anomaly (GA), first derivative (FD), and second derivative (SD) gravity anomalies of some mass models, after Hinze et al (2013)

Model	GA	FD	SD
Sphere (point mass)	2	3	4
Horizontal cylinder (horizontal line mass)	1	2	3
Vertical pipe (vertical line mass)	1	2	3
Faulted thin-bed (small-throw double-sided fault)	1	2	3
One-sided fault (small-throw semi-infinite horizontal sheet)	0	1	2
Contact/edge	−1?	0	1

www.manaraa.com

Two-dimensional gravity modeling:

Two-dimensional (2D) models consider the earth in two dimensions, i.e. it changes with depth (the Z direction) and in the direction of the profile (X direction; perpendicular to strike). 2D models do not change in the strike direction (Y direction). 2D blocks and surfaces are presumed to extend to infinity in the strike direction. GM-SYS allows profiles that dip to the strike of the model. The profile angle calculated from the strike direction is entered as relative strike. For profiles perpendicular to the strike, the relative strike is 90^0 (Geosoft GM-SYS, nd).

The 2-D modeling program provides a geological evaluation reasonableness model based on any geological and geophysical previous data on the study area. The two dimensional gravity modeling program is a technique that is based on fitting the gravity parameters with the observed data from potential field.

Reduced to pole (RTP):

The Reduction of total magnetic field intensity to the pole process was illustrated by Baranov (1957). The total magnetic intensity field was reduced to pole by using the Gx's technique (Phillips, J.D., 2007). The RTP was calculated using the inclination and declination values of 63^o and -7.20^o, respectively. This filter is applied in the Fourier domain and it migrates the observed field from observation inclination and declination, to what the field would look like at the magnetic pole. This aids in the interpretation since any asymmetry in the reduced to pole field can then be attributed to source geometry and/or magnetic properties ([3]Geosoft technical notes). The anomalies result in the RTP magnetic map result will be directly located above the source, figure 4.2.

www.manaraa.com

The magnetic anomaly shape relies not only on the susceptibility and shape of the perturbing body, but also on the direction of its magnetization and direction of the regional field. The RTP (Reduction of total magnetic field intensity to the pole) technique transforms an anomaly into the anomaly that would be detected if the magnetization and regional field were vertical. Thus, RTP removes the asymmetries caused by a nonvertical magnetization or regional field and produces a simple set of anomalies to interpret (Dobrin and Savit 1988). However, for an accurate interpretation of the magnetic data, it has been suggested to reduce the total field to magnetic pole in order to remove the effect of magnetic latitude on the anomalies (Bhattacharyya 1965).

Grant and Doddo (1972) stated that the reduction to magnetic pole filter requires the azimuthal orientation of the sensor θ in order to perform the reduction to the pole. This tool assumes that lines are relatively rectilinear, and calculates the orientation of each line using the first and last point of the line. RTP can be calculated in the wavenumber domain using the following equation,

$$L(\theta) = \frac{I}{(\sin Ia + i\cos.\cos(D - \theta))^2}$$

Where θ is the wavenumber direction, I is the magnetic inclination, D is the magnetic declination and *Ia* is the inclination for amplitude correction. *Ia* is set to an inclination greater than the true inclination of the magnetic field or less than the true inclination in the Southern hemisphere (Macleod et al 1993).

Shaded-relief:

Shaded relief is "calculating the first horizontal derivative in the direction of a supposed illumination" Reeves (2005).The shaded relief technique is commonly used to

www.manaraa.com

enhance the image. This image is useful in the analysis of magnetic anomaly maps, since the large gradients typical of magnetic anomalies are hard to interpret in contour maps. Also, this method is useful in identifying lithologic-geology (Hinz et al. 2013; p 317-318). Short-wavelength anomalies associated with local sources are enhanced, similar to the vertical derivative method (Hildenbrand and Kuchs 1988).

The shaded relief map presents magnetic anomalies as topography. It is used to enhance and highlight most linear trends perpendicular to the illumination direction. The surface reflection in shaded relief depends in the orientations of the topography related to the position of the sun. (Dentith and Mudge 2014)

Source Parameter Imaging (SPI):

The source parameter imaging technique is a fast and easy method for calculating the depth of source bodies. Its accuracy has been shown to be +/- 20% in tests on real data sets with drillhole control. Its accuracy is similar to the Euler deconvolution method; however, source parameter image produces a complete set of clear solution points and is easier to use. Thurston and Smith (1997) indicated that the goal of the source parameter image method is that the image result can be interpreted easily by someone who is not familiar with magnetic interpretation, but is an expert in the local geology. Source parameter image called "local wavelength" is a method based on the extension of the complex analytical signal. The local wavenumber for the magnetic field given by Nabighian (1972) as

$$K=\frac{1}{|A|^2}\left(\frac{\partial^2 T}{\partial x \partial z}\frac{\partial T}{\partial x}-\frac{\partial^2 T}{\partial x^2}\frac{\partial T}{\partial z}\right)$$

Where T is the total magnetic field, x and z are the horizontal and vertical

www.manaraa.com

direction, and $|A|$ is the analytic signal amplitude.

Where

$$|A| = \sqrt{\left(\frac{\partial T}{\partial x}\right)^2 + \left(\frac{\partial T}{\partial z}\right)^2}$$

The SPI techniques assumes either a 2-D sloping contact or a 2-D dipping thin-sheet model. The grid solutions show the source depths and edge location. The depth estimate results are independent of the magnetic inclination, declination, dip, strike and any remanent magnetization (Thurston and Smith 1997).

The depth estimated directly over the source edge at location x=0

Depth = $1/K_{max}$

where K_{max} is the maximum value of the local wavenumber K over the step source (SPI.GX geosoft).

So, the SPI first calculates analytic signal and local phase and then finds the peak values by using the Blakely and Simpson (1986) method. The Blakely method is calculated each grid intersections and compared with its eight surrounding grid cells in four directions (x-direction, y-direction, and both diagonals) to see if a peak is present. These peak values are used to calculate depth solution that saved to a database (SPI.GX geosoft; Blakely and Simpson 1986).

An advantage of this method is that the interference of anomalies is low, since the second-order derivatives are generated by this method to create the image. The SPI estimate source parameters from gridded data and this has two advantages. First, it eliminates errors caused by survey lines that are not oriented perpendicular to strike.

www.manaraa.com

Second, there is no dependence on window selection or size operation, as other methods require. In practice, the technique is used on gridded data by estimating the strike direction at each grid point (Thurston and Smith 1997). The vertical derivative grid is calculated in the frequency domain, and the horizontal derivatives are calculated in the space-domain, using Geosoft (version 8).

Compared to the analytical signal, the local wavelength gives a better resolution and has maximums that are inversely proportional to depth. The peaks of the local wavelength and analytic-signal can be used either to map the edge or contact of the source body. Nevertheless, the local wavelength presents more features and better resolution (Thurston and Smith 1997).

The local wavenumber, like the analytic signal, is independent of source magnetization and dip effects; however, parameter positions such as depth and horizontal location can be determined directly from the magnetic field (Pilkington and Keating 2006).

The inversion of the local wavelength corresponds to the contact depth, where the warm color indicates a high wavelength and cold color indicates the low wavelength. The color bar shows the inverse of the local wavelength, it has units of meter.

Upward continuation filter:

The observation of an airplane can be "recalculated" on a different plane view. Upward continuation is a "clean" filter as it has no side effects. It is changed the measurement surface of potential field to another surface. Used to reduce the effects of shallow features and noise in grids (Whitenhead and Musselman 2011).

www.manaraa.com

The wavenumber filter that creates upward continuation is defined as

$F(w)= e^{-hw}$

Where h is distance in ground units, relative to the observation of the plane

w is wavenumber (radians/ground_unite)

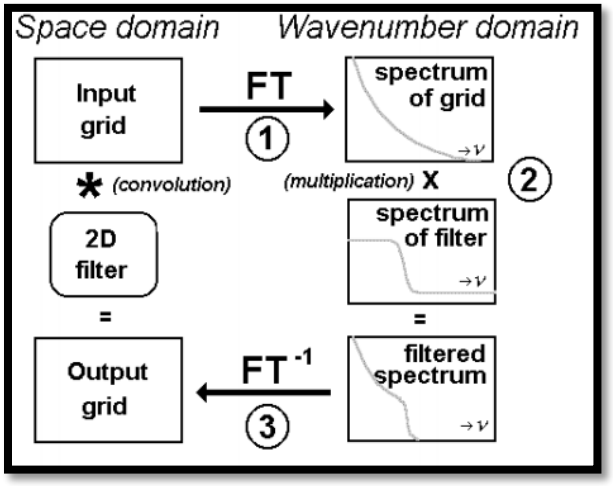

Figure 4.1: A three stage process using multiplication in the wavenumber domain can be more efficient than convolution in the space domain, (Reeves 2005).

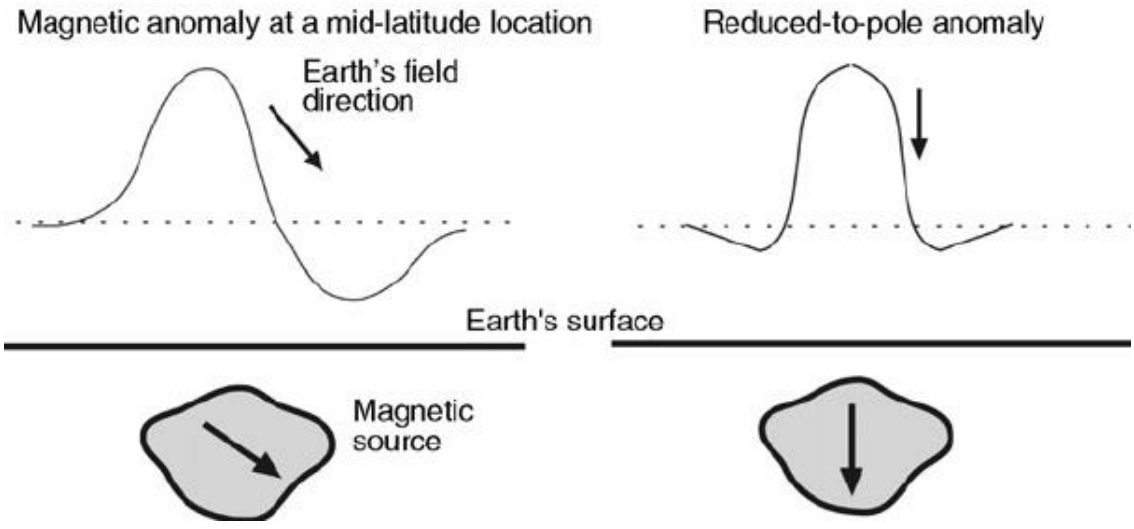

Figure 4.2: Magnetic anomaly of total field before and after the reduction to pole transformation that makes anomaly directly located above the source, after (Ravat 2007).

www.manaraa.com

CHAPTER 5

RESULTS

5.1 Gravity Data Results

The Bouguer gravity values (figure 5.1) increase gradually from 2.1 mGal in the north to over 16 mGal in the western part of the study area. The changes in gravity anomalies are related to density differences of the rocks. The Bouguer map shows low gravity anomalies (blue color) to the north over the Pageland granite. High gravity anomalies (pink color) to the west may be related metavolcanics and/or dikes. The low gravity anomalies over the Haile Mine area are related to the increase in the thickness of the metasedimentary section. The medium gravity values (green and yellow color) in the central part of the study area are possibly related to the coastal plain sedimentary sequence, showing N and NW trends.

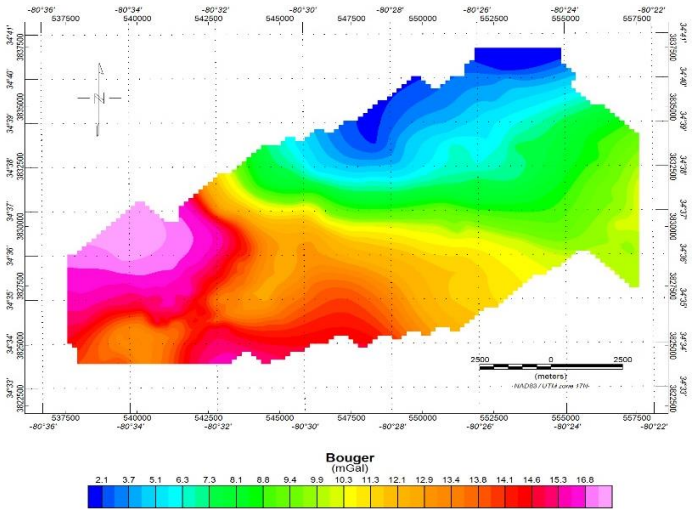

Figure 5.1: Bouguer gravity map

www.manaraa.com

Power spectrum technique:

The fast Fourier transform is applied on the Bouguer gravity grid to calculate the 2-dimensional power spectrum by using Oasis Montaj (Geosoft version 8.5). The power spectrum (figure 5.2) illustrate two linear segments relevant to regional and residual components of the gravity field.

The 2-dimensional power spectrum (figure 5.2) shows deep-seated sources (low frequency end), with wavenumbers < 0.38, and the average depth between 1.5 and 2 km. The high frequency end represents the residual components of Bouguer gravity (figure 5.2), with average depths between 0.5 and 0.1 km.

The Butterworth filtering tool was applied in the wavenumber domain through Oasis Montaj version 8.5. The Butterworth filter tool is carried out on the Bouguer gravity grid; in terms of the filter parameters, the degree of filter function is 8 (default), and the central wavelength cutoff value is 0.28 (cycle/ground).

Regional and residual maps of the Bouguer gravity data are shown in figure 5.3 and 5.4, respectively. The low gravity zone on the northern part of the map, with an amplitude that ranges between 2 and 6 mGal oriented in NE-SW direction, is associated with the Pageland granite. The second zone on the western part of the map is characterized by high gravity, with an amplitude that ranges between 15 and 19 mGal, and is oriented in a NW-SE direction. This zone may be associated with mafic intrusions and/or metavolcanic formations. The third zone is at Haile Mine area, has a medium gravity value that ranges between 13.5 and 15 mGal, and trends NE-SW. This zone is associated with the increase of the thickness of the metasedimentary section.

www.manaraa.com

The residual map (figure 5.4) shows that amplitude values range between - 0.20 and 0.25 mGal. It is characterized by several minor circular and elongated anomalies along the study area. The structural trends are in NW-SE, NE-SW and N-S directions. The western part of the study area at Haile Mine site shows a high amplitude anomalies of 0.15 mGal oriented in NE-SE and N-S trends. Figure 5.5 shows the B-B' geological profile and its location on the residual gravity map.

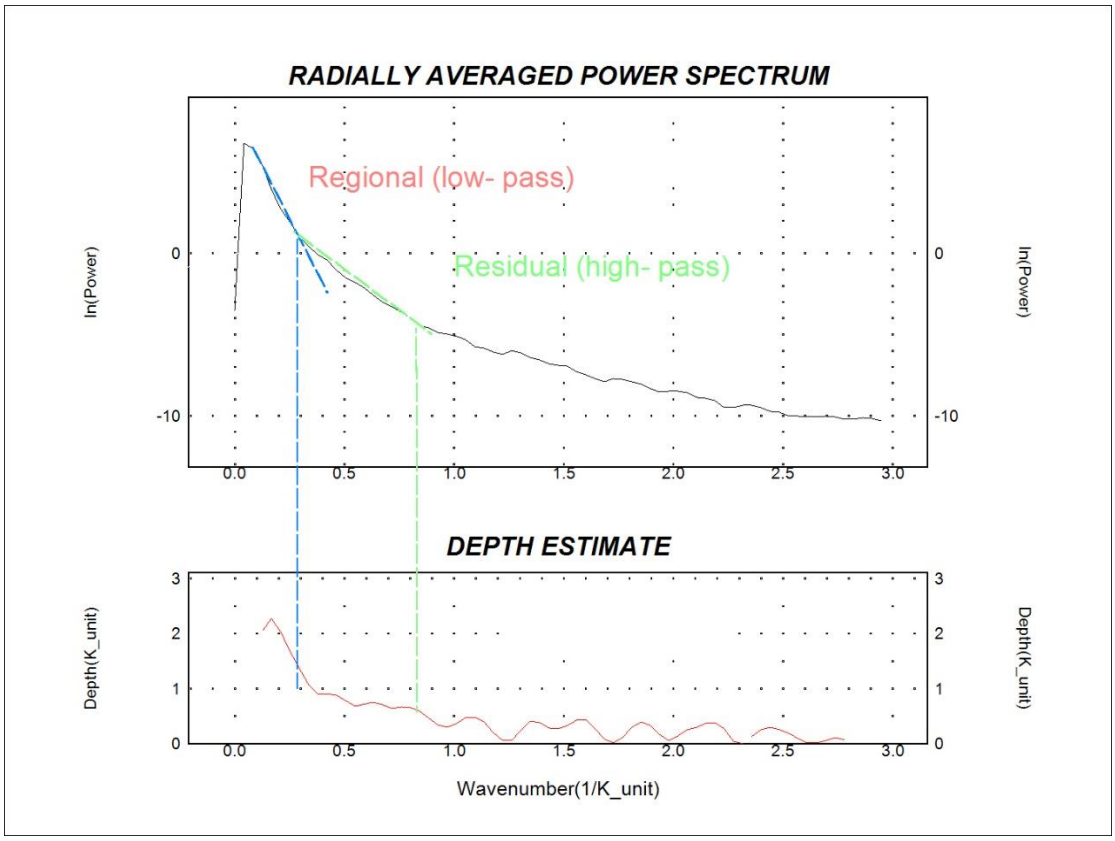

Figure 5.2: The 2-dimensional power spectrum of the Bouguer gravity map.

www.manaraa.com

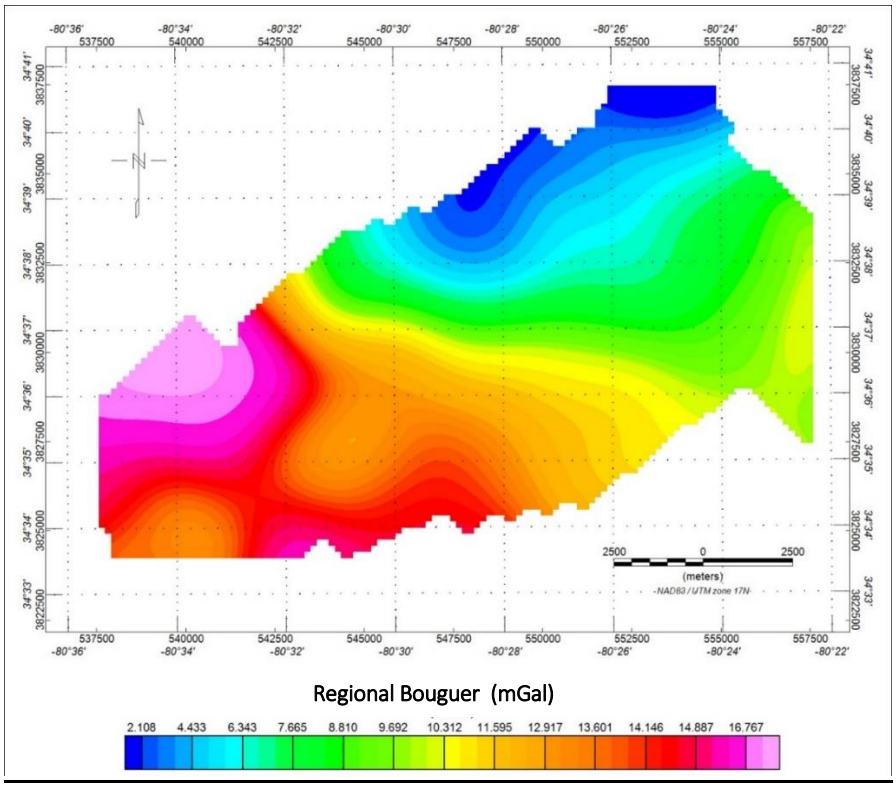

Figure 5.3: The regional Bouguer gravity map.

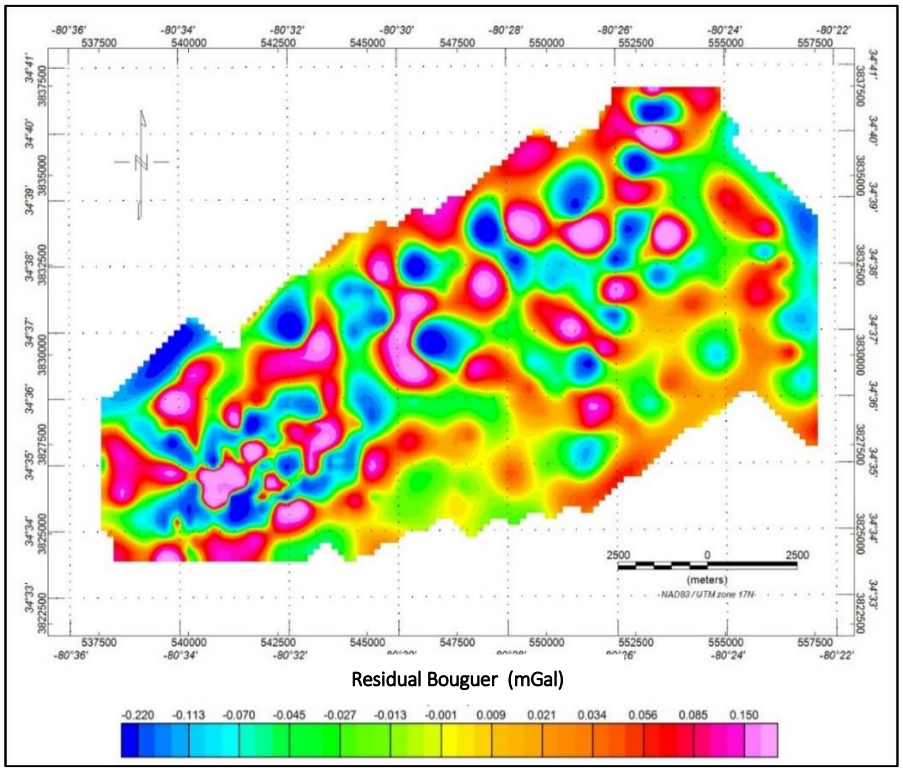

Figure 5.4: The residual Bouguer gravity map.

www.manaraa.com

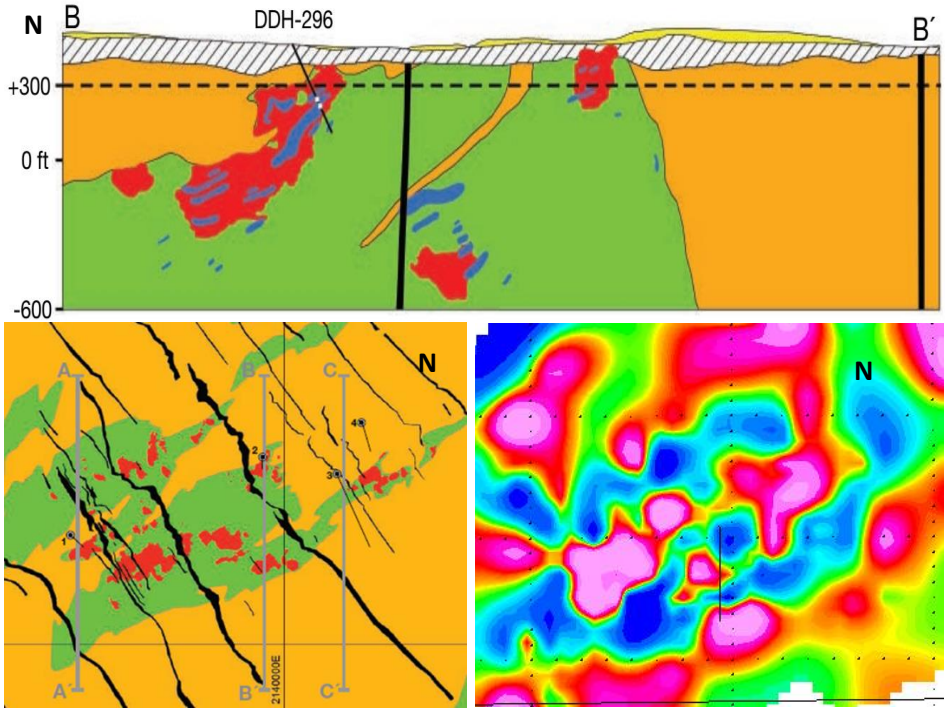

Figure 5.5: The B-B' geological profile and its location on the geological map from Mobley et al. 2014. Expanded view of the residual Bouguer map showing the location of the B-B' geological profile.

3-D Analytical signal (AS) method:

The analytic signal was applied to the Bouguer gravity to provide the source locations of the gravity anomalies, locate the sources edges in both horizontal and vertical dimensions, and determine the main trends of these anomalies. It shows maxima over contacts (Roset et al. 1992), and a maximum value over the edges of the fault/contact.

Figure 5.6 shows a high analytic signal (pink color) located in the west, north, and north-east part of the study area, related to metavolcanics and the Pageland granite (felsic intrusive), respectively. The high values of AS in the west and north part (dotted line) may indicate the contact between metasedimentary and metavolcanic formations. The analytic signal of the Bouguer map over the Haile mine in the western part of study area

www.manaraa.com

(small box in the western side of figure 5.6), shows maximum anomalies over the metavolcanic units and also highlights some of the ore bodies in the Haile Mine area.

Figure 5.7 shows an expanded view to the small box in figure 5.6, where the Haile mine area is located. It shows a geological map overlying the AS of the Bouguer map. High AS anomalies correspond to the areas of ore bodies and metavolcanic units. The metasedimentary rocks show a low AS anomaly.

The positions and trends of some peak analytic signals (red color) at the Haile and the Brewer Mine areas are similar to TDR of the Bouguer and residual maps.

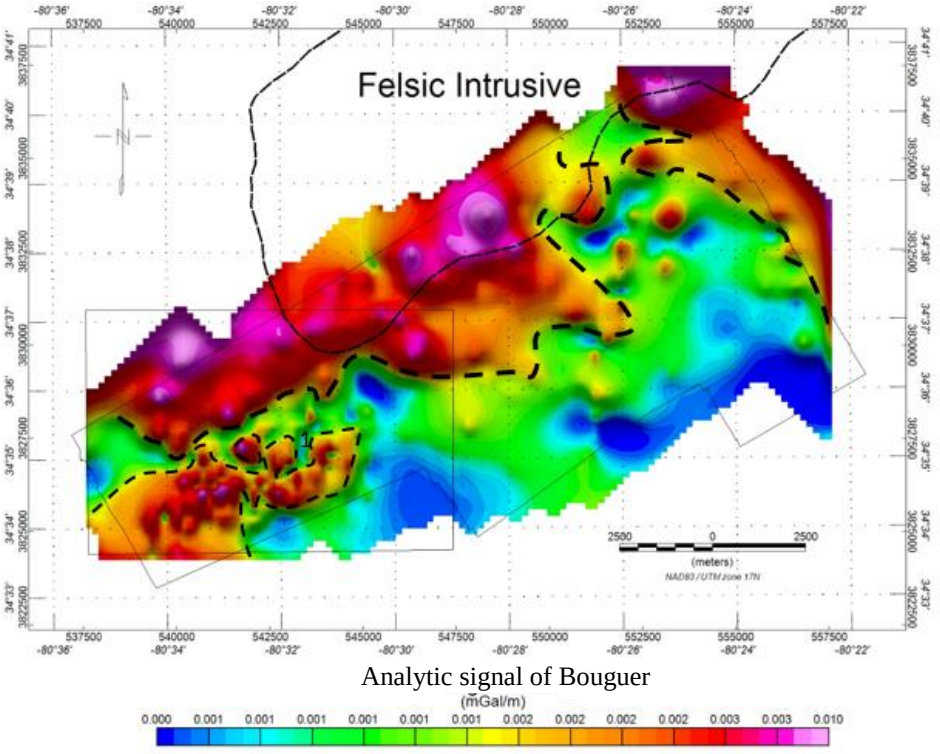

Figure 5.6: The analytic signal of the Bouguer gravity map. Dotted line may refer to the lithological boundaries of the metasedimentary and metavolcanic units.

www.manaraa.com

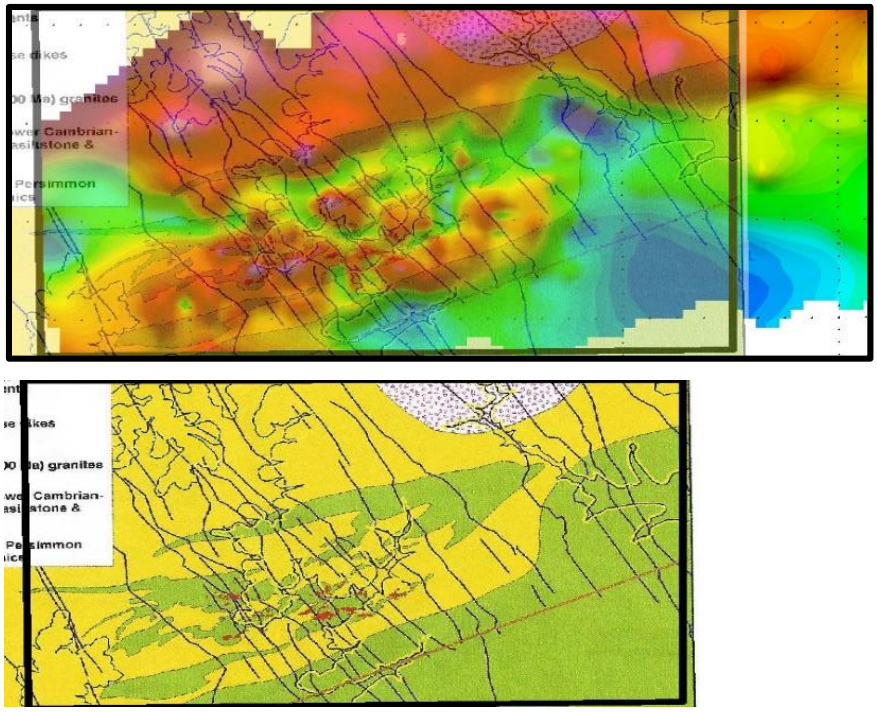

Figure 5.7: An expanded view to the Haile Mine area. The geological map overlies the AS of the Bouguer gravity map. The boundary of the AS map is located in the western part of figure 5.6.

Tilt Derivative method (TDR):

The tilt derivative was applied to Bouguer gravity and its regional and residual maps to enhance the subsurface structure and determine the depths and locations of the vertical contacts and faults of the sources bodies without prior knowledge about the source by using the first horizontal and vertical derivatives. The TDR represent both the shallow and deep sources.

The TDR map results helps predict the horizontal location and extent edge of anomaly sources by assuming a vertical contact model. The tilt derivative maps show the range of the amplitudes is from -1.57 to 1.57 radial. So, the zero contour line is located over or near the contact source, where the vertical derivative is zero and the horizontal

www.manaraa.com

derivative is maximum and is negative outside the anomaly source region, while the TDR is positive when it passes over the edges of the source.

The TDR map of Bouguer (figure 5.8) shows the boundary of the metasedimentary formation in the west part over the Haile main area. The zero contour line in the north part of the study area outlines the edge of the felsic intrusion, similar to the edge location that results from the shaded relief of the RTP magnetic map.

The TDR of the regional Bouguer gravity map (figure 5.9) indicates the possible regional boundary of the metasedimentary units in the Haile Mine area. The felsic intrusive edge is clearly seen. The zero contours produce an elongated zone in NW and NE direction, in the west, center, and east part of the study area. The metavoclanic unit and mafic dikes are characterized by positive tilt derivatives; the lithological boundary of the metavolcanic rocks has been superimposed over the tilt derivative of the regional Bouguer map (figure 5.10).

The TDR of residual Bouguer map (figure 5.11) shows that the main structural trends of these anomalies are NE-SW and NW-SE. Some of these lineament edges (figure 5.11) are following faults. South of the Haile Mine area the contact of the metasedimentary formation is shown clearly by positive tilt derivative as a NE trend. Figure 5.12 shows an expanded view of the Haile Mine area. The ore is characterized by a positive tilt derivative and has a NE trend.

www.manaraa.com

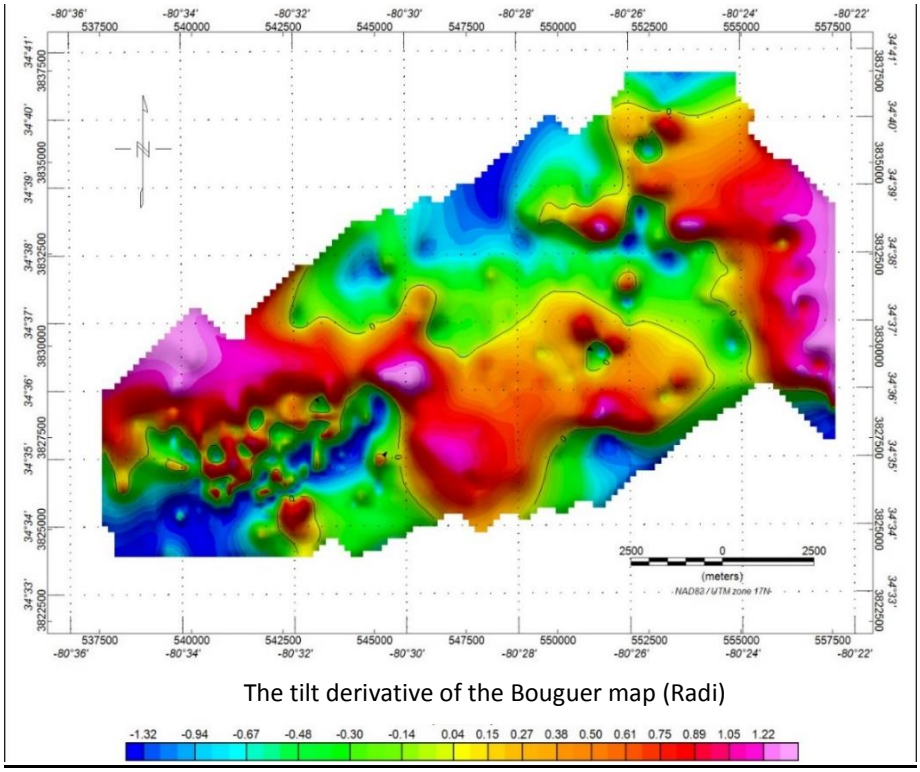

Figure 5.8: The tilt derivative of the Bouguer map. Solid line indicates the zero radial contour. The polygon is the boundary of the study area.

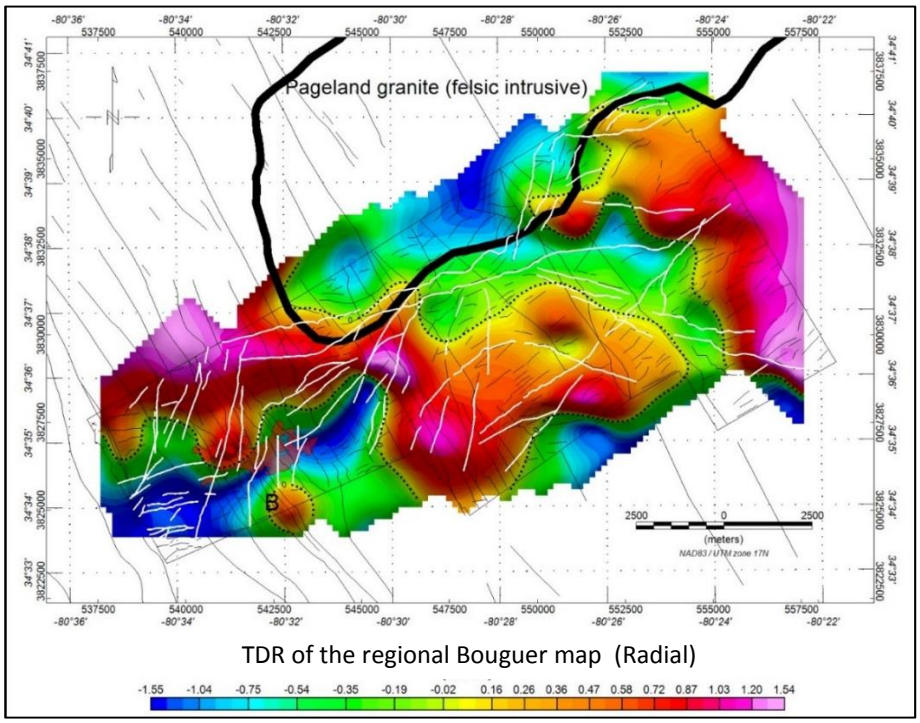

Figure 5.9: The TDR of the regional Bouguer map. Dotted lines are the zero contours. The thick line is the felsic intrusion from OceanaGold's geological map.

www.manaraa.com

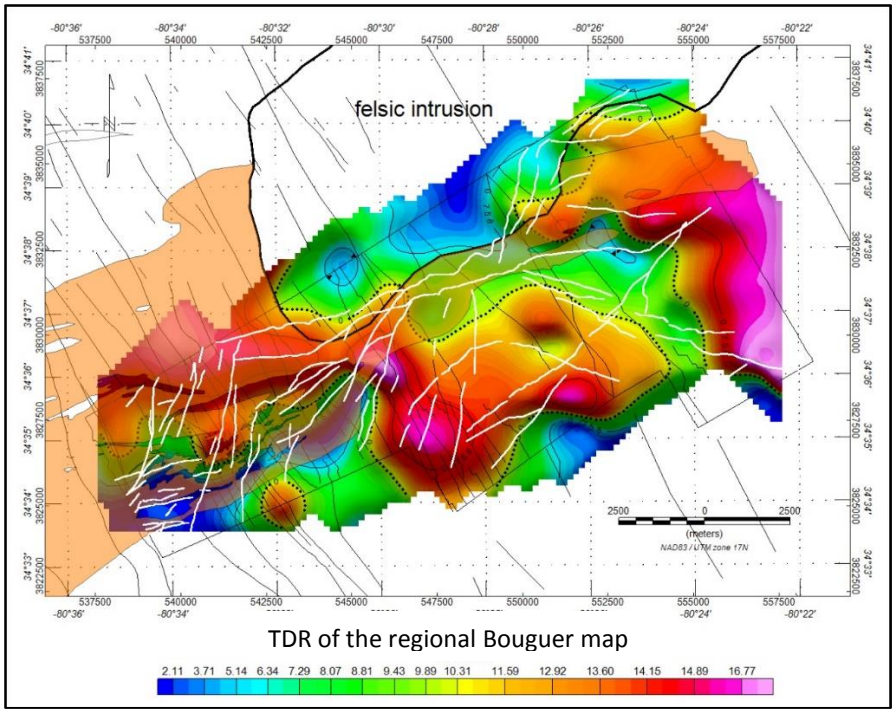

Figure 5.10: The TDR of the regional Bouguer map. The geological map from OceanaGold overlies the TDR of regional Bouguer map. The orange color of the geological map indicates the lithologic boundary of the metavolcanic formation. The NW lines are mafic dikes. The white lines are possible faults.

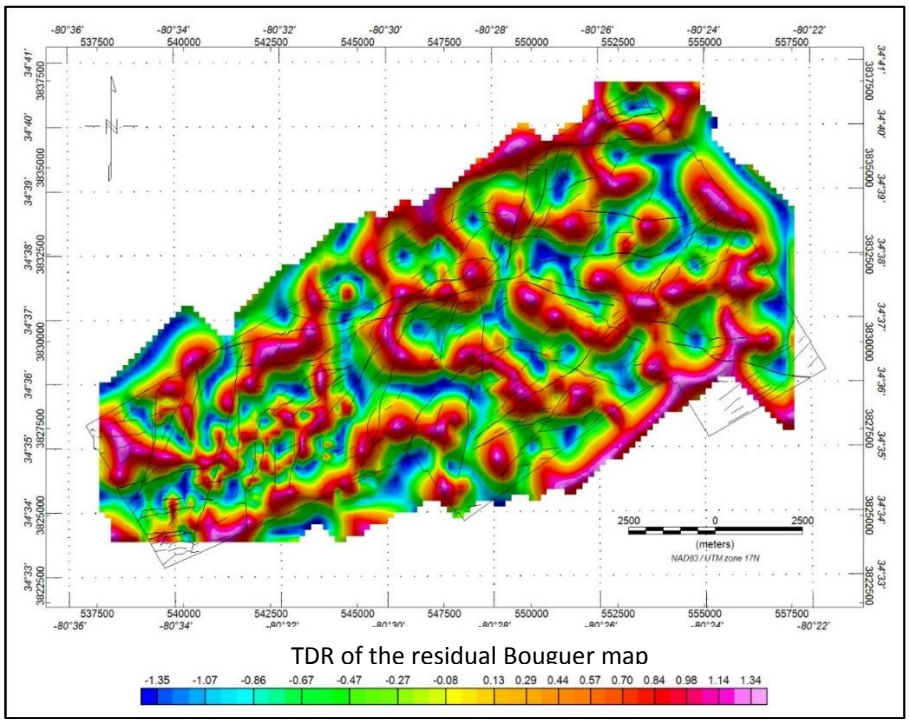

Figure 5.11: The TDR of the residual gravity map. Some of these lineament edges are following the faults. The solid lines are possible faults from geological map.

www.manaraa.com

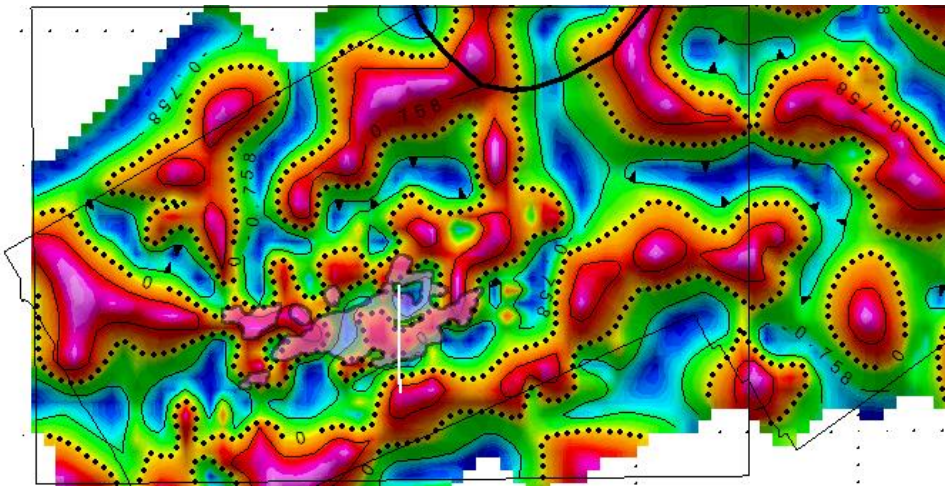

Figure 5.12: Expanded view of the Haile Mine area. White line is the B-B' profile. Pink polygon is the ore body from OceanaGold's geological map.

Source Parameter Image method (SPI):

The source parameter image is applied on the Bouguer gravity map by using Geosoft software to estimate the depth of gravity sources and locate the source contact. The inversion of the local wavelength corresponds to the contact depth, where the warm color indicates a high wavelength and cold color indicates the low wavelength. The color bar show the inverse of the local wavelength, it has units of meter.

Based on the SPI statistic report figure B.1, the depth of gravity sources range from 101 to 28965 m. Figure 5.13 shows the solution grid of SPI. It shows the edge locations and depths of anomaly sources. The blue color shows that area of the shallow gravity sources and the red color shows the area of deep gravity sources. The source depths over the Haile Mine area are shallow.

The SPI solutions indicate the contact locations, depths, and structural trends. The SPI solutions are shown in figure 5.14 and 5.15. As indicated from the SPI method figure 5.14 and 5.15, the yellow contacts are present at depths less than 500 m, where the red

www.manaraa.com

are present at depths between 500 to 1500 m, while the green square are present at depths between 1500 to 2000m. Finally, the purple and blue circle are present at depths between 2000 to 2500 m and above 2500 m, respectively.

Figure 5.15 shows the structural trends of the SPI solutions. Line A-A' is the same trend as seen in the residual Bouguer, analytic signal of residual Bouguer, and tilt derivative of the TMI and its regional map. Line B-B' has the same trend as observed in the residual Bouguer and the analytic signal of the residual Bouguer gravity map. Line B-B'' shows a half circle feature, similar to a feature as the SPI of the magnetic field, an oval pattern around the Brewer Mine area that may related to the Richtex/Persimmon Fork contact.

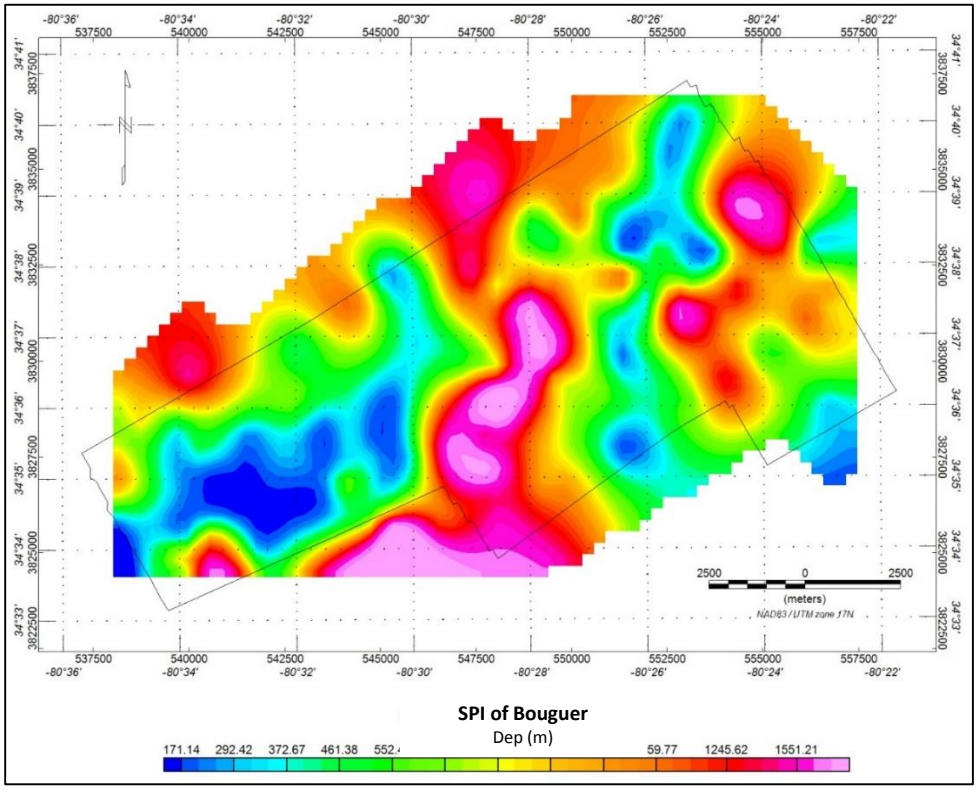

Figure 5.13: Source parameter image of Bouguer gravity (depth estimate grid).

www.manaraa.com

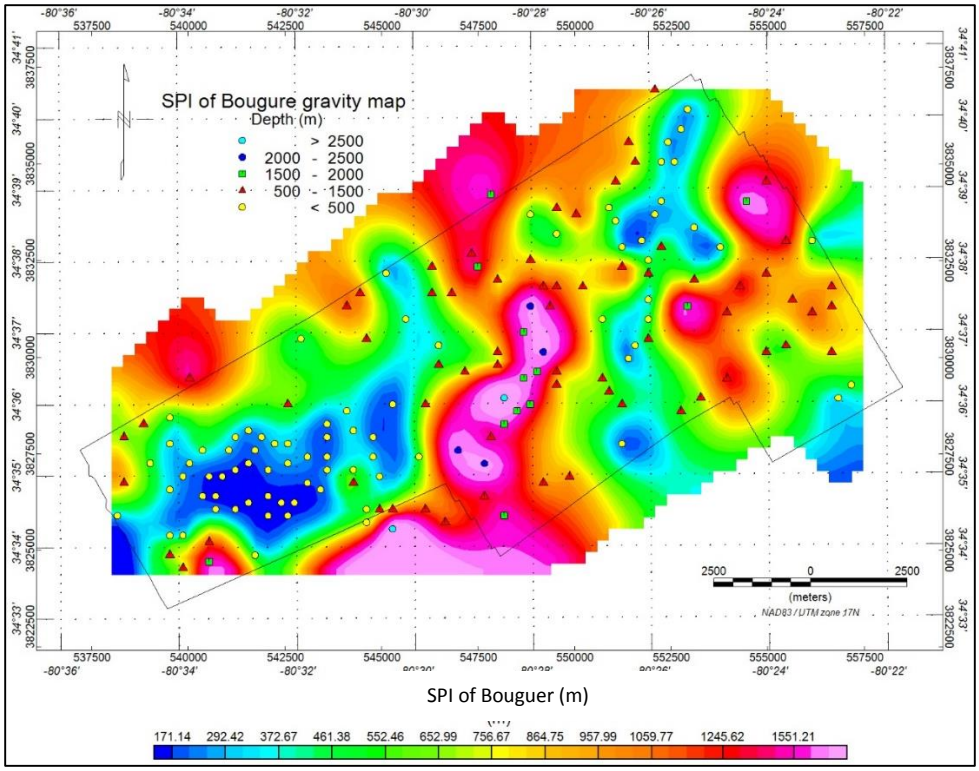

Figure 5.14: SPI solutions plotted on the SPI of the Bouguer map.

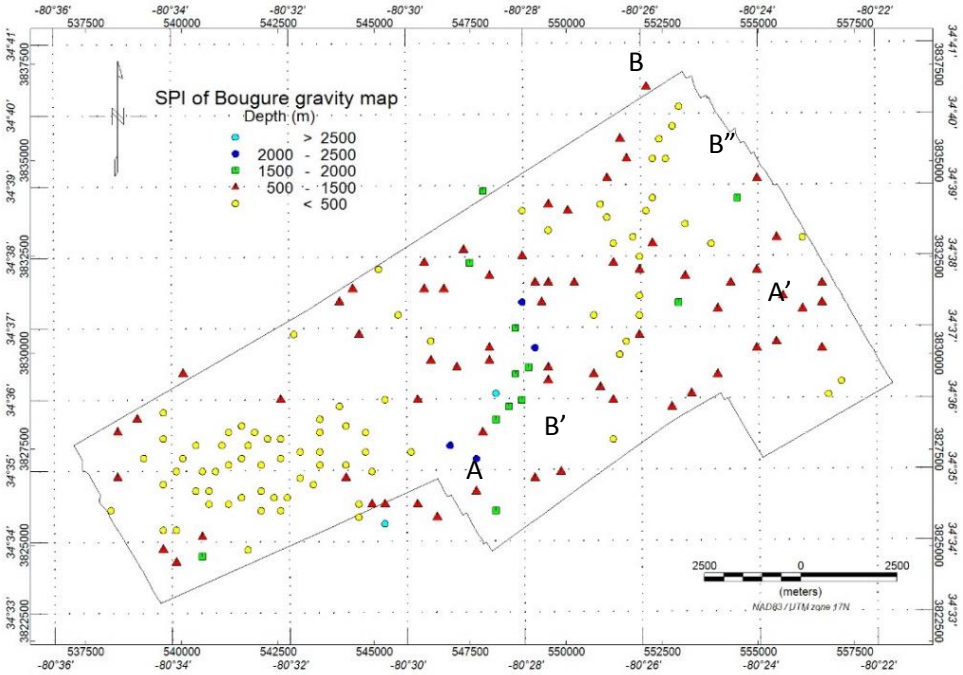

Figure 5.15: SPI solutions of Bouguer gravity map.

www.manaraa.com

3-D Euler deconvolution (ED):

The Euler deconvolution (ED) method was applied to the 2nd vertical derivative of the Bouguer gravity field (figure 5.16). Note the numerous shallow solutions in the Haile Mine area, the southwest part of the study area. NNE trend B – B' is a possible fault and/or contact. This trend is similar to one observed in the gravity residual and ED, and magnetic TDR. ENE trend A – A' can also be seen in the residual, SPI and AS of the Bouguer map.

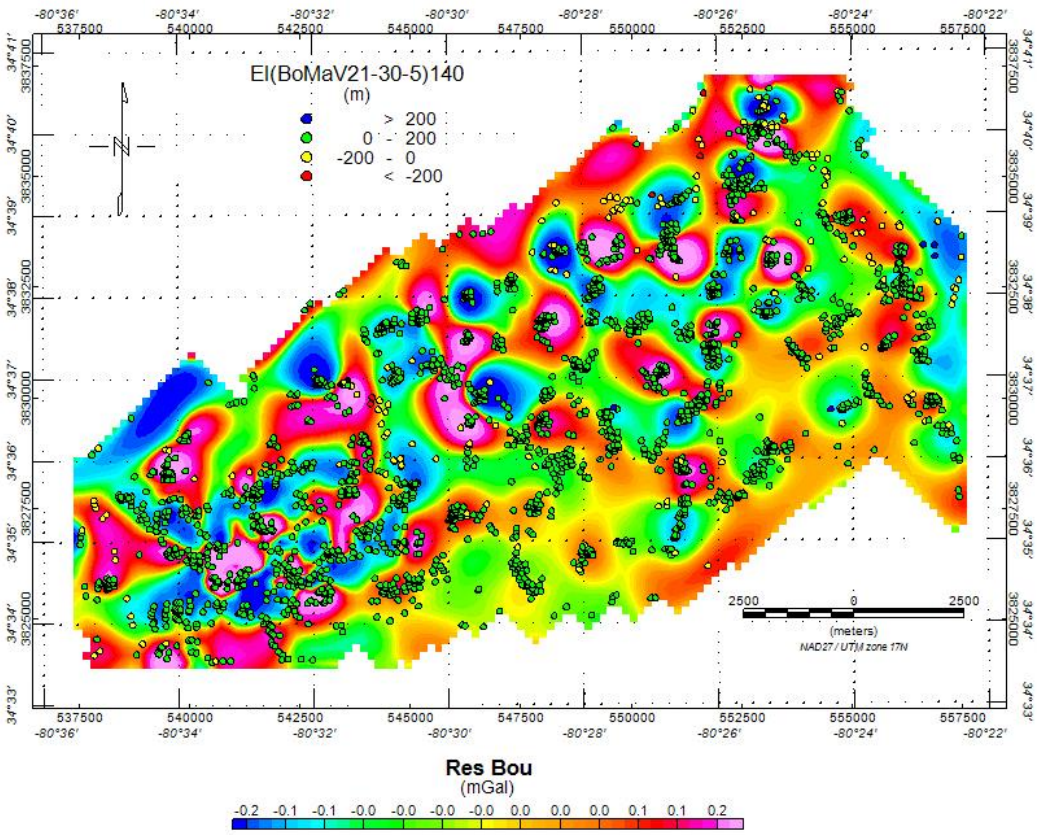

www.manaraa.com

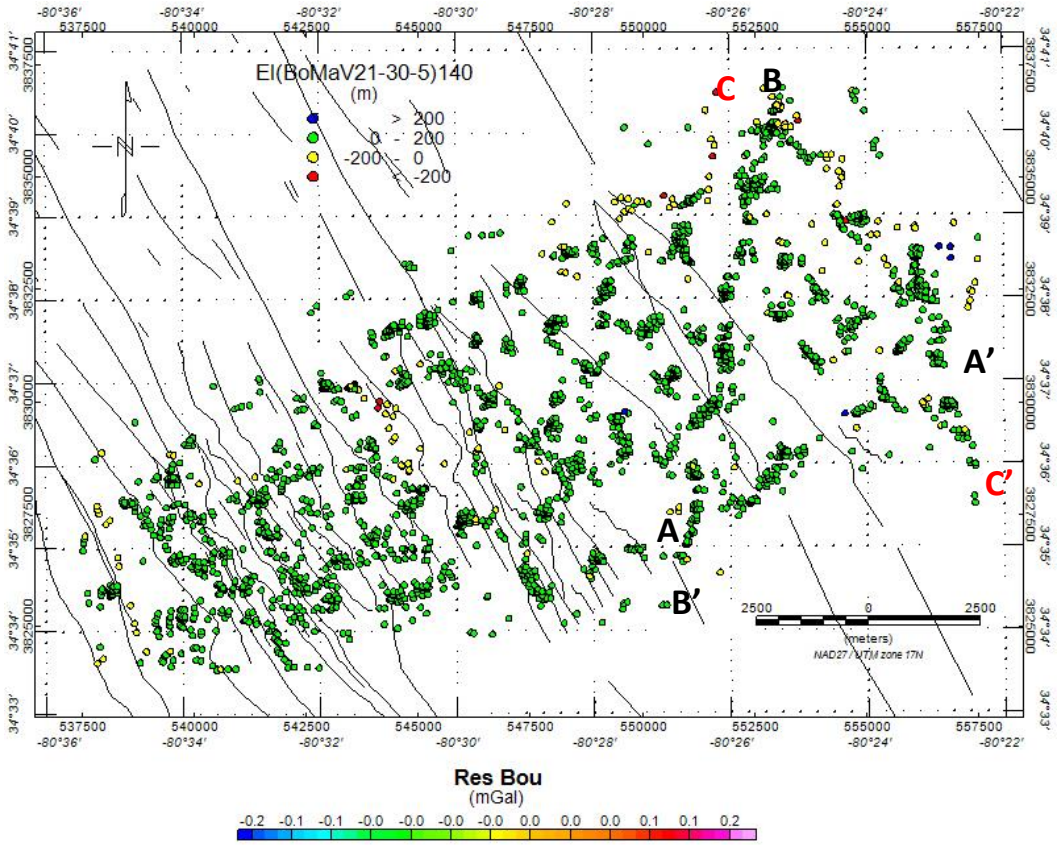

Figure 5.16: The Euler deconvolution solutions of 2nd vertical derivative of the Bouguer map. The structural index is 1 which represents contacts. The Euler solution depths plotted on the residual Bouguer map (above) and without the gravity map (below). The window size is 5. The Euler deconvolution solutions follow the dikes. A NNE trend (B-B') is a possible fault and/or contact. A NW trend (C-C') is follow the Jurassic dikes trend. An ENE trend (A-A').

2-D gravity modeling:

The two dimensional forward gravity model was generated by using Oasis Montaj and 2-D GM-SYS software along the B-B' geological section from (Mobley et al. 2014). The gravity model is defined by the correlation of rock density value from diverse sources "Berry (2013), Donald et al. (2008), and Snider et al. (2014)". Along the profile, the horizontal axis represents the distance in meters. The vertical axis displays the gravity field in mGal and the lower section displays the depth in meters.

www.manaraa.com

In the study area, the initial density values (table 5.1) are used for metasedimentary, metavolcanic, coastal plain, saprolite, dikes, and ore. The Bouguer reduction density is 2.69 gm/cc. The final model result (figure5.17) shows a good fit between calculated gravity (solid line) and the observed (dotted).

To model one of the ore bodies that is located on the right side of figure 5.17, the ore density values were assumed to vary from 2.75, 2.80, and 2.85 gm/cc, and the metasedimentary densities value range from 2.72 to 2.75 gm/cc. The average density value of the pyrite, molybdenite, and gold were derived from (Carmichael 1989) and (Telford1990) (table 5.2). The average density of pyrite and molybdenite is 5.0 gm/cc and gold is 18.0 gm/cc.

Figure 5.18 shows the same density values as figure 5.17, the Richtex density value is 2.72 gm/cc and the ore body density is 2.80 gm/cc. The calculated (solid line) fits the observed gravity (dotted).

1) If we assume that the ore density is due to pyrite and molybdinite (5 gm/cc);

$2.72\ X + (1-X)\ (5.0) = 2.8$

$X = 0.96$

Then ore body is 4% pyrite and molybdenite and 96% Richtex.

If we assume that the anomaly is mainly due to the presence of gold (18 gm/cc),

$2.72\ X + (1-X)\ (18.0) = 2.8$

$X = 0.99$

Then the ore body is 1 % gold.

www.manaraa.com

2) By increasing the Richtex density (figure 5.19) from 2.72 (dashed line) to 2.75 gm/cc (solid line), the density model does not fit the observed gravity (dotted line).

3) By changing the density of the ore body (figure 5.20) from 2.80 (dashed line) to 2.75 gm/cc (solid line) and keeping the Richtex density 2.72gm/cc, the density model does not fit the observed gravity (dotted) as well.

If ore density is 2.75 gm/cc and Richtex = 2.72 gm/cc,

$2.72\ X + (1-X)\ (5.0) = 2.75$

$X = 0.99$

Then 1% is pyrite and molybdenite.

If we assume that the anomaly is mainly due to the presence of gold (18 gm/cc),

$2.72\ X + (1-X)\ (18.0) = 2.75$

$X = 0.998$

Then the ore body is 0.2% gold.

5) By changing ore body density (figure 5.21) to 2.85 gm/cc (solid) and keeping the Richtex density of 2.72 gm/cc, the density model does not fit observed gravity as well.

Table 5.1: The initial densities value.

Unites	Density value
Richtex (MS)	2.72 gm/cc
Persimmon Fork (MV)	2.73 gm/cc
Coastal Plain	2.63 gm/cc
Saprolite	2.12 gm/cc
Dikes	2.86 – 3.0 gm/cc
Ore bodies	2.79 – 2.8 gm/cc

www.manaraa.com

Table 5.2: Mineral densities value.

Minerals	Densities		References
Pyrite	5.1 g/cc	4.95.2g/cc	(Carmichael 1989) ; (Telford1990)
Gold	19.3 g/cc	15.6-19.4g/cc	(Carmichael 1989) ; (Telford1990)
Molybdenite	4.999g/cc	4.4-4.8g/cc	(Carmichael 1989) ; (Telford1990)

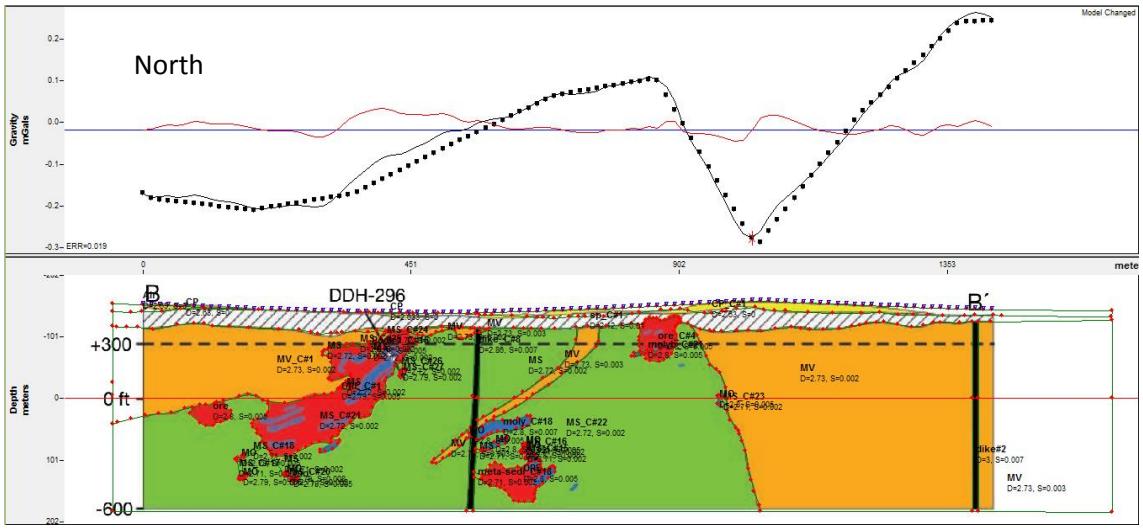

Figure 5.17: 2-D density model. North is on the left side of the profile.

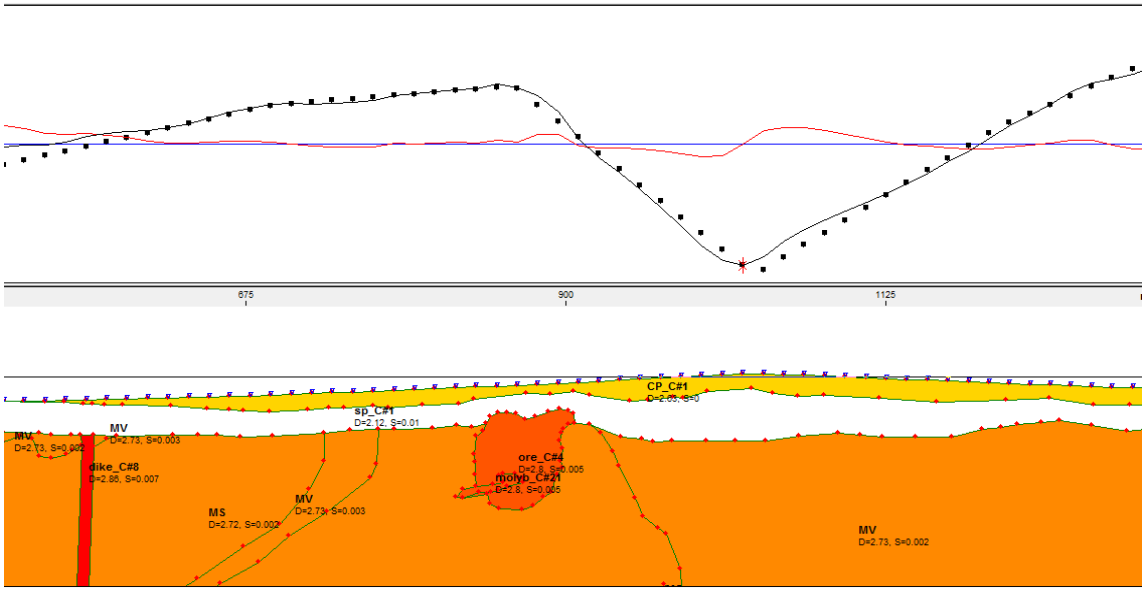

Figure 5.18: The 2-D density model zooms in to one of the ore bodies that is located on the right side of figure 5.17. MV metavolcanic (light orange); MS metasedimentary (light orange); CP coastal plain (yellow); SP saprolite (white); dike (red); ore (orange).

www.manaraa.com

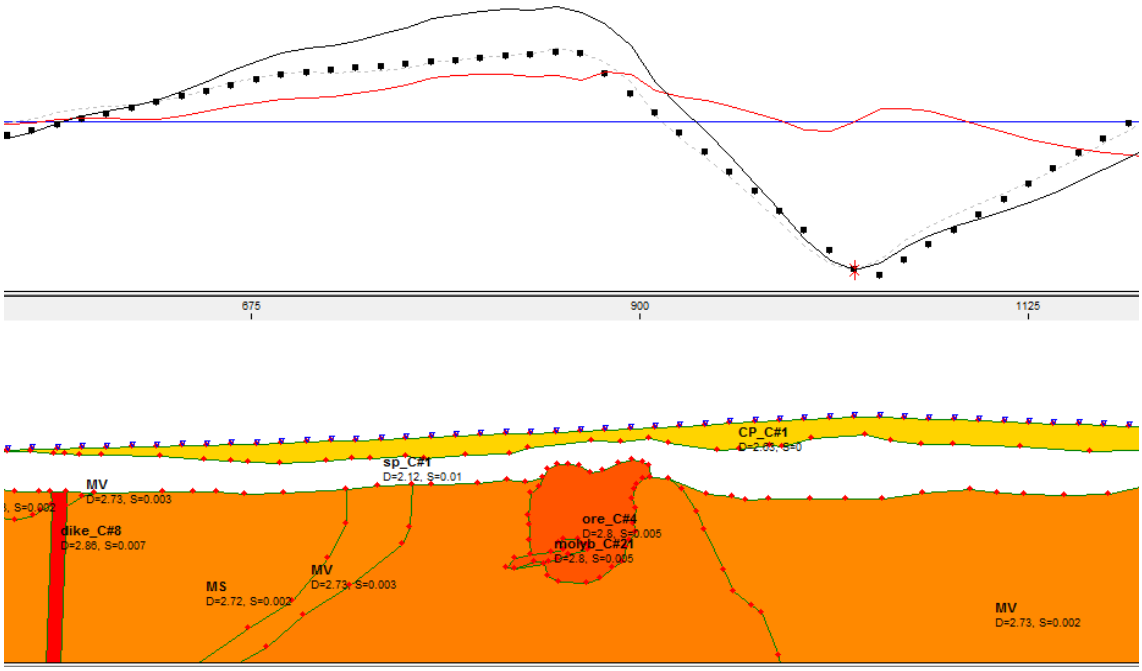

Figure 5.19: The Richtex = 2.75 gm/cc (solid), Richtex = 2.72 gm/cc (dashed), and Ore = 2.8 gm/cc. Calculated anomalies do not fit the observed gravity (dotted line).

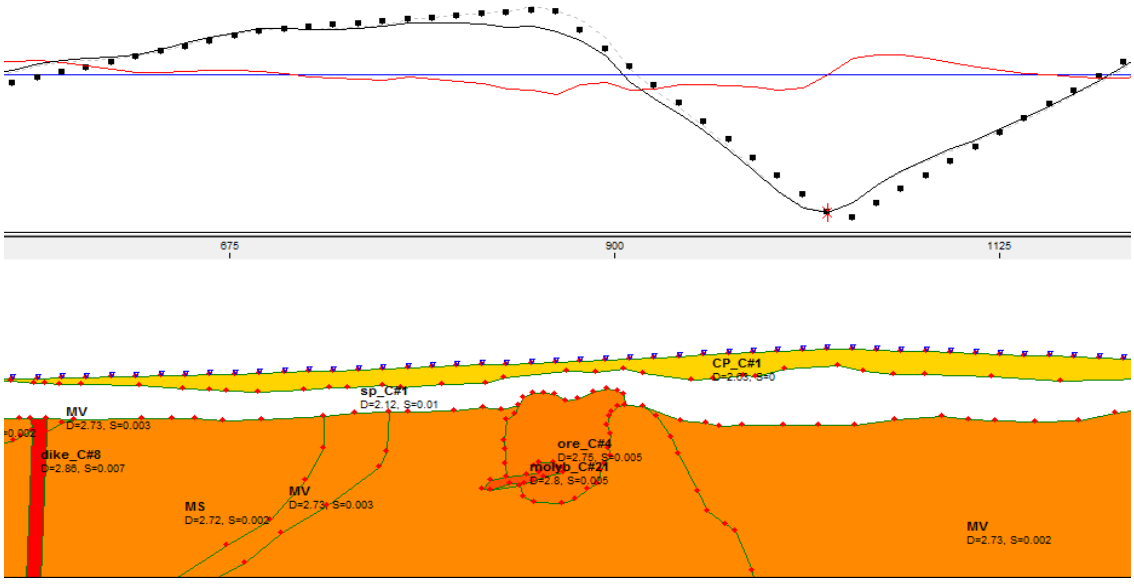

Figure 5.20: The Richtex = 2.72 gm/cc, ore = 2.75gm/cc (solid), and ore = 2.80 gm/cc (dashed). Calculated does not fit the observed gravity (dotted line).

www.manaraa.com

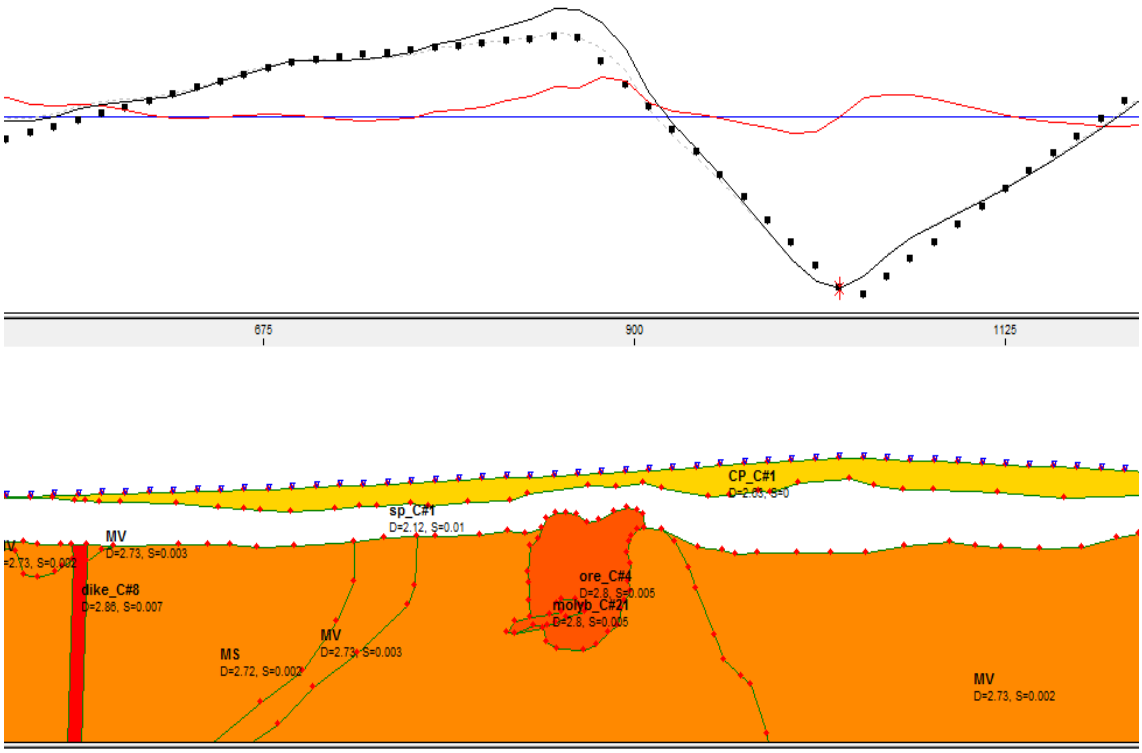

Figure 5.21: The Richtex = 2.72 gm/cc, ore = 2.85 gm/cc (solid line), and ore = 2.80 gm/cc (dashed line).

5.2 Magnetic Data Results

Total magnetic intensity (TMI)

The total magnetic intensity anomalies in the study (figure 5.22) area range between 49884 and 50441 nT. Maximum magnetic values (pink color) of 50441 nT are observed over granites and have a structure tend of NE-SW. The elongated anomalies (red and pink colors) are associated with the NW-SE Jurassic dikes. In general, the metasedimentary formation shows a lower magnetic intensity than the metavolcanic formation.

www.manaraa.com

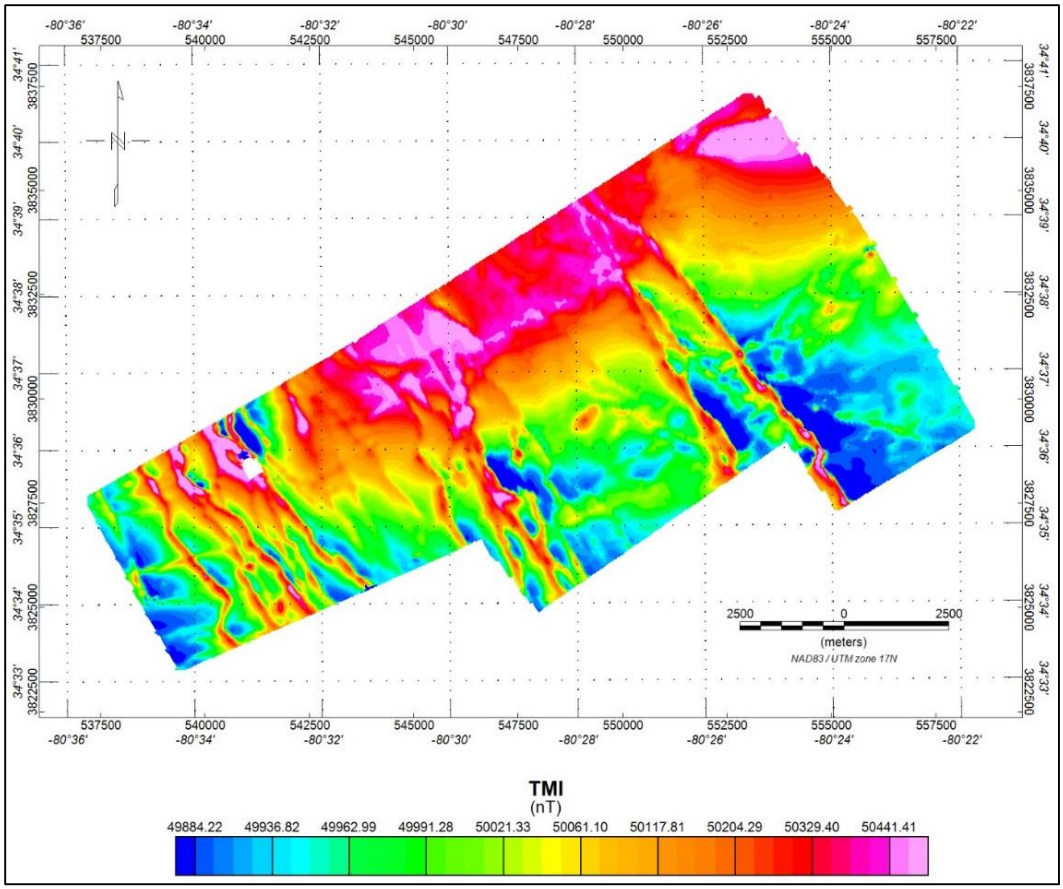

Figure 5.22: Total magnetic intensity of the study area.

Reduce to the pole (RTP)

The total magnetic intensity was analyzed using the reduced to pole method to reduce the effect of magnetic variations caused by the dipole magnetic field. This filter migrates the observed field from observation inclination and declination to what the field would look like at the magnetic pole. This aids in the interpretation since any asymmetry in the reduced to pole field can then be attributed to source geometry and/or magnetic properties (Geosoft). The anomalies in the RTP magnetic map will be directly located above the source. This method uses inclination and declination values of 63^0 and -7.20^0.

www.manaraa.com

In general, the RTP map (figure 5.24) shows no difference from the total magnetic intensity map, except for some anomalies exposed in the study area. Due to the inclination and declination removal, many high anomalies are present in the central part of the area. The RTP map highlights ENE trends in the central part and under the coastal plain which may be related to Alleghanian (alkaline) dikes or ore bodies.

The NE-SW and NW-SE trends (Alleghanian and Jurassic dikes respectively) have high values of magnetic anomalies between 50050 to 50300 nT. The highest value is about 50444 nT and is located in the northern part and directed NE-SW, related to the Pageland granite (felsic intrusion).

A profile over the 2-D density model (Figure 5.23) shows the total field and Reduced to Pole (RTP) magnetic anomalies. An RTP anomaly is located directly above the dike. Small anomalies over ore bodies are also suggested in the total field and RTP magnetic anomaly profiles.

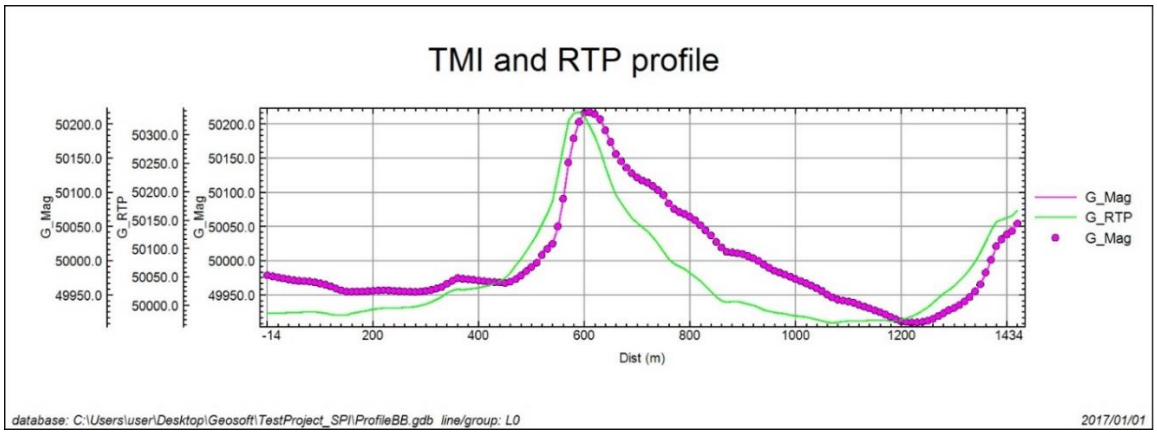

Figure 5.23: The magnetic anomaly of the total field before and after the reduced to the magnetic pole is applied over the 2-D density model. The anomaly of the reduced to magnetic pole is directly located above the source. North is on the left side of the profile.

www.manaraa.com

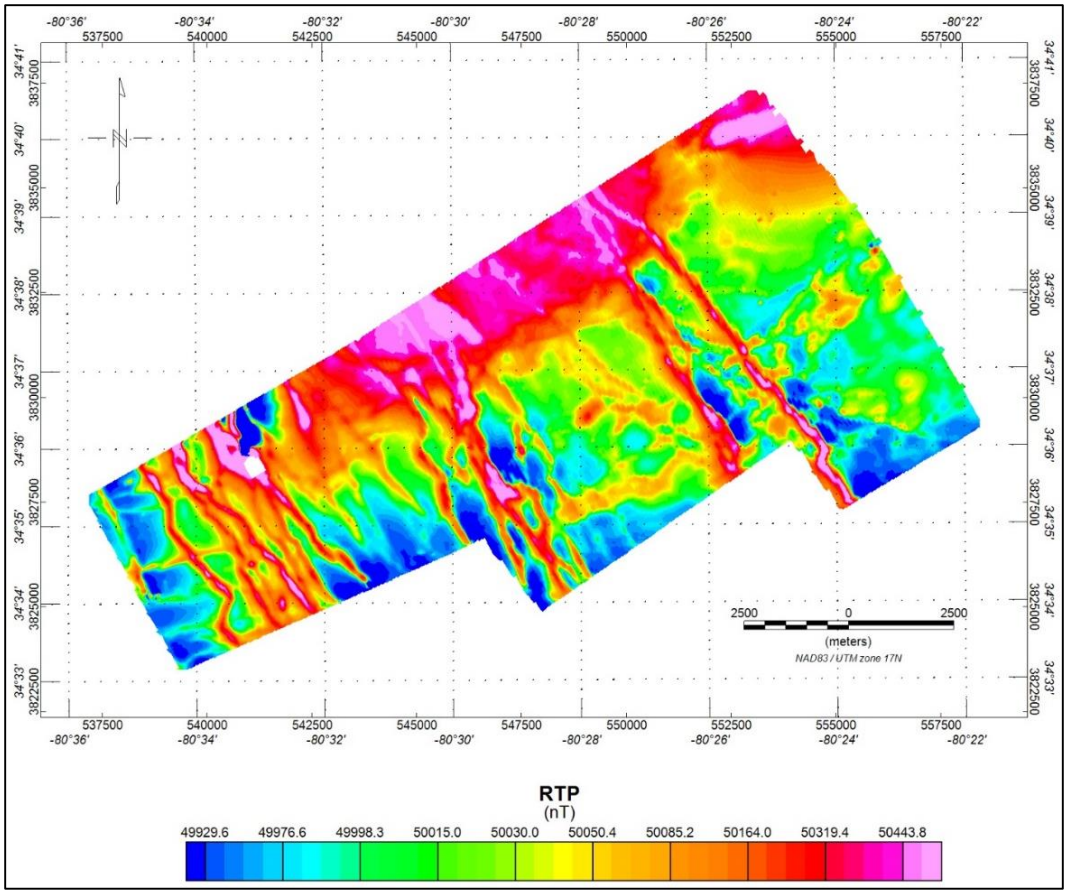

Figure 5.24: The reduced to the pole map (RTP).

Shaded-relief:

The shaded relief map of reduce to pole (figure 5.25) presents many linear magnetic anomalies that were not apparent on the TMI map. The shaded relief map clearly illuminates the Pageland granite contact. The map indicates the NW-SE and NE-SW structural trends, the Jurassic and Alleghanian dikes, respectively. Several minor structural trends are also shown in figure 5.25, associated with a possible faults and/or geological contacts.

www.manaraa.com

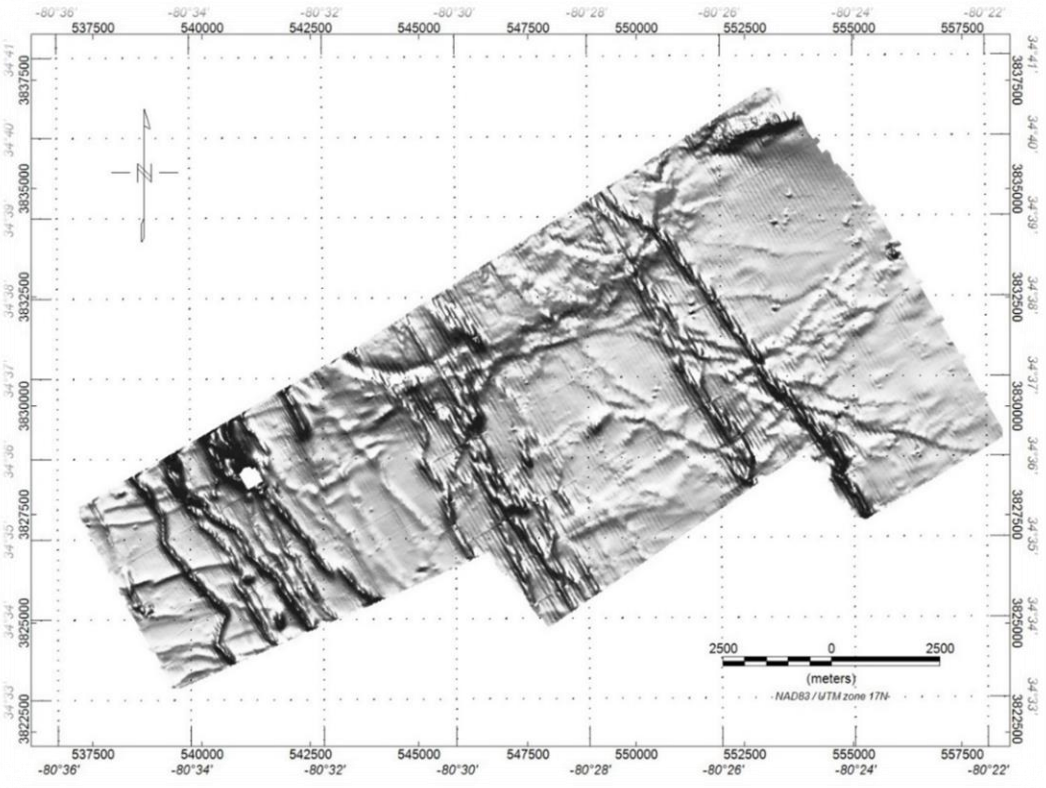

Figure 5.25: The shaded relief map of reduced to the magnetic pole.

Power spectrum technique (PS):

The 2-dimensional power spectrum (figure 5.26) shows a deep-seated source (low frequency) with a wavenumber < 0.9. The average depths of the low frequency magnetic sources range between 1 and 0.5 km. The high frequency end represents the residual components of total magnetic intensity, the average depths of the high frequency magnetic sources is between 0.1 and 0.5 km.

The regional map (figure 5.27) shows the same main structural trends of total magnetic intensity (TMI) but with different anomalies, value ranges, and smoothness. The map shows two major deep-seated features, NW-SE Jurassic dikes and felsic intrusion (granites).

www.manaraa.com

The residual total magnetic intensity (TMI) map (figure 5.28) shows magnetic values ranging between -100 and 145 nT. The Alleghanian dikes are enhanced and interpreted as NE-SW trends in the western part of the study area. The narrow elongated magnetic highs trending NW-SE are associated with diabase (Jurassic) dikes. Also, possible faults may offset the diabase dikes.

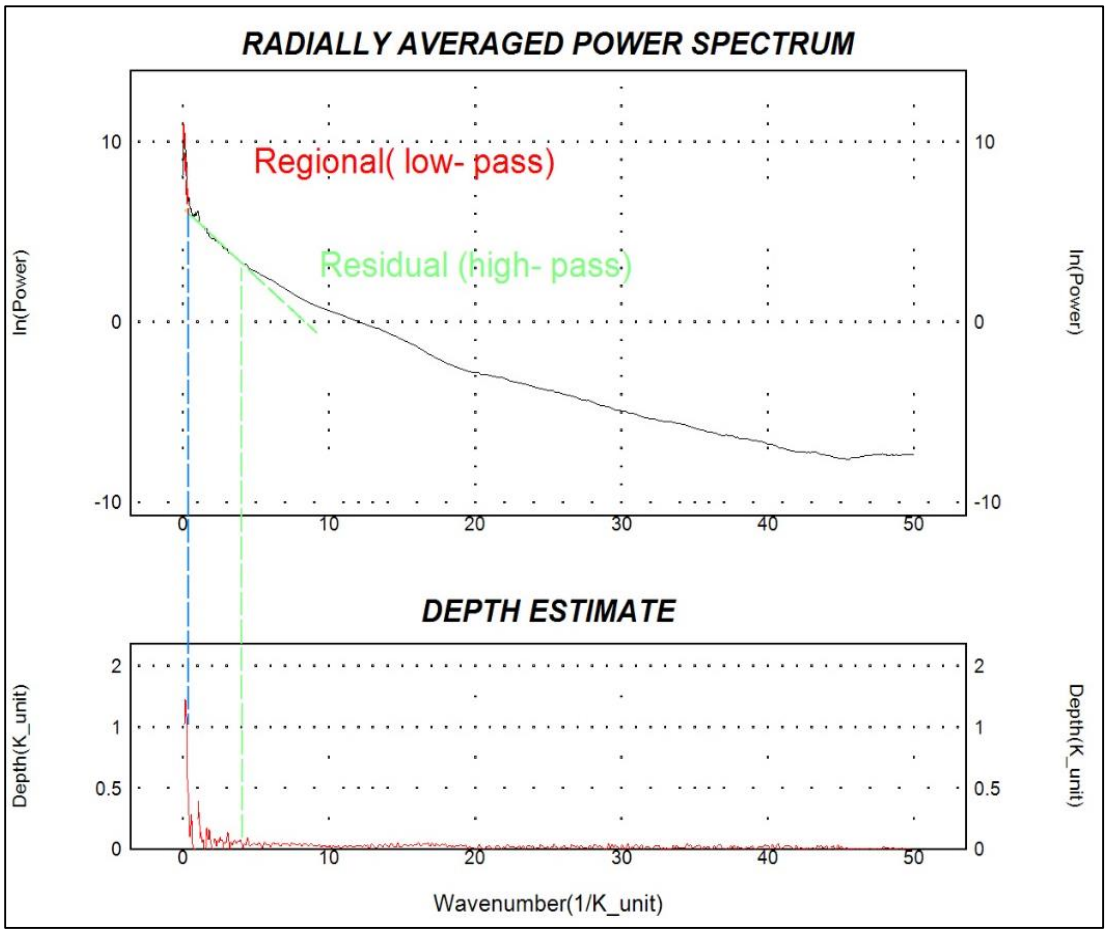

Figure 5.26: 2-D power spectrum of total magnetic intensity data.

www.manaraa.com

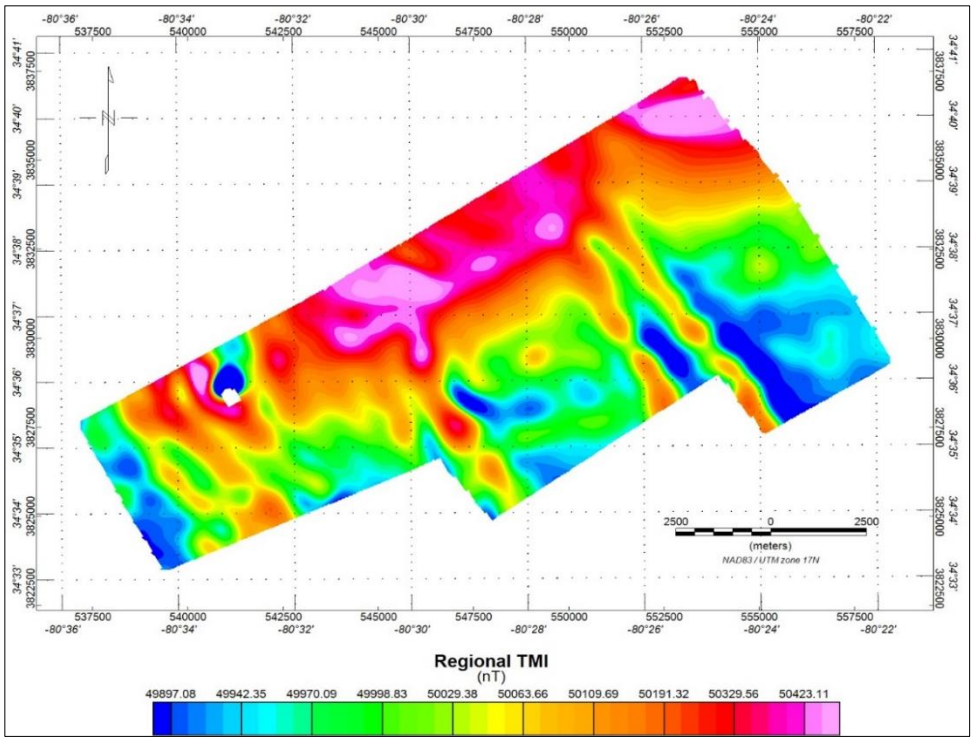

Figure 5.27: The regional total magnetic intensity map.

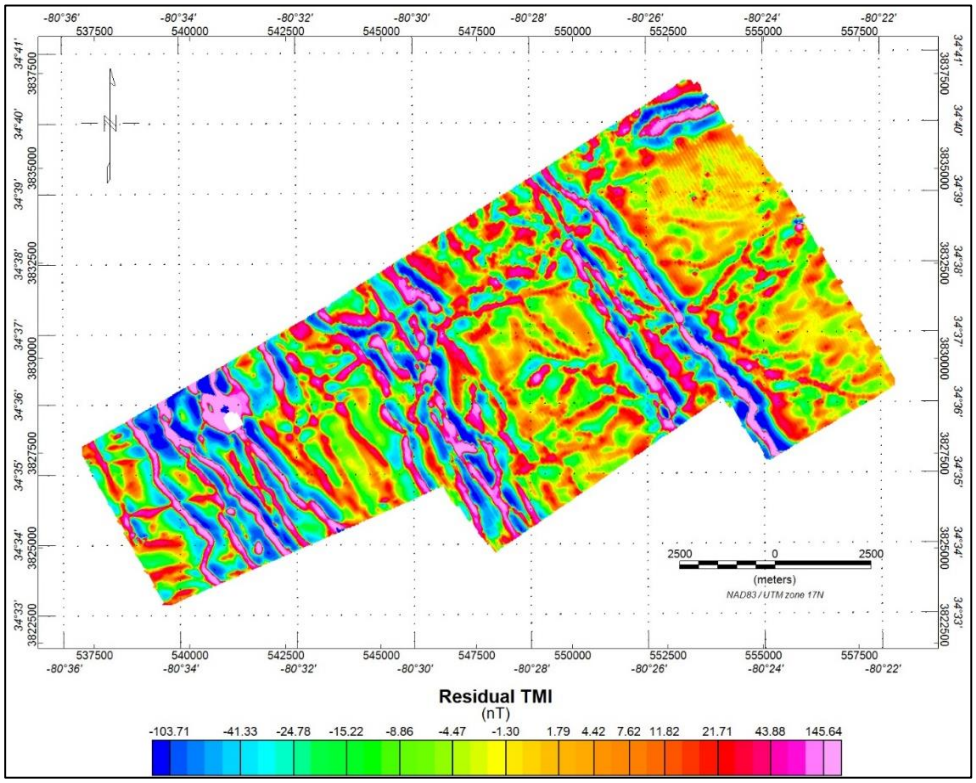

Figure 5.28: The residual total magnetic intensity map.

www.manaraa.com

Analytical signal (AS) method:

As the analytic signal (AS) calculation is independent of the directions of the Earth's magnetic field, anomalies will be correctly shifted to the top of the source bodies, no need to apply the AS over the RTP map. The analytic signal map in figure 5.29 shows maximum anomalies over the source edge contacts and the main trend directions of these anomalies.

The AS map shows the diabase dikes trending NW-SE as well as the granite edge contact (felsic intrusive). The directions and positions of these anomalies are similar to those in the TDR and shaded relief maps of total magnetic intensity. The ENE-trending anomalies in the central part of the study area that were highlighted after applying the reduced to pole filter are seen in the AS map (figure 5.29).

Upward continuation of 70 m is applied to the AS of total magnetic field map to filter out the effects of near-surface features that are unlikely to be interest and for a better demonstration of the contact location (figure5.30). Morrell et al. 2011, used analytical signal to define the boundaries of a magnetic quiet zone that they interpreted as an area of hydrothermal alteration. A circular low analytic signal in the northeast part of the study area indicates the hydrothermal alteration zone of the Brewer Mine area. In the central part of the study area a similar analytic signal feature to the Brewer Mine may also be an area of hydrothermally altered rock.

In order to improve the dynamic resolution of the image, the color scale was changed to highlight the maximum anomalies as shown in figure 5.31. The dikes and felsic intrusive contacts are clearly seen in the upward continuation of the AS map.

www.manaraa.com

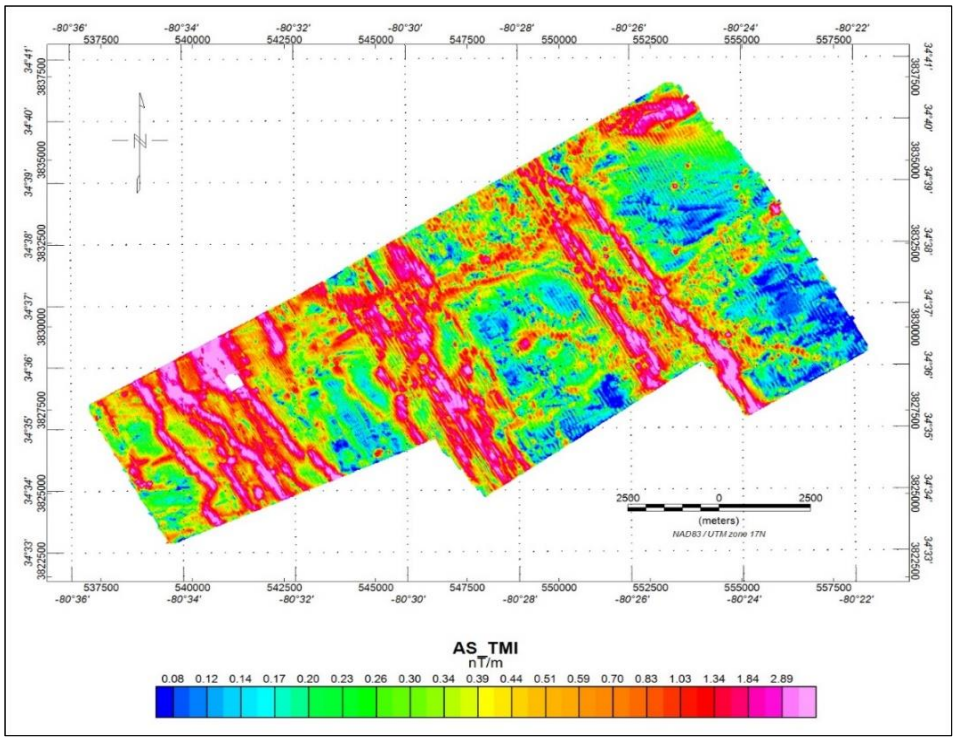

Figure 5.29: Analytic signal of total magnetic intensity map.

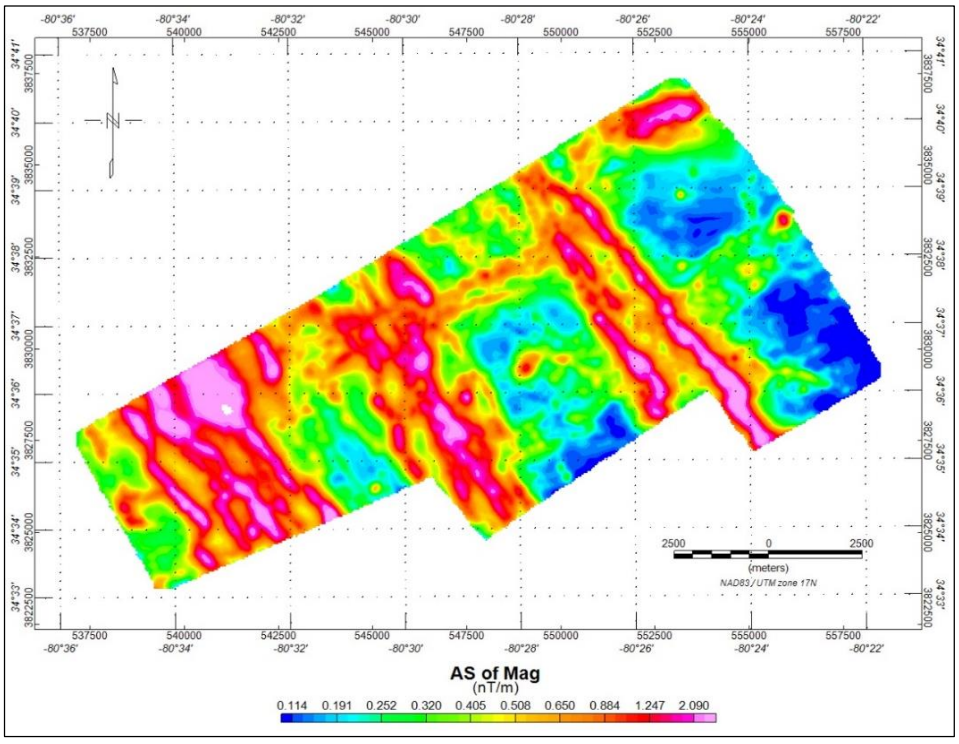

Figure 5.30: Upward continuation of 70 m applied to the AS of TMI map.

www.manaraa.com

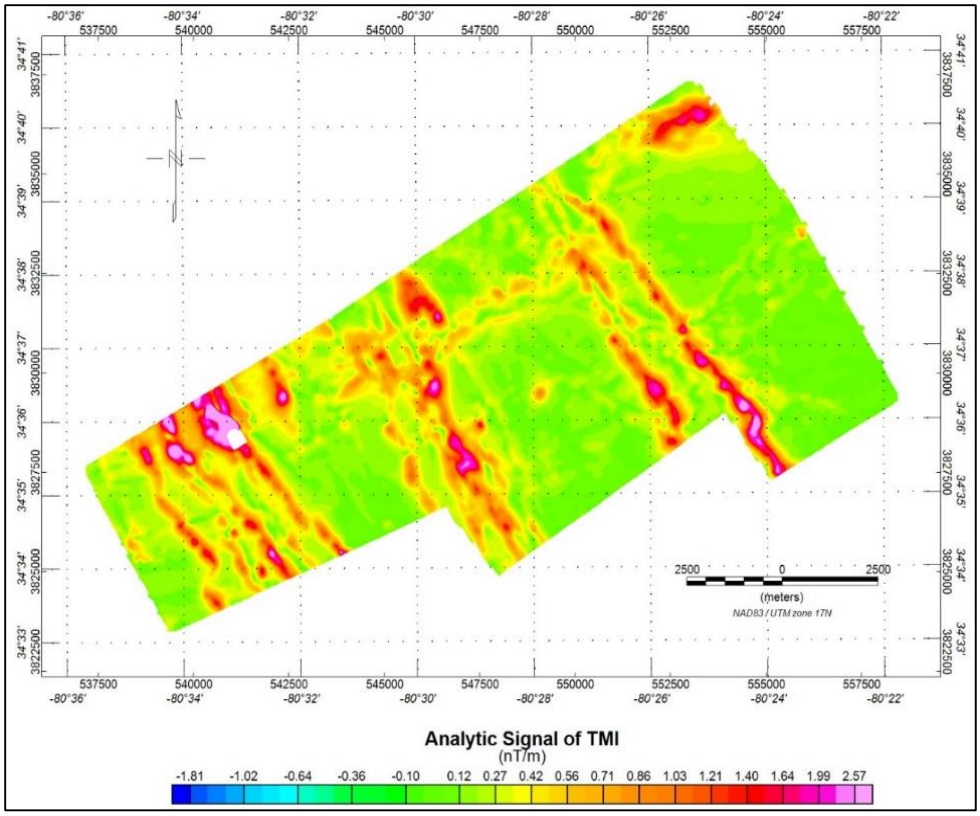

Figure 5.31: Upward continuation of 70 m applied on AS of TMI map. To improve the dynamic resolution, the color scale was changed to highlight the maximum anomalies.

Tilt Derivative (TDR method):

The tilt derivative was applied to the RTP map (figure 5.32) showing that the main subsurface structural trends in the study area are NE-SW and NW-SE, alkaline and diabase dikes, respectively. The felsic intrusive contact is also delineated.

The upward continued filter of 70 m was applied on the tilt derivative of the RTP map (figure 5.33) to filter out the effects of near-surface features and for a better demonstration of the contact locations. Figure 5.33 shows that the tilt derivative of RTP can be used for the location of the anomaly sources assuming a vertical contact model and the resolution of structural directions is better than figure 5.32.

www.manaraa.com

The geological map (mafic dikes, possible faults, and the felsic intrusion) have been superimposed over the upward continuation of 70 m of the tilt derivative of the reduced to pole map. In figure 5.34, it is clear the tilt derivative highlights the anomaly sources of the study area. The anomalies in the AS of TMI map have variable peak intensities while the TDR of the RTP map have constant peak intensities.

The upward continuation of 50m of the tilt derivative of the RTP map in figure 5.35 shows some structural trends that have not been identified in the geological map. These structures in the central and eastern part of the study area have NW and NNE trends. Some of these trends are also visible on the shaded relief map.

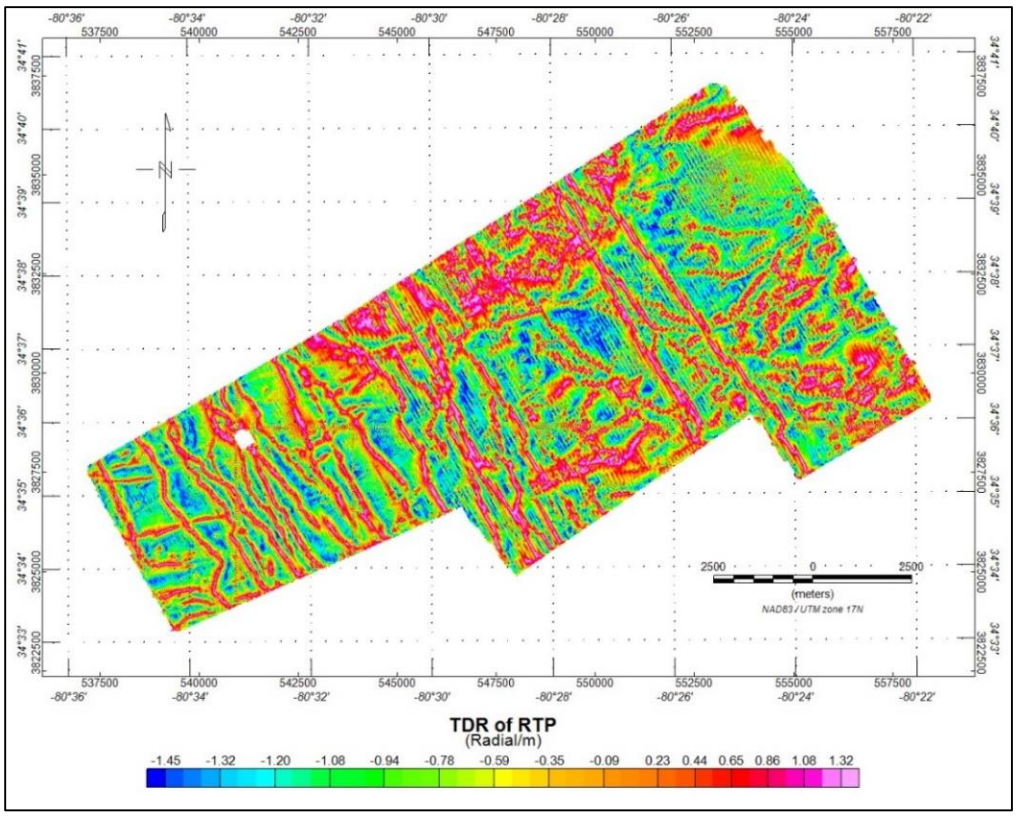

Figure 5.32: Tilt derivative of the reduced to the pole.

www.manaraa.com

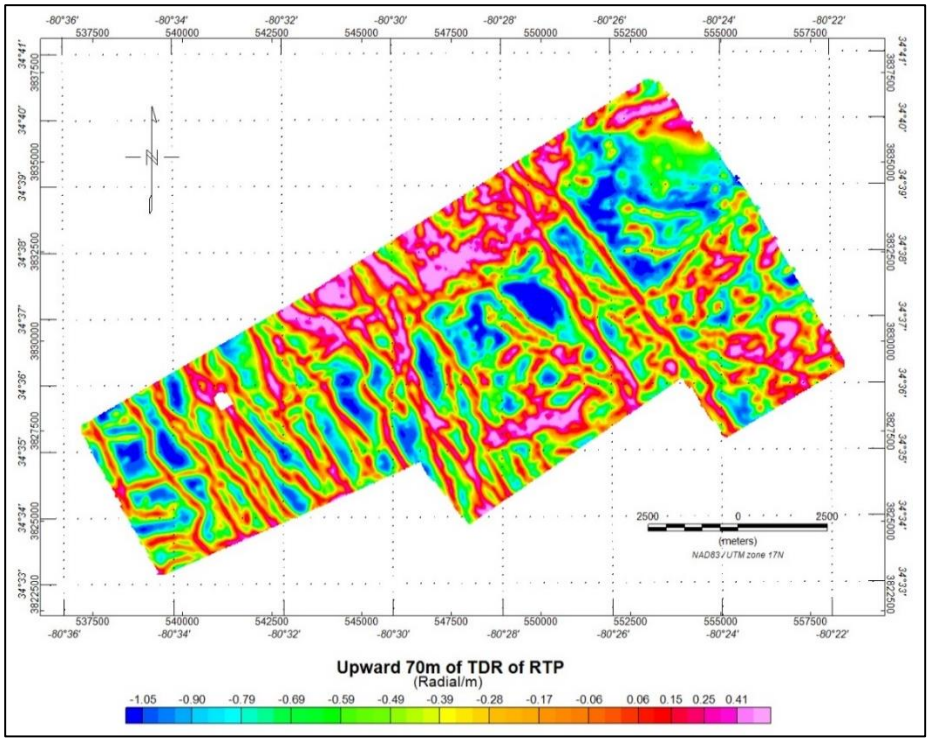

Figure 5.33: Upward continuation of 70 m of the TDR of the reduced to the pole map.

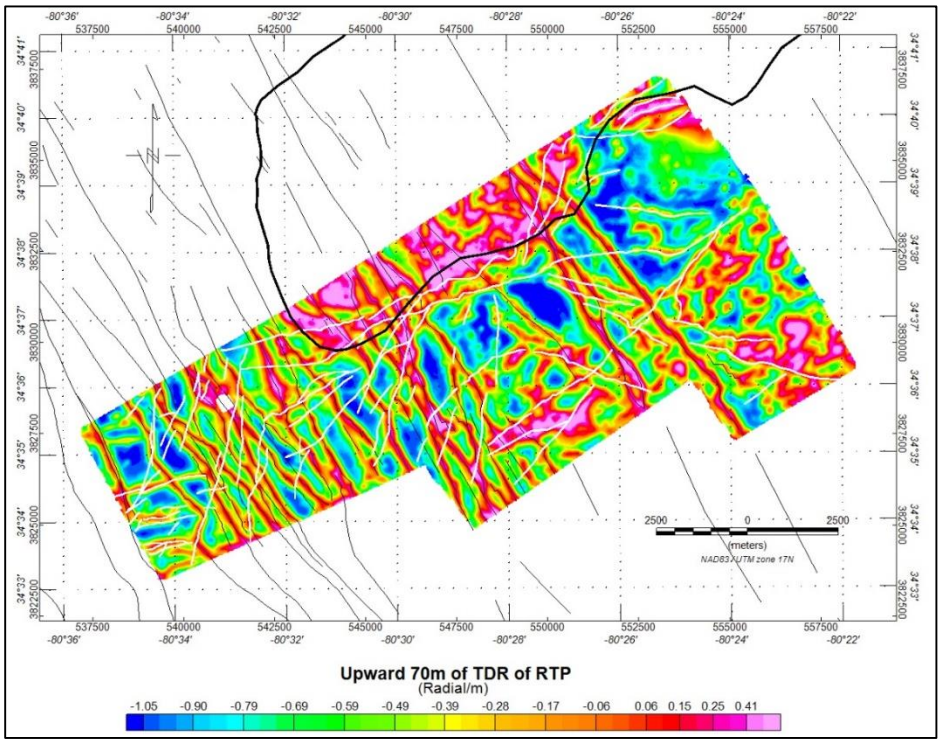

Figure 5.34: Geological map superimposed on the upward continuation of 70 m of the TDR of the RTP map. The white lines are possible faults. The thick line is the felsic intrusive. The NW-SE lines are mafic dikes.

www.manaraa.com

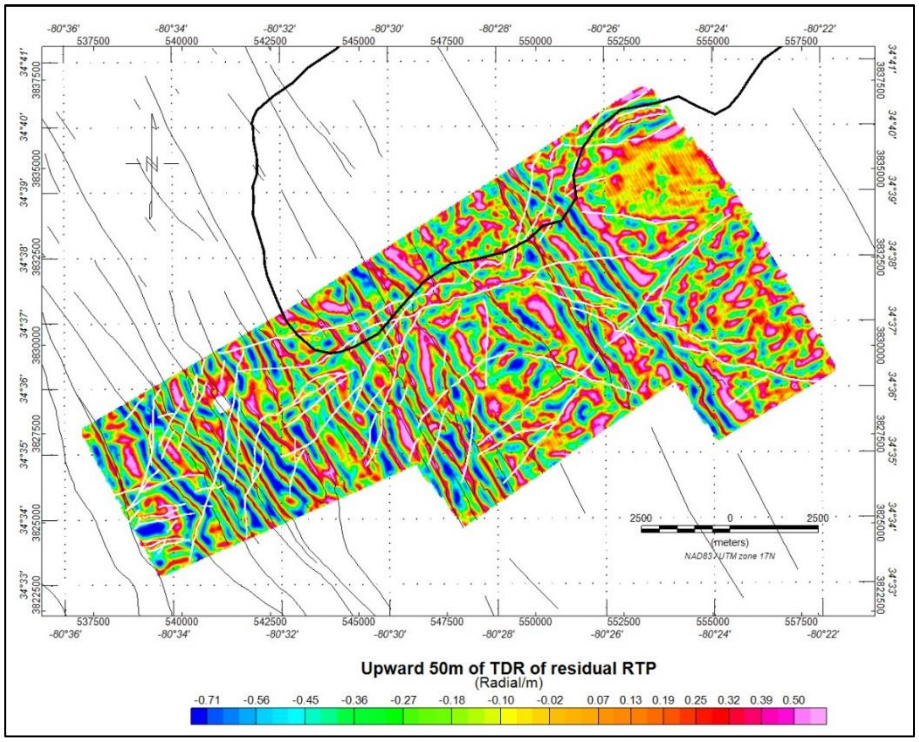

Figure 5.35: Geological map superimposed on the upward continuation of 30 m of the TDR of the residual RTP map. The white lines are possible faults. The thick line is the felsic intrusive. The NW-SE lines are the mafic dikes.

Source Parameter Image method (SPI):

The local wavenumber like the analytic signal is independent of source magnetization and dip effects; however, the source position, depth and horizontal location, can be determined directly from the magnetic field (Pilkington and Keating 2006).

The SPI can be applied on the total magnetic intensity map to estimate the depth of the magnetic sources. Figure 5.36 shows that the magnetic source depths ranging from 7 to 1188 m (figure B.2). The result is very close to the average depth of the power spectrum method. The SPI map shows the same structure as the tilt derivative of the RTP map. It shows an oval pattern in the northeast part of the study area around the Brewer

www.manaraa.com

Mine area that may be related to the Richtex/Persimmon Fork contact, the hydrothermal alteration zone or the metamorphic halo. Also, line 1-1' on the SPI map shows the same structural trend as the tilt derivative of the residual RTP map, this line has not been interpreted in the geological map. In figure 5.37 the geological map is superimposed on the source parameter image of the TMI map.

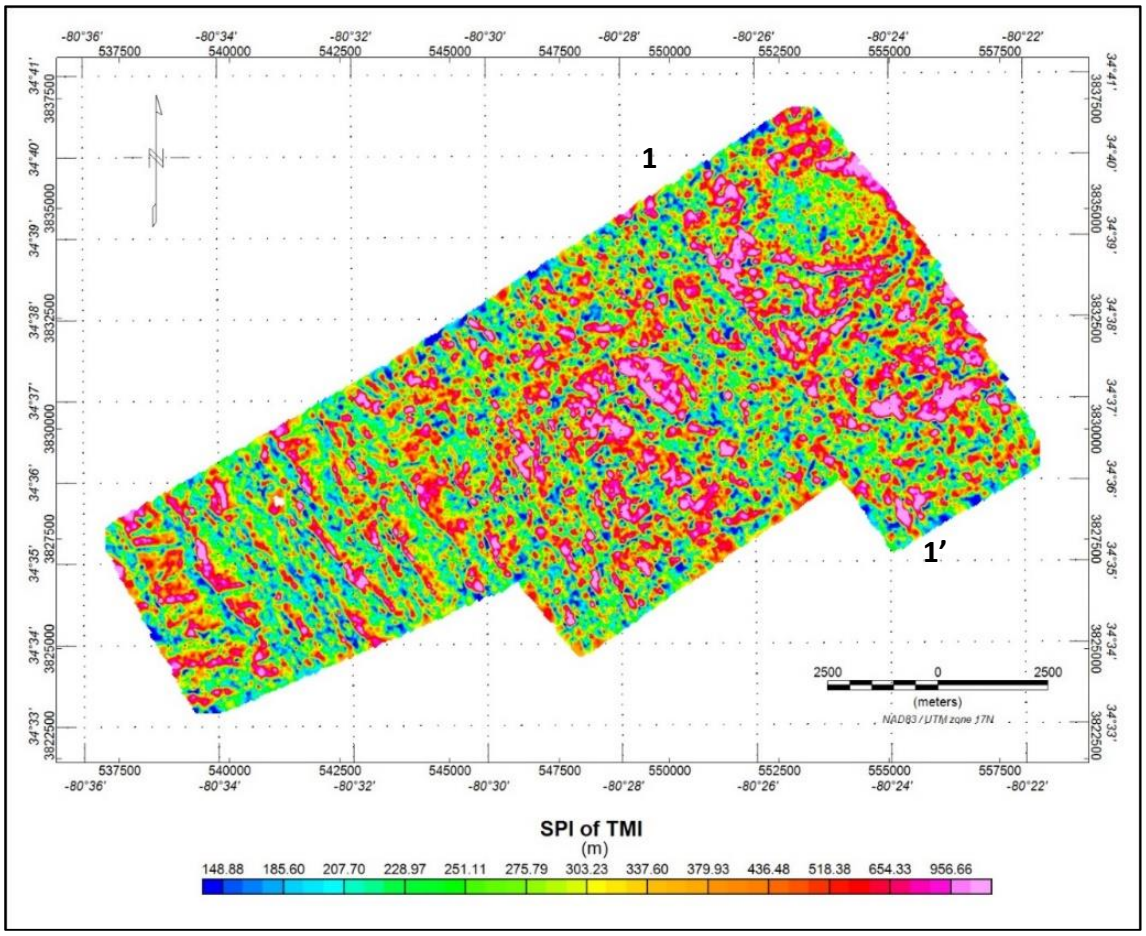

Figure 5.36: The SPI of TMI map. The sources depths range between 8 and 1188 m.

www.manaraa.com

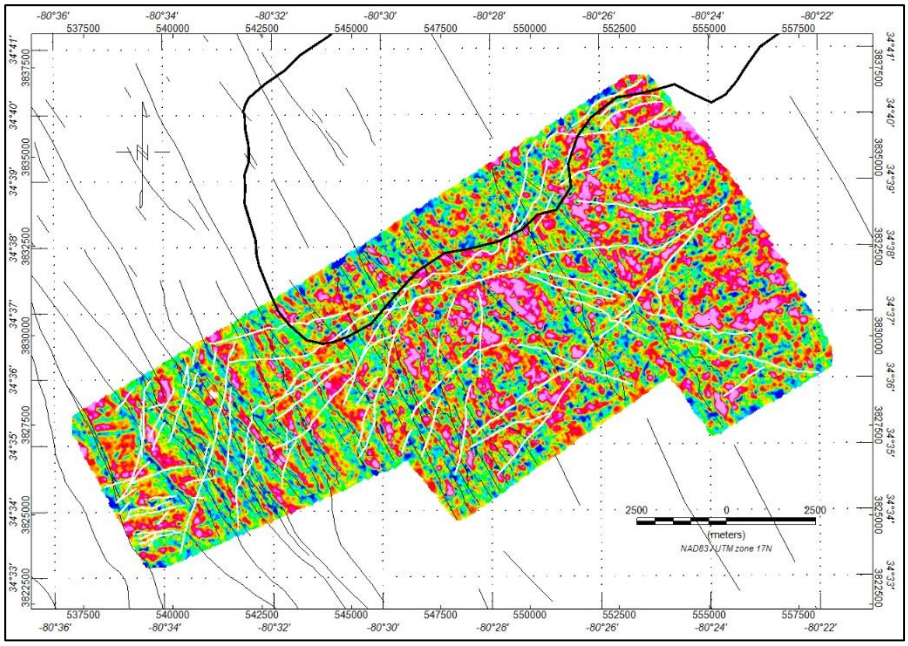

Figure 5.37: Geological map superimposed on the SPI of the TMI. The white lines are possible faults. The thick line is the felsic intrusive. The NW-SE lines are the mafic dikes.

3-D Euler deconvolution (ED):

The Euler deconvolution (ED) method was applied on the analytic signal (AS) and the total magnetic intensity (TMI). The positive depth values of the ED are below sea level and minus values are above sea level.

The ED of the upward continuation of the analytic signal of TMI map (figure 5.38) shows good agreement with the analytic signal map. The solution depths of the ED contacts range from -155.5 to 363.3 m. As indicated from the ED method the yellow contacts show depths between 0 to 100 m (below the sea level). Comparisons of the Euler Deconvolution (ED) method and the analytic signal solutions show reasonable agreement. Both methods are useful, where AS can be used to locate magnetic contacts, and their geometry, the ED can give a more information about the structural information

www.manaraa.com

and depths (Roest et al. 1992; Ndlovu et al. 2015). In figure 5.39 the ED of TMI is superimposed on the upward continuation of 70 m of the AS of TMI map. The yellow contacts show depths between 0 and 100 m (below sea level). The ED of TMI's solutions shows good agreement with analytic signal of TMI map solutions. Both figures indicate that the study area is affected mainly by two structural trends, NE and NW, and have similar contact depth results. Figure 5.40 shows the ED solutions plotted on the TMI map.

In figure 5.41 the depth calculated from the tilt derivative is compared with the Euler deconvolution of the TMI and the Euler deconvolution of the analytic signal's depth solutions (Table 5.3). The location of labels on the tilt derivative of the RTP map that were selected for depth estimation were compared with the closest points obtained from the Euler deconvolution and the Euler deconvolution of the upward continuation of 70 m of the analytic signal of the TMI maps. A, B and D tilt derivative and Euler deconvolution of the TMI depth results are similar. C shows that the depth of the tilt derivative of the RTP is very close to the depth of the Euler deconvolution of the analytic signal.

Table 5.3: Depth estimates based on the TDR, ED of TMI, and ED of AS.

Label	X	Y	TDR depth (m)	ED depth of the TMI (m)	ED of the AS of TMI depth (m)
A	544250	3828600	97.28	94.62	50.70
B	546250	3826950	98.8	80.17	78.43
C	546550	3829700	135.40	66.89	131.64
D	549250	3828050	154.44	140	80.93

www.manaraa.com

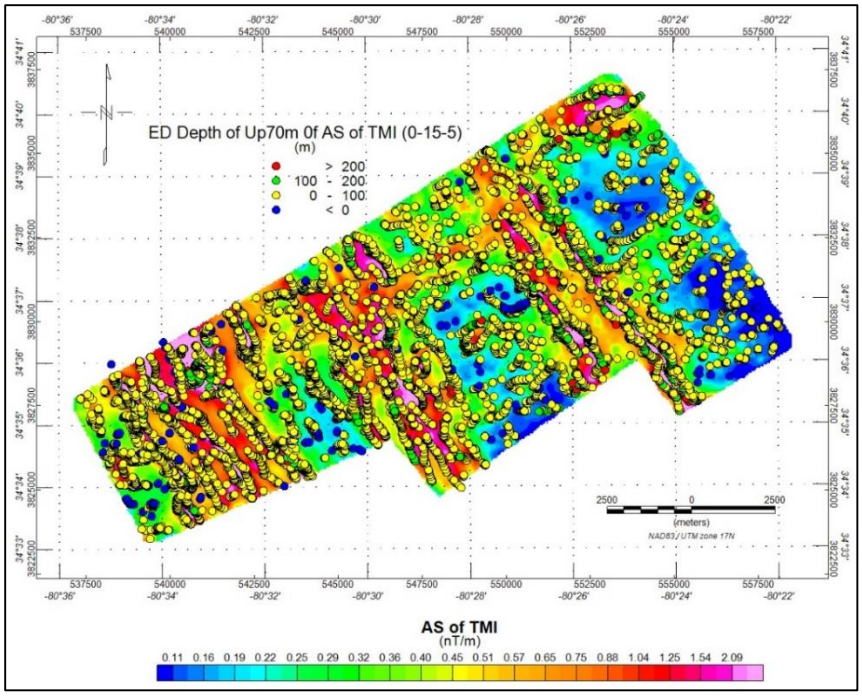

Figure 5.38: Euler deconvolution solutions of the upward continuation of 70 m of the AS of TMI. The solution depths range between - 155.5 and 363.3 m. The SI=0, Depth tole = 15%, Win. Size= 5, and flying height is 32m.

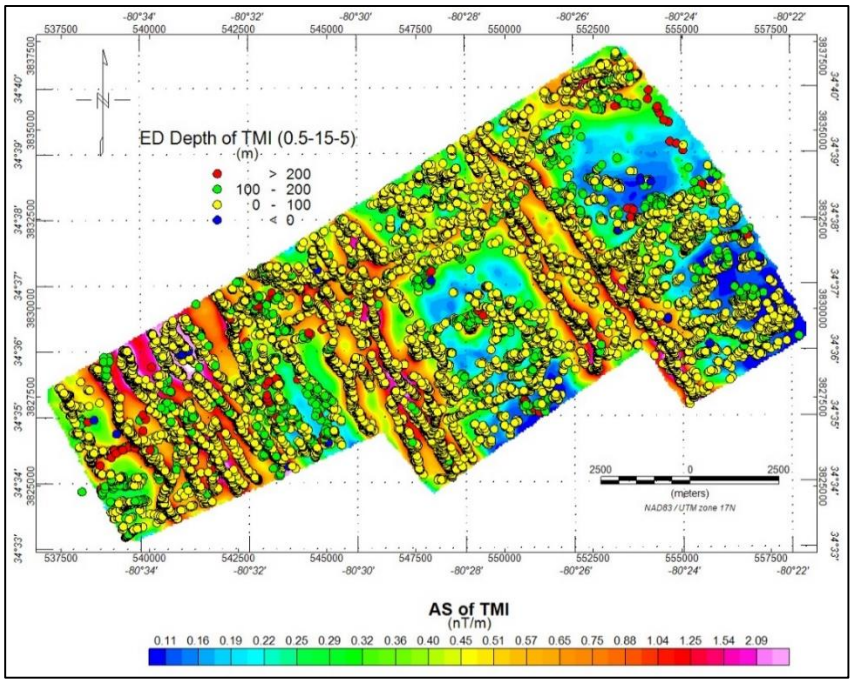

Figure 5.39: Euler deconvolution solutions of TMI plotted on the upward continuation of 70 m of the AS of TMI. The solution depths range between - 155.5 and 529 m. The SI=0, Depth tole = 15%, Win. Size= 5, and flying height is 32m.

www.manaraa.com

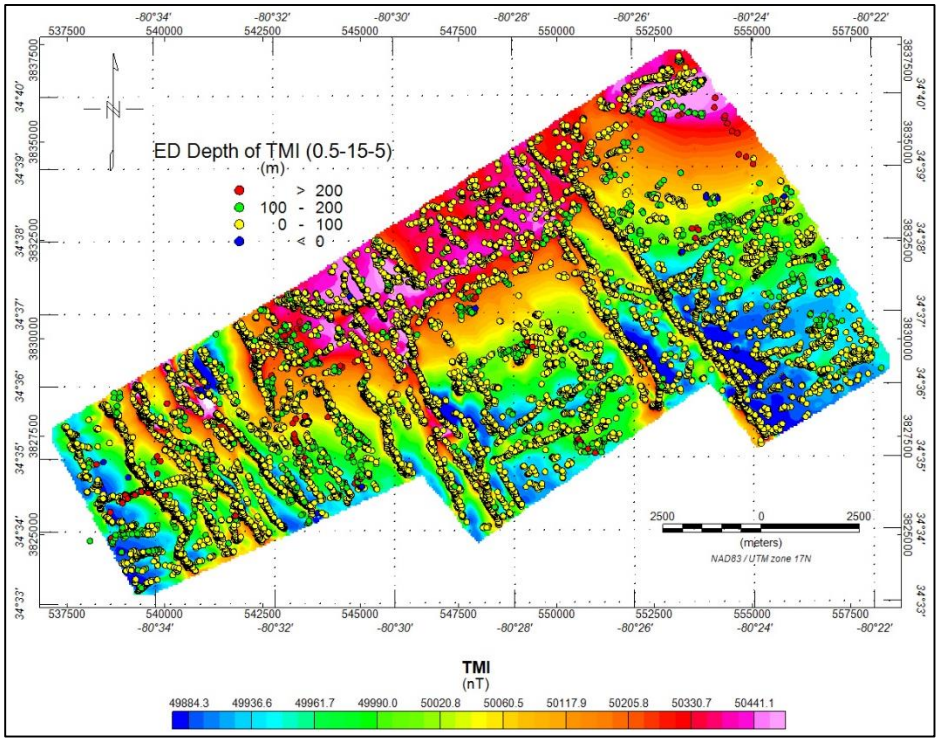

Figure 5.40: Euler deconvolution solutions of the TMI plots on the TMI map. The solution depths range between - 155.5 and 529 m. The SI=0, Depth tolerance = 15%, Win. Size= 5, and flying height is 32m.

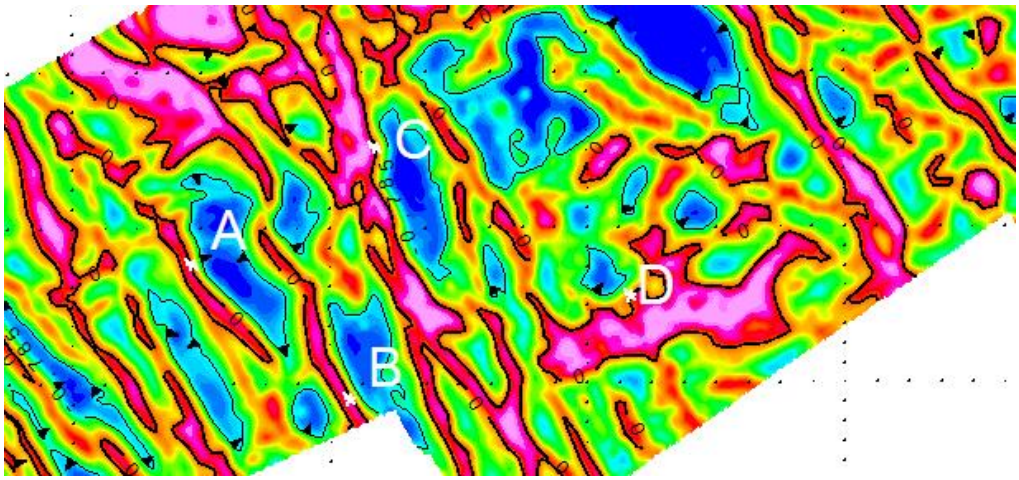

Figure 5.41: Expanded view of the tilt derivative of the RTP map. The thick black contour line indicates the edge of the contact and localizes the contact location. The thin black contour lines are equal to - 45° and can be used for calculating depths on edges. For the best interpretation of depth estimation by the tilt derivative method, points (A to D) are selected.

www.manaraa.com

5.3 Electromagnetic Data Results

The digital database of the electromagnetic anomalies was gridded using a bi-directional gridding algorithm with a grid cell of 10 m (figure 5.42). The conductivity grid as shown in figure 5.42 has some leveling problems (such as tie line leveling, lag corrections, base level corrections, etc.), so, a microlevelling filter using FFT Decorrugation is applied to remove non geological noise caused by long-wavelength noise along flight lines as recommended by Geosoft (Paterson Grant & Watson). The leveling error "noise" grid is calculated by applying two filters, the Butterworth high-pass filter combined with a directional cosine filter. The Butterworth high-pass filter is set to four times the line separation, while, the directional cosine filter is set to pass wavelengths only in the direction of the lines. The Butterworth passes wavelengths on the order of two to four line separations, such as would result from a line-to-line levelling error. Figure 5.43 shows the result of applied leveling correction to the conductivity grid after subtracting the levelling error grid from the original.

Figure 5.44 shows cultural noises (roads and power lines) that had been defined by OceanaGold during the EM survey. To reduce electromagnetic noises from the raw data, a high pass filter was applied. The high pass image represents cultural noise as shown in figure 5.45. The final result was produced by subtracting the original data from the high pass image (figure 5.46), so, the data quality result was significantly improved.

Figure 5.47 shows the lithologic boundary of the Ritchtex formation from the geological map superimposed on the conductivity map. High conductive anomalies are associated with the Ritchtex unit and the ore in the Haile Mine area. Also, a circular feature is clearly seen around the Brewer Mine area, which possibly indicates a contact.

www.manaraa.com

Figure 5.48 and 5.49 show the conductivity associated with the ore bodies both before and after filtering. Note the correlation between the zones of high conductivity and the mapped ore bodies. The EM profile B-B' is shown in figure 5.50. The profile indicates a high conductivity anomaly in the lower western part of the section that also correlates with the location of an ore body.

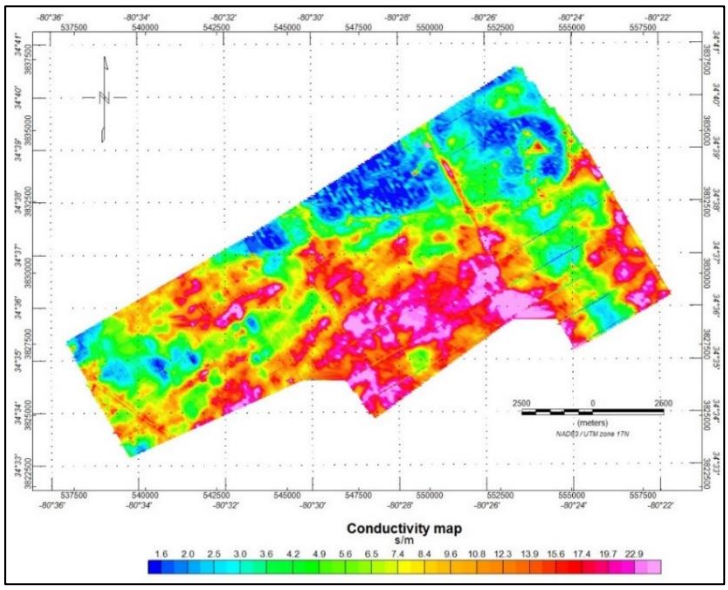

Figure 5.42: The conductivity map.

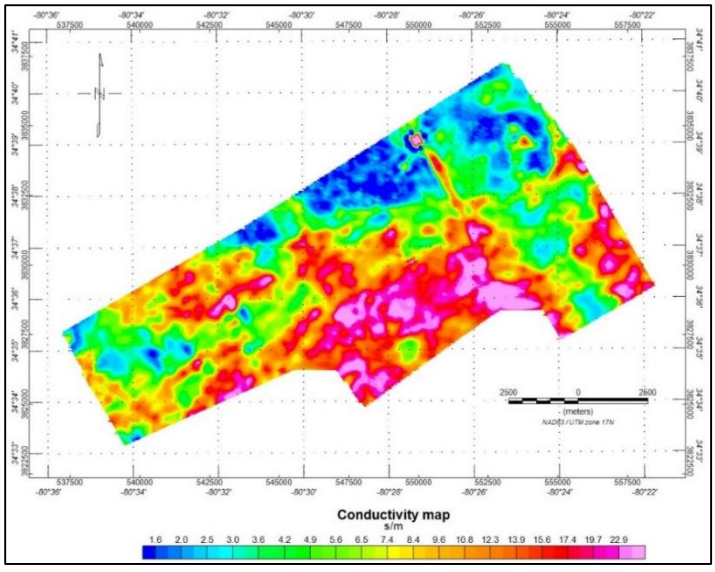

Figure 5.43: The leveling correction of the conductivity map.

www.manaraa.com

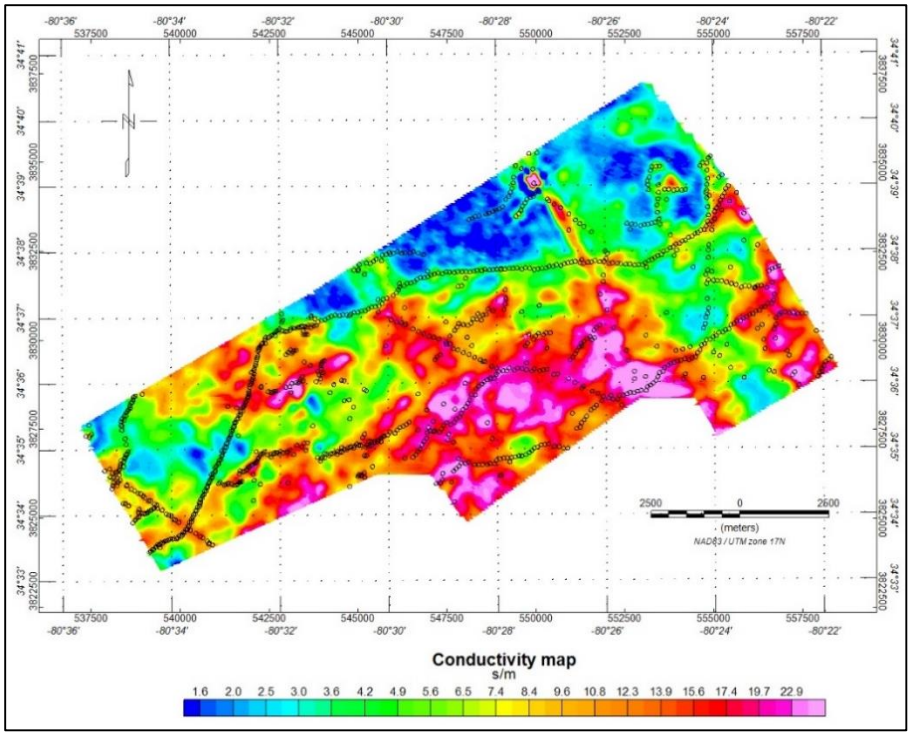

Figure 5.44: The cultural noise (dotted lines) plotted on the conductivity map.

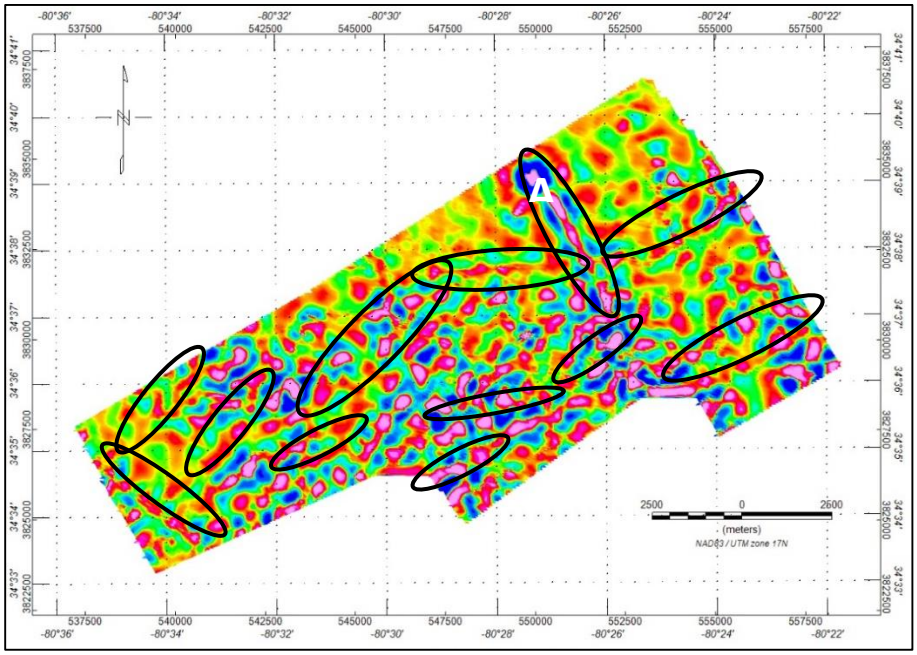

Figure 5.45: The EM data after using a high pass filter to represent the noise. Black ovals indicate the observer noises that were defined from the dataset. Label A indicates a high tension power line from Google earth.

www.manaraa.com

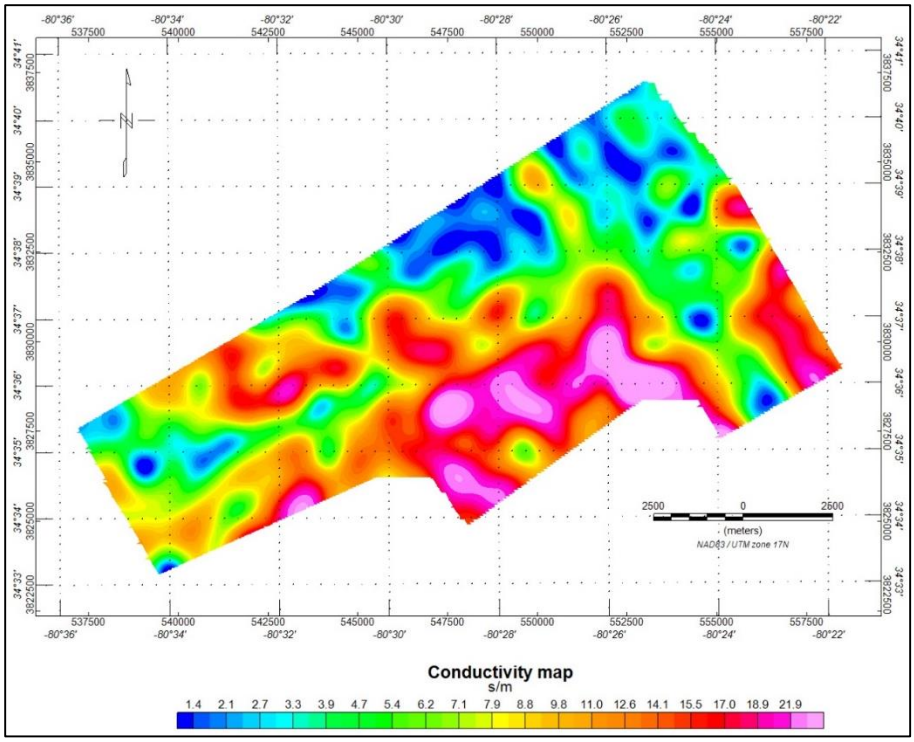

Figure 5.46: Conductivity map after reducing the noise.

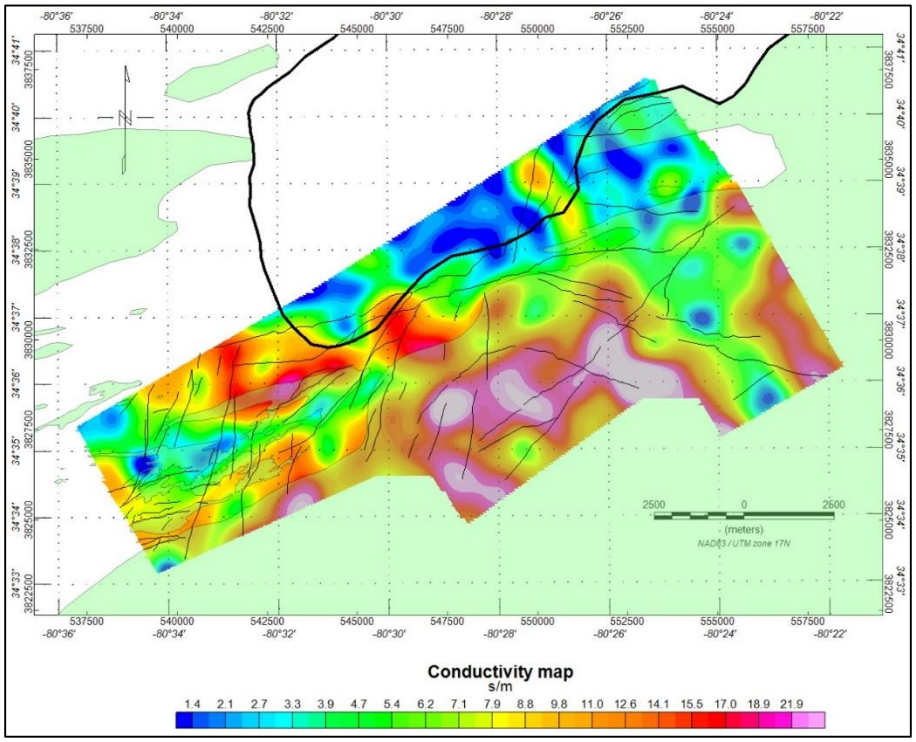

Figure 5.47: The lithologic boundary of the metasedimentary formation (green color) superimposed on the conductivity map. The thick black line indicates the felsic intrusion.

www.manaraa.com

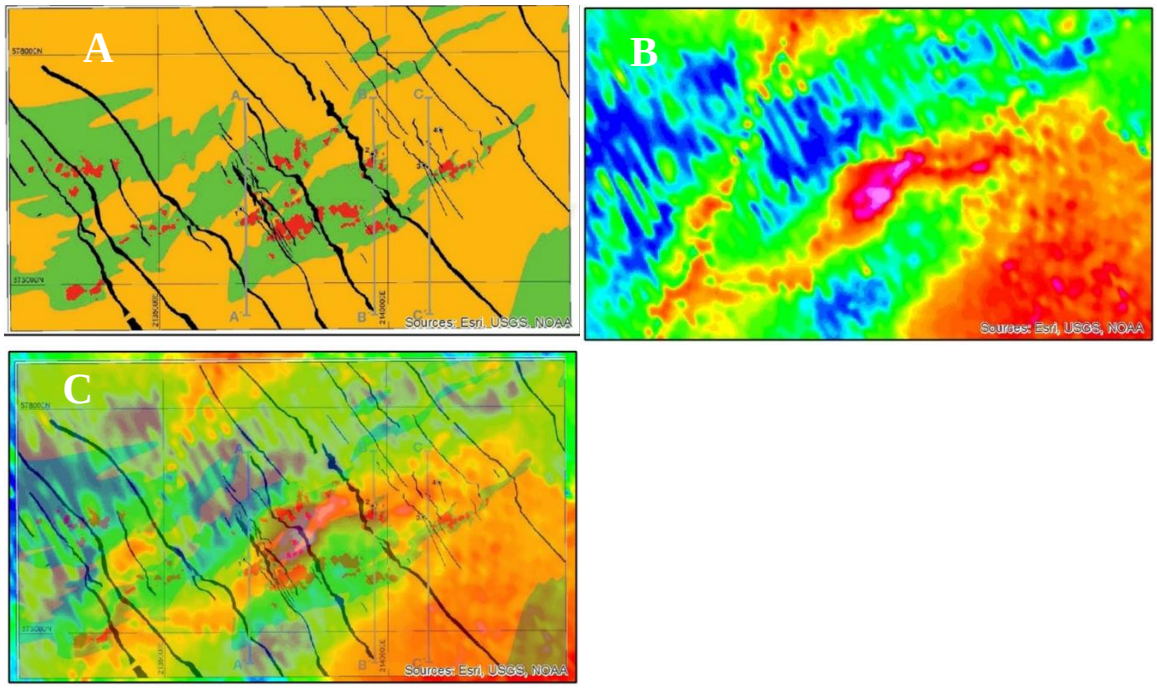

Figure 5.48: A is the geological map of Haile Mine at 120 m above sea level. B is the unfiltered EM conductivity map. C is the geological map superimposed on the conductivity map. Note the correlation between the zones of high conductivity and the mapped ore bodies.

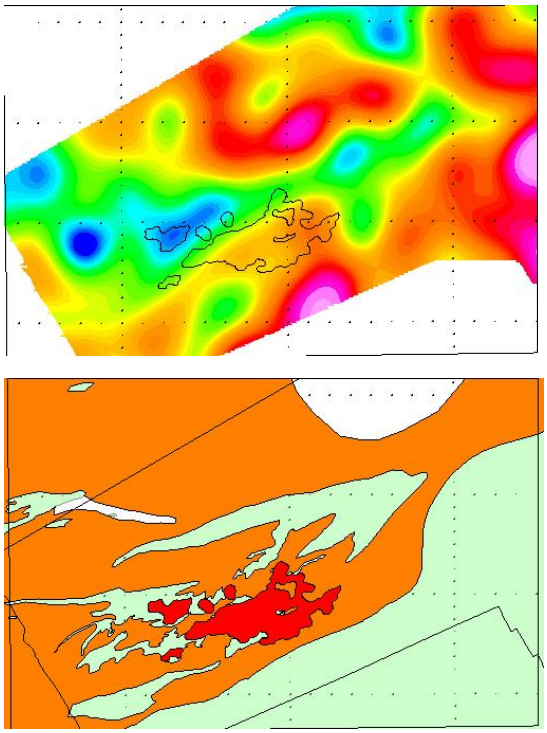

Figure 5.49: The EM conductivity after HP filter and the geological map. Note the high EM signal associated with the ore location and trend.

www.manaraa.com

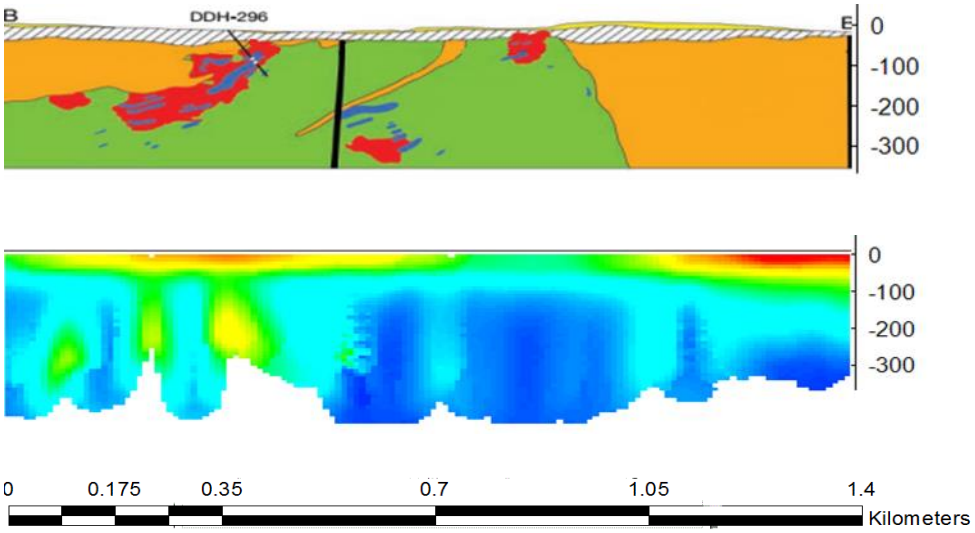

Figure 5.50: Cross section shows the conductivity over the B-B' profile. A conductive anomaly in the lower western part of the section is associated with an ore body. A low conductive anomaly is located just south of the dike. Left side is north.

www.manaraa.com

CHAPTER 6

DISCUSSION AND INTERPRETATION

The Bouguer map shows that the Pageland granite is characterized by low gravity anomalies in the northern section of the study area. High gravity anomalies to the west are related to the metavolcanic rocks and/or mafic dikes. The gravity anomalies over the Haile Mine area are related to the increase in the thickness of the metasedimentary section. Positive anomalies in the residual and analytic signal Bouguer gravity field correlate with the location of an ore body. The 2-D density forward model shows that the anomaly can be produced by 4% pyrite and molybdenite.

The total magnetic intensity (TMI) map is dominated by the NW-trending Jurassic dikes, while its tilt derivative and residual show both the Jurassic and Alleghanian dike trends. The analytic signal of TMI and shaded relief of RTP maps illuminate the edge contact of the Pageland granite. The magnetic survey shows no clear signal associated with the ore zones. This may be due to 1) the ore's magnetite being affected by hydrothermal alteration similar to New Zealand (Morrell et al. 2011); 2) the low susceptibility of quartz and pyrite (table 6.1) that is associated with the mineralization zones; and 3) the stronger magnetic signal from the mafic dikes that dominates the magnetic field. Over the metasedimentary formation the tilt derivative map has a negative value and the analytic signal has a low anomaly.

www.manaraa.com

A circular structural feature is observed by the Source parameter image and the Euler deconvolution magnetic and gravity maps around the Brewer mine and in the central part of the study area.

The cultural electromagnetic noise was reduced by applying a high pass filter. Ore bodies in the Haile mine area show high conductivity, while the intrusive felsic (Pageland granite) is associated with the lowest conductivity. A zone of high conductivity near the Brewer mine is surrounded by a circular zone of low conductivity.

Table 6.1: The susceptibilities of various rocks and minerals.

Material	**Susceptibility x 10^{-3} (SI)**	**Material**	**Susceptibility x 10^{-3} (SI)**
Quartz	-0.01	Illmenite	300 – 3500
Rock Salt	-0.01	Magnetite	1200 - 19,200
Calcite	-0.001 - 0.01	Limestones	0 – 3
Sphalerite	0.4	Sandstones	0 – 20
Pyrite	0.05 – 5	Shales	0.01 – 15
Rock Salt	-0.01	Illmenite	300 – 3500
Hematite	0.5 – 35	Magnetite	1200 - 19,200
Limestones	0 – 3	Shales	0.01 – 15
Sandstones	0 – 20	Schist	0.3 – 3
Gneiss	0.1 - 25	Granite	0 - 50
Slate	0 - 35	Gabbro	1 - 90
Basalt	0.2 - 175	Peridotite	90 - 200
from T.M. Boyd of the Colorado School of Mines			

The geological contacts map of the study area (figure 6.1) was drawing based on the ED (structural index= 0.5 and 1), tilt derivative, and analytic signal of TMI and shaded relief of RTP maps. The Ritchtex over the Haile Mine area, Au bearing alteration zones, and possible faults in figure 6.1 are the same as the geological map.

www.manaraa.com

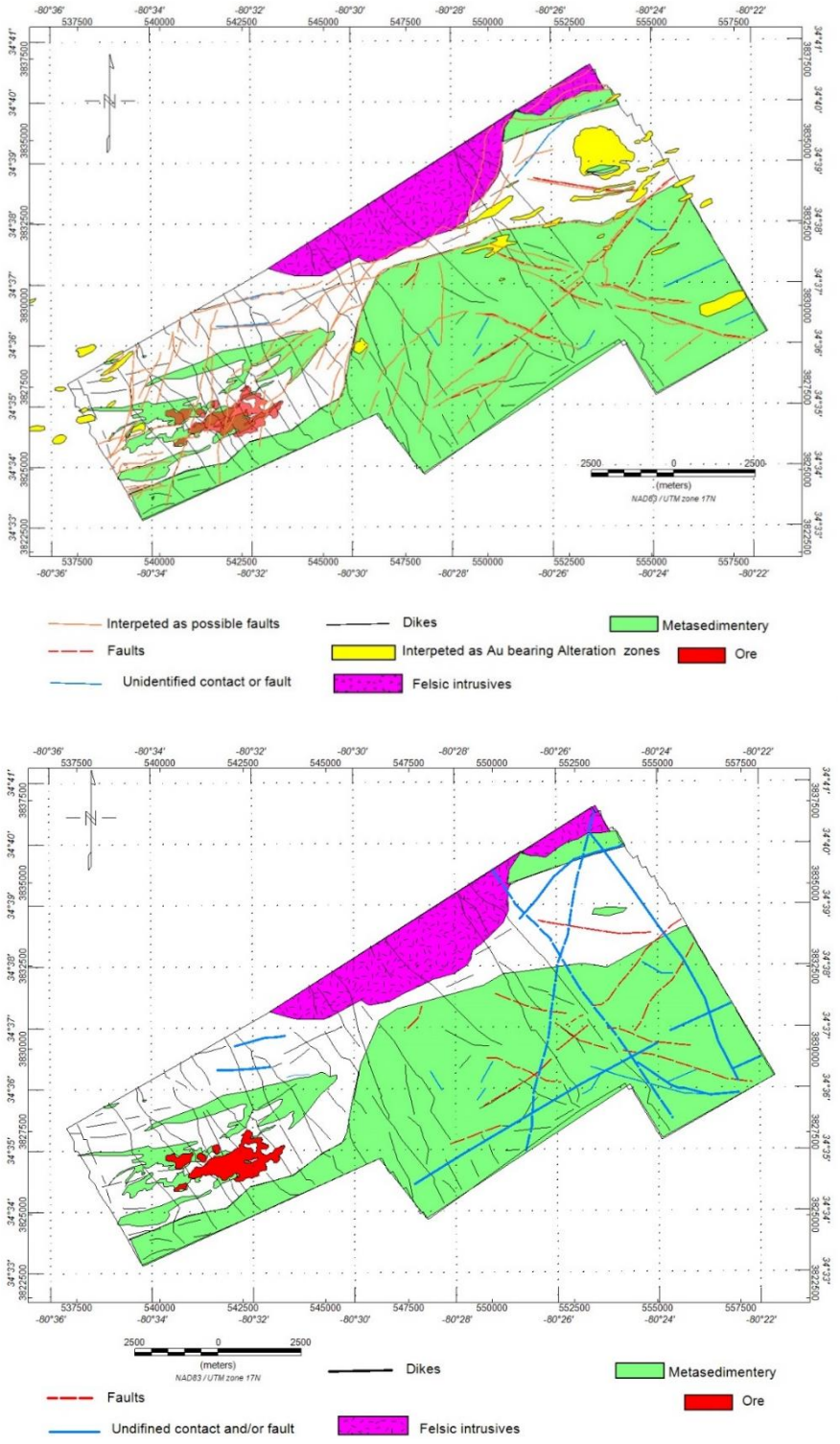

Figure 6.1: Geological map of the study area. (Upper map) Contacts and faults are based on the Euler deconvolution (structural index= 0.5 and 1), tilt derivative of the RTP, and analytic signal of the TMI and shaded relief of the RTP maps and the geological map by OceanaGold. (Lower map) The lower map is the geological map based primarily on the geophysical data.

www.manaraa.com

CHAPTER 7

CONCLUSIONS

The goal of this research was to calibrate and test geophysical methods for the detection of disseminated sulfides in the area of the Haile Gold Mine, South Carolina. The work focused on the use of high resolution gravity, electromagnetic (EM) and magnetic data. Surprisingly, an apparent correlation was observed between high resolution gravity anomalies and an ore body in the Haile Mine area. EM methods also show promise for exploration for disseminated sulfides. While magnetic data was not apparently useful for direct detection of ore bodies in the Haile Mine area, it was very useful in defining the geometries of intrusive igneous plutons and dikes as well as an apparent zone of hydrothermal alteration around the Brewer Mine. Specific conclusions include:

1. The interpretation of the gravity and magnetic data was enhanced by the use of tilt derivatives, reduced to pole anomalies (RTP), shaded relief, Power spectrum, Analytical signal, Source parameter imaging (SPI), 3-D Euler deconvolution, upward continuation, and 2-D forward density modeling.
2. There is a strong regional correlation between high amplitude gravity and magnetic anomalies and the most productive gold mines in the Carolina terrane.

www.manaraa.com

3. Residual gravity anomalies, tilt derivatives, and analytic signal show positive anomalies correlated with the location of a disseminated ore body in the Haile Mine area. The observed gravity field over the ore body matched model predictions produced by 4% pyrite and molybdenite.
4. Helicopter EM methods are effective in distinguishing sedimentary from volcanic-dominated sediments in the metamorphic rocks of the Carolina terrane.
5. Electro magnetic (EM) anomalies are also spatially associated with the Haile ore bodies. Cultural signals in the EM data can be minimized with high pass filtering.
6. The edges of the Pageland granite pluton are clearly illuminated by the shaded relief, tilt derivative, Euler deconvolution, and analytic signal of the high resolution magnetic field.
7. The RTP magnetic field is dominated by NW-trending Jurassic mafic dikes as well as ENE-trending Alleghanian age alkaline dikes.
8. An oval pattern in the magnetic SPI outlines the Brewer gold mine area, a zone of possible hydrothermal alteration.

www.manaraa.com

REFERENCES

Aeroquest, Jun.2010, Report on a Helicopter-Borne AeroTEM System Electromagnetic and Magnetic Survey for Haile Gold Mine Inc. Aeroquest Job # 10-021

Allard, M., 2007, On the Origin of the HTEM Species, in Milkereit, B., Ed., Proceedings of Exploration 07: Fifth Decennial International Conference on Mineral Exploration, p. 355-374.

Al-Fouzan, F., Harber, W., Dilmore, R., Hammach, R., Sams, J., et al., 2004, Methods for Removing Signal Noise from Helicopter Electromagnetic Survey Data. Mine Water and the Environment

Anschütz H., 2014, AEM Method Description and Project Examples, Report.

Ayuso R., Wooden J., Foley N., Robert R. Seal II, A. K. Sinha, 2005, U-Pb Zircon Ages and Pb Isotope Geochemistry of Gold Deposits in the Carolina Slate Belt of South Carolina

Balch, S., Boyko, T., and Paterson, N., 2003, the AeroTEM airborne electromagnetic system. The Leading Edge, 22:562-566.

Baranov, V., 1957, A new method for interpretation of aeromagnetic maps; pseudo gravimetric anomalies. Geophysics, 22(2), 359–382. https://doi.org/10.1190/1.1438369

Bell, H., Butler, J., Howell, D., and Wheeler, W., 1974, Geology of the Piedmont and Coastal plain near Pageland, South Carolina and Wadesboro, North Carolina. Carolina Geol. Soc. Field trip guide.

Berry, J., Mobley, R., Gillon, K., Yogodzinski, G., and Bates, C., 2016, A Neoproterozoic epithermal gold deposit _The Haile gold mine, South Carolina, USA: The Geological Society of America, Field Guide 42, p.1-8; 2016.

Bhattacharyya, B. K., 1965, Two-dimensional harmonic analysis as a tool for magnetic interpretation. Geophysics, 30(5), 829–857.

Blakely, R.J., 1995, Potential Theory in Gravity and Magnetic Applications, Cambridge University Press, New York.

Blakely, R. J., and Simpson, R. W., 1986, Approximating edges of source bodies from magnetic or gravity anomalies. Geophysics, 51, 1494–1498

Chiappini, A., Meloni, A., Boschi, E., Faggioni, O., Beverini, N., Carmisciano, C., and Marson, I., 2000, Shaded relief magnetic anomaly map of Italy and surrounding marine areas. Annali Di Geofisica 43, 5.

www.manaraa.com

Chile, S., (n.d), Consulting Potential Field Geophysics, Airborne Electro-Magnetic Surveys Workshop. Retrieved February 22, 2017, from http://www.geoexplo.com/airborne_survey_workshop_EM.html#Typical_Electrial_Pr

Cristopher R. Vyhnal, Harry Y. McSween, 1990, Constrain on Alleghanian vertical displacements in the southern Appalachian Piedmont, based on aluminum-in hornblende barometry: Geology; v.18, p.938-941; October 1990.

Cumbest, R. J., Price, Van, Anderson, Eric E., 1992, Gravity and Magnetic Modeling of the Dunbarton Triassic Basin, South Carolina: Southeastern Geology, v. 33, p. 37 51.

Daniels, D. L., 1974, Geological interpretation of geophysical maps, central Savannah River area, South Carolina and Georgia: U.S. Geological Survey Geophysical Investigations Map 68-893.

Daniels, D.L., 2005, South Carolina Aeromagnetic and Gravity Maps and Data: Open File Report 2005-1022. http://pubs.usgs.gov/of/2005/1022/

Dennis, A., and Wright, J., 1997, The Carolina terrane in northwestern South Carolina, U.S.A.: Late Precambrian-Cambrian deformation and metamorphism in a peri Gondwanan oceanic arc. Tectonics, 16:460-473.

Dentith M., Mudge S., 2014, Geophysics for the Mineral Exploration Geoscientist, Cambridge University Press, Chapter 5

Dobrin, M.B., 1960, Introduction to Geophysical Prospecting (2nd ed.), NewYork, McGraw-Hill

Dobrin, M.B., and Savit, C.H., 1988, Introduction to Geophysical Prospecting (4th ed.), New York, McGraw-Hill

Feebrey, C. A., Hishida, H., Yoshioka, K., and Nakayama, K., 1998, Geophysical Expression of Low Sulphidation Epithermal Au-Ag Deposits and Exploration Implications –Examples from the Hokusatsu Region of SW Kyushu, Japan–. Resource Geology, 48(2), 75–86. https://doi.org/10.1111/j.1751 3928.1998.tb00008.x

Feiss, Geoffrey P., 1982, Geochemistry and Tectonic Setting of the Volcanics of the Carolina Slate Belt: Economic Geology, v. 77, p. 273-293.

Foley N. and Ayuso R., 2012, Gold Deposits of the Carolina Slate Belt, Southeastern United States: Age and Origin of the Major Gold Producers. Open File Report 2012–1179

Ford, K., Keating, P., and Thomas, M. D., 2007, Overview of geophysical signatures associated with Canadian ore deposits. Geological Association of Canada, Mineral Deposits Division, Special Publication no. 5, p. 939-970.

Geosoft Inc., Creating Section(s) from Array Data, How-To Guide; 10/08/2015.

[1]Geosoft Oasis montaj, n. d., Introduction GM-SYS. Retrieved March 3, 2017, from https://my.geosoft.com/elearning/lessons/#/reading/542

www.manaraa.com

[2]Geosoft Oasis montaj, 16/01/2013, Applying filters with montaj Geophysics, How-To Guide. Retrieved from http://updates.geosoft.com/downloads/files/how-to guides/Applying_Filters_with_montaj_Geophysics.pdf

[3]Geosoft technical note, n.d., Reduction to the Magnetic Pole for High Frequency High Amplitude Anomalies. Retrieved March 3, 2017, from http://www.geosoft.com/search results/?q=reduced+to+pole#sthash.TCARMvyN.dpuf

Grant, F. S., and Dodds, J., 1972, MAGMAP FFT processing system development notes, Paterson Grant and Watson Limited. 1972; 230.

Hatcher, R. D., Jr., 2005, Southern and Central Appalachians, Elsevier Ltd; 2005.

Hatcher, R. D., Jr., Bream, B.R, and Merschat, A. J., 2007, Tectonic map of the southern Appalachians: A tale of three orogens and a complete Wilson Cycle, in Hatcher, R.D., Jr., Carlson, M.P., McBride, J.H., and Martinez Catalan. J.R., eds., 4-D Framework of Continental Crust: Geological Society of Ameraica Memoir 200, p. 595-632.

Hibbard, J., 2000, Docking Carolina: Mid-Paleozoic accretion in the southern Appalachians: Geology; February 2000; v. 28, p. 127-130.

Hibbard, J., Stoddard, E., and Secor, D., Dennis, J., 2002, The Carolina Zone: overview of Neoproterozoic to Early Paleozoic peri-Gondwanan terranes along the eastern Flank of the southern Appalachians: Earth-Science Reviews, v. 57, p. 299-339

Hildenbrand, T., 1983, A filtering program based on two-dimensional Fourier analysis of geophysical data. United States Department of The Interior Geological Survey, open file report 83-237.

Hildenbrand, T., and Kucks, R., 1988, Filtered Magnetic Anomaly Maps of Nevada Sheet 5 - Shaded Magnetic Relief Maps - NGDS. Retrieved March 3, 2017, from http://data.geothermaldata.org/dataset/filtered-magnetic-anomaly-maps-of nevada-sheet-5-shaded-magnetic-relief-maps

Hinze, W. J., 1960, Application of the gravity method to iron ore exploration. Economic Geology, 55(3), 465–484. https://doi.org/10.2113/gsecongeo.55.3.465

Hinze, William J., von Frese, Ralph, R. B., and Saad, Afif, H., 2013 Gravity and Magnetic Exploration, Principles, Practices, and Applications, Cambridge University Press.

Hoover, D., Klein, D., and Campbell, D, 1995, Geophysical Methods in Exploration and Mineral Environmental Investigations. U.S. Geological Survey Open-File Report 95-831, p. 19-27.

Hoover, D, Reran, D., and Hill, P., 1992, the Geophysical Expression of Selected Mineral Deposit Models. U.S. Deparment of the Interior Geol. Surv. Open-File Report 92

Horn B.K.P. 1982. Hill shading and the reflectance map. Geoprocessing 2, 65–146.

www.manaraa.com

Hsu, S.-K., Coppens, D., and Shyu, C.-T., 1998, Depth to magnetic source using the generalized analytical signal. Geophysics, 63(6), 1947–1957. https://doi.org/10.1190/1.1444488

Hulse D., Lane T., and Crowl W., 2008, NI 43-101 Technical Report on the Haile Mine Project, Lancaster County, South Carolina.

Irvine, R. J., and Smith, M. J., 1990, Geophysical exploration for epithermal gold deposits. Journal of Geochemical Exploration, 36(1), 375–412. https://doi.org/10.1016/0375 6742(90)90061-E

Keary P., Brooks M., Hill I., 2002, An Introduction to Geophysical Exploration 3rd edition: Blackwell Science Ltd.

Klein T., Cunningham C., Robert R. Seal II, 2007, the Russell Gold Deposit, Carolina Slate Belt, North Carolina.

Lane, R.., 2002, Ground and Airborne Electromagnetic Methods, in Papp, E., Ed., Geophysical and Remote Sensing Methods for Regolith Exploration, CRCLEME Open file report 144, p. 53- 79.

Lillie, R., 1999, Whole Earth Geophysics: An Introductory Textbook for Geologists and Geophysicists (1st ed.), Prentice Hall, New Jersey.

Macleod, I., Jones, K., Dai, T., 1993. 3D analytic signals in the interpretation of total magnetic field data at low magnitude latitudes. Exploration Geophysics, 24(4), 679–688.

MacLeod IN, Jones K, Dal TF. 3-D analytic signal in the interpretation of total magnetic field data at low magnetic latitudes. Exploration Geophysics. 1993; 24:679–688.

Mariita, N. O., 2007, The Magnetic Method

Miller, H. G., and Singh, V., 1994, Potential field tilt – a new concept for location of potential field sources: Journal of Applied Geophysics, 32, 213–217

Mobley R., Yogodzinski G., Creaser R., and Berry J., 2014, Geologic History and Timing of Mineralization at the Haile Gold Mine, South Carolina; Economic Geology, v.109, pp.1863–1881; 2014.

Morrell, A. E., Locke, C. A., Cassidy, J., and Mauk, J. L., 2011, Geophysical Characteristics of Adularia-Sericite Epithermal Gold-Silver Deposits in the Waihi-Waitekauri Region, New Zealand, Economic Geology, 106(6), 1031–1041.

Nabighian M. N., 1972, the analytic signal of two-dimensional magnetic bodies with polygonal cross section: Its properties and use for automatic anomaly interpretation. Geophysics, 37:507–517

Nabighian M.N., Ander M.E., Grauch V.J.S., Hansen R.O. et al., 2005, Historical development of the gravity method in exploration. Geophysics 70, 6, 63ND 89ND. CrossRef

Ndlovu, T., Mashingaidze, R. T., and Mpofu, P., 2015. Analytic Signal and Euler Depth Interpretation of Magnetic Anomalies: Applicability to the Beatrice Greenstone Belt. Journal of Geography and Geology, v70, no 4.

www.manaraa.com

Nora, K., and Ayuso, R., 2012, Gold Deposits of the Carolina Slate Belt, Southeastern United States: Age and Origin of the Major Gold Producers. USGS, open-file report 2012–1179.

Paterson Grant & Watson, n.d, Geosoft Technical Note on Microlevelling using FFT Decorrugation, Retrieved February 22, 2017, from http://www.geosoft.com/media/uploads/resources/technical notes/microleveling%20tech%20note.pdf

Phillips, J.D., 2007. Geosoft eXecutables (GX's) developed by the U.S. Geological Survey, Version 2.0, with notes on GX development from Fortran Code. U.S. Geological Survey, Open file, Report: 1335.

Pilkington, M., and Keating, P., 2006, The relationship between local wavenumber and analytic signal in magnetic interpretation. Geophysics, 71(1), L1–L3. https://doi.org/10.1190/1.2163911

Popenoe, P. and Zietz, I., 1977. The Nature of the Geophysical Basement Beneath the CoastalPlain of South Carolina and Northeastern Georgia.

Qian, W. and Boerner, D., 1995, Electromagnetic modelling of buried line conductors using an integral equation. Geophysical Journal International, v121, p202-214

Rama Rao, C., Kishore, R. K., Pradeep Kumar, V., and Butchi Babu, B., 2011, Delineation of intra crustal horizon in Eastern Dharwar Craton – An aeromagnetic evidence. Journal of Asian Earth Sciences, 40(2), 534–541. https://doi.org/10.1016/j.jseaes.2010.10.006

Rapprecht, R., 2010, A study of Late-Proterozoic host rocks, the style of mineralization and alteration, and their timing at the Deep River gold prospect, central North Carolina. Master's Thesis, University of North Carolina at Chapel Hill.

Reeves, C., 2005, E-Book on Aeromagnetic Surveys: Principles, Practice and Interpretation. Retrieved March 2, 2017, from http://www.geosoft.com/news/news-releases/e-bookaeromagnetic-surveys principles-practice-and-interpretati

Reddi, A. G. B., Mathew, M. P., Singh, B., and Naidu, P. S., 1988, Aeromagnetic Evidence of Crustal Structure in the Granulite Terrane of Tamil Nadu-Kerala. Geological Society of India, 32(5), 368–381.

Reid, A.B., Allsop, J.M., Granser, H., Millett, A.J. and Somerton, I.W., 1990, Magnetic interpretation in three dimensions using Euler deconvolution. Geophysics, 55: 80 - 91.

Roest, W.R., Verhoef, J., and Pilkington, M., 1992. Magnetic Interpretation using the 3-D analytic signal. Geophysics, 57 116–125.

Roset, W. R., Verhoef, J., Pilkington, M., 1992, Magnetic interpretation using the 3D analytic signal. Geophysics 57:116–125

Saibi, H., Nishijima, J., Aboud, E., and Ehara, S., 2006, Euler deconvolution of gravity data in Geothermal Reconnaissance; the Obama geothermal area, Japan.

www.manaraa.com

Salem, A., 2004, Interpretation of magnetic data using analytic signal derivatives. Geophysical Prospecting, 53(1), 75–82.

Salem, A., and Ravat, D., 2003, A combined analytic signal and Euler method (AN EUL) for automatic interpretation of magnetic data. Geophysics, 68(6), 1952–1961. https://doi.org/10.1190/1.1635049

Salem, A., and Smith, R., 2005, Depth and structural index from the normalized local wavenumber of 2D magnetic anomalies. Geophysical Prospecting, 51, 83–89.

Salem, A., Williams, S., Samson, E., Fairhead, D., Ravat, D., and Blakely, R. J., 2010, Sedimentary basins reconnaissance using the magnetic Tilt-Depth method. Exploration Geophysics, 41(3), 198–209. https://doi.org/10.1071/EG10007

Salem, A., Williams, S., Fairhead, D., Ravat, D., and Smith, R., 2007, Tilt-Depth method: A simple depth estimation method using first-order magnetic derivatives. The Leading Edge, 26, 1502–1505

Salem A., Williams S., Fairhead J.D., Smith R. and Ravat D.J., 2008. Interpretation of magnetic data using tilt-angle derivatives, Geophysics, 73, P. L1- L10

Secor, Donald T., Sara, Samson L., Snoke, Arthur W., and Palmer, Allison R., 1983, Confirmation of the Carolina Slate Belt as an Exotic Terrane: Science, New Series, v. 221, p. 649–651.

Smith R., 2010, Airborn electromagnetic methods: applications to minerals, water and hydrocarbon exploration. CSEG recorder, V. 35 No. 03.

Snider J., Patterson E., Gochnour L., Marek J., and Burkhalter C., 2014, Haile Gold Mine Project, NI 43-101 Technical Report.

Snoke, A., Secor,T., Jr., and Metzgar, C., 1977, Batesburg-Edgefield catalastic zone—a fundamental tectonic boundary in the South Carolina Piedmont: Geological Society of America Abs. with Programs, v. 9, no. 2, p. 185-186.

Sørensen, K., Christiansen, A., and esben Auken, E.,(n.d) the transient electromagnetic method (tem). Retrieved February 22, 2017, from https://www.liag hannover.de/fileadmin/user_upload/dokumente/Grundwassersysteme/BURVAL/uch/065-076.pdf

Spector, A., and Grant, F. S., 1970, Statistical models for interpretation of aeromagntic data, Geophysics, 35: 293 - 302.

Stewart, T., 1981, Evaluation of Electromagnetic Methods for Rapid Mapping of Salt Water Interfaces in Coastal Aquifers

Telford, W. M., and Geldart, L. P., Sheriff, R. E. and Keys, D. A., 1976, Applied Geophysics, Cambridge University Press.

Telford, W.M., Geldart, L.P., Sheriff, R.E., 1990, Applied Geophysics Second Edition, Cambridge University Press, New York, 744 p.

Thompson, D. T., 1982, EULDPH: A new technique for making computer-assisted depth estimates from magnetic data. Geophysics, 47(1), 31–37. https://doi.org/10.1190/1.1441278

www.manaraa.com

Thurston, J. B., and Smith, R. S., 1997, Automatic conversion of magnetic data to depth, dip, and susceptibility contrast using the SPI ™ method. GEOPHYSICS, 62(3), 807–813.

Tuten, T., 2013, Geophysical Model of Granite Intrusives Surrounding the Haile Gold Mine, Lancaster County, SC using high resolution gravity data, bachelor's thesis, University of South Carolina, Columbia.

Verduzco, B., Fairhead, J. D., Green, C. M., MacKenzie, C., 2004, New insights into magnetic derivatives for structural mapping: The Leading Edge, 23, 116–119.

Whitehead, N., 2010, montaj Grav/Mag Interpretation, tutorial and user guide, Geosoft Incorporated

Whitenhead, N., and Musselman, C., 2011, Montaj MAGMAP filtering, Geosoft Incorporated.

Wright, P.M., 1981, Gravity and magnetic methods in mineral exploration, in Skinner, B.J., ed., Economic Geology, 75th Anniversary volume, p. 829-839

www.manaraa.com

APPENDIX A: THE COSTAL PLAIN AND DIKES DISTRIBUTION IN SOUTH CAROLINA.

The Atlantic coastal plain sediments extend from North Carolina to Alabama. Based on well data, the coastal plain increases in thickness to the southeast (A.1). Based on the magnetic map, Jurassic dikes are oriented northwest-southeast and north-south (A.2).

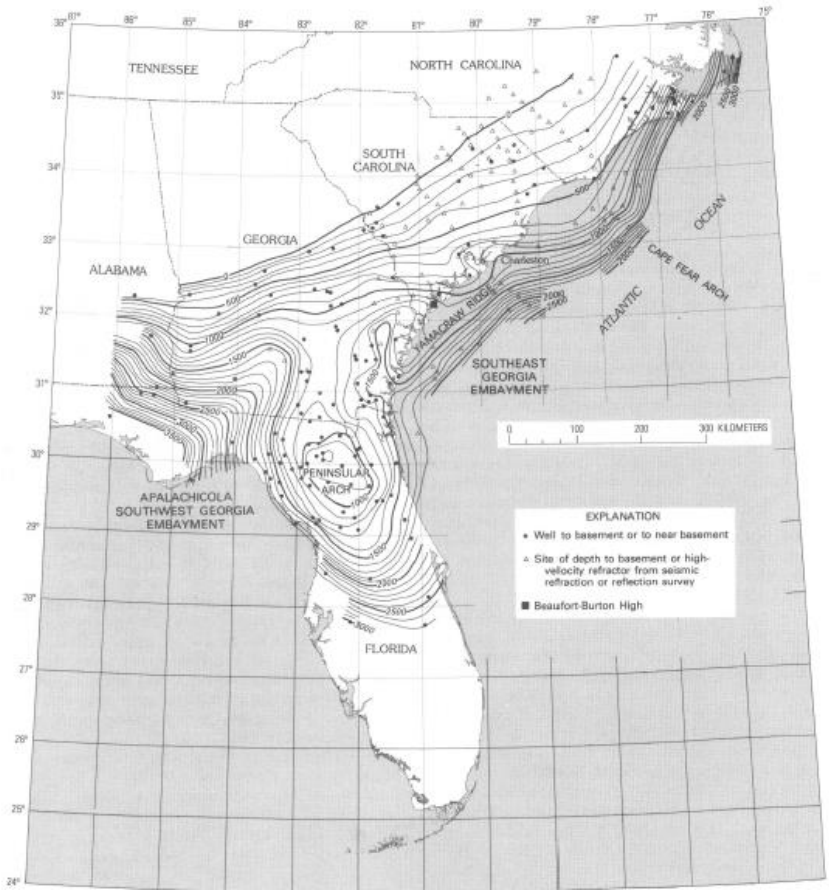

Figure A.1: Coastal plain thickness map, from Popenoe and Zietz (1977).

www.manaraa.com

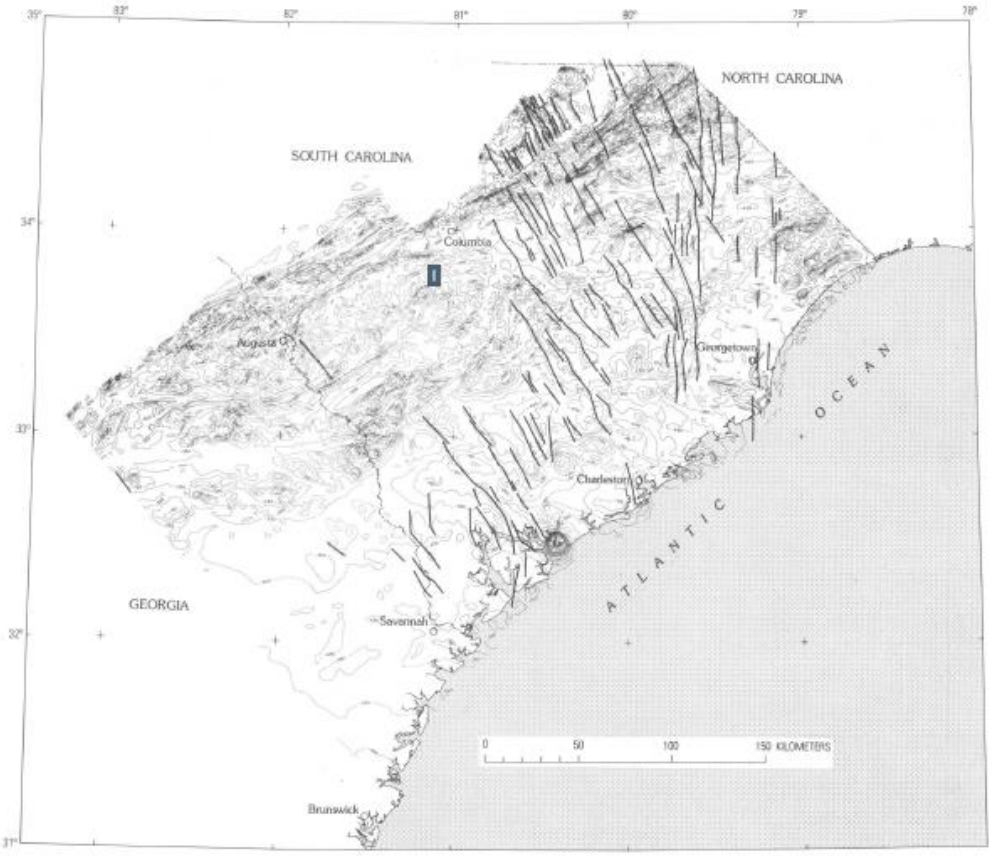

Figure A.2: Dike distribution map, from Popenoe and Zietz (1977).

www.manaraa.com

APPENDIX B: STATISTICS REPORT OF THE SOURCE PARAMETER IMAGE METHOD.

The source parameter image depth estimate results are independent of the magnetic inclination, declination, dip, strike and any remanent magnetization. The statistic report of the SPI of the Bouguer (figure B.1) shows that the source depths range from 101 to 28965 m. The gravity SPI results are close to the average depth results of the power spectrum: 0.1 to 2 Km. The magnetic SPI results (figure B.2) show the source depths range from 8 to 1189 m. The magnetic power spectrum source depth results are similar: 100 to 1000 m.

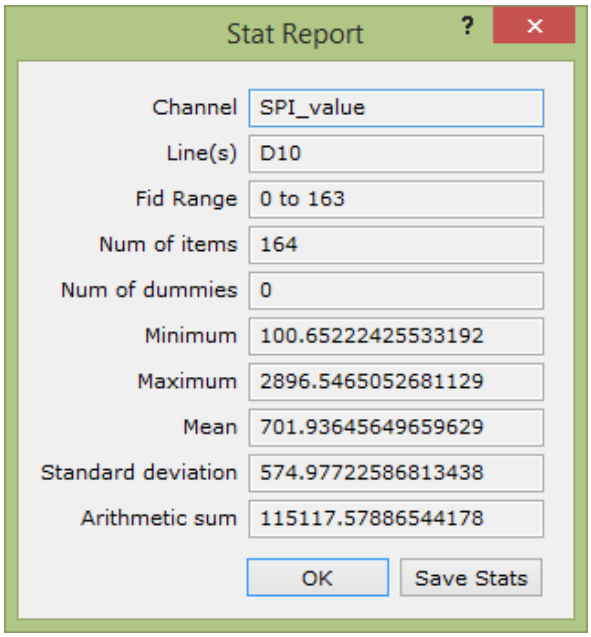

Figure B.1: SPI statistic report of Bouguer gravity.

www.manaraa.com

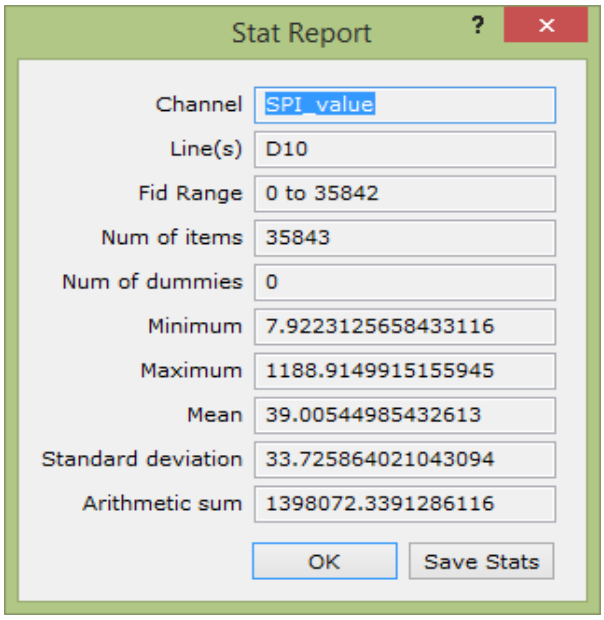

Figure B.2: SPI statistic report of Magnetic.

www.manaraa.com

APPENDIX C: EXPANDED VIEW OF THE CENTRAL PART OF THE STUDY AREA.

The ENE trend that was highlighted by the RTP method is shown in Figure C.1. The ENE trend in the central part of the study area is clearly visible on the TDR, EM, AS, and shaded relief maps. A is the TMI map. B is the EM conductivity map. C is the shaded relief map. D is the TDR of the RTP map. E is the AS of the TMI.

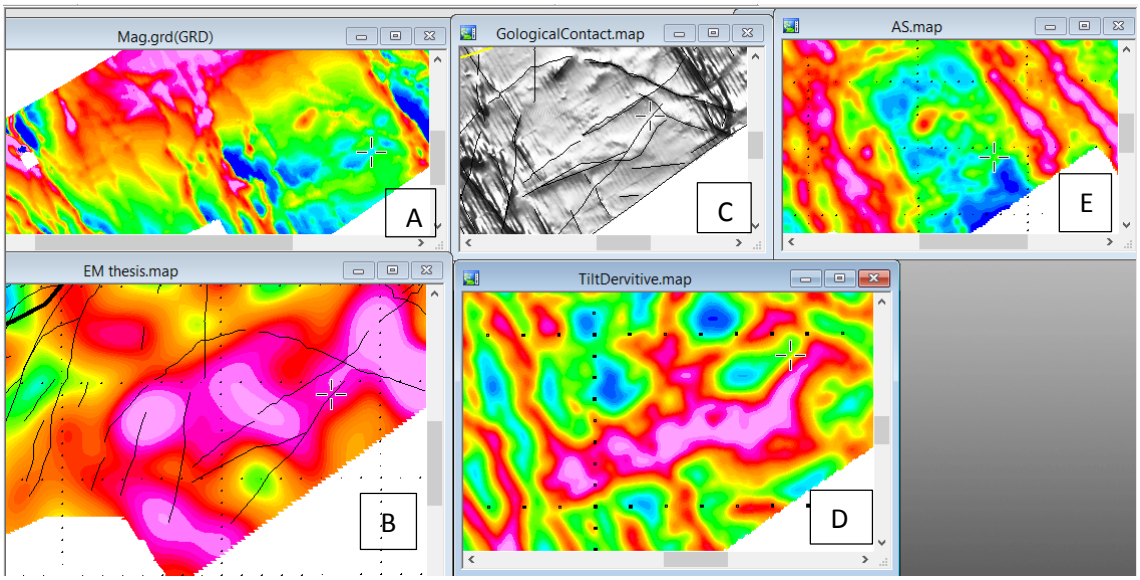

Figure C.1: Expanded view of the central part of the study area. The plus tag indicates the location control point. In B the point is located on a NE conductivity trend possibly located between two faults. This point shows a low TMI and higher signal on the RTP, tilt derivative, and AS.

www.manaraa.com

APPENDIX D: EULER DECONVOLUTION TO ESTIMATE THE SOURCE DEPTHS FOR MAGNETIC AND GRAVITY ANOMALIES.

The Euler Deconvolution (ED) method was applied to the total magnetic intensity and Bouguer maps. Structural indexes of 0, 0.5, 1, 2, and 3 were applied to represent contacts/faults, sill, dike, step, pipes, and spherical sources. The Euler Deconvolution solutions of the Bouguer gravity field (figure D.1) follows the TDR. The Euler Deconvolution solutions for the magnetic field (figure D.2) with a structural index of 0.5 is represent a contact/fault model follow the Jurassic and Alleghanian dikes. The Euler Deconvolution solutions for a structural index of 1 (figure D.3) follow Jurassic dikes and the Pageland granite. For the dikes and sills depths range between 0 - 858 m below sea level. The Euler Deconvolution solutions for pipe sources (figure D.4) show depths ranging between 500 – 1346 m below sea level. The Euler Deconvolution solutions for a spherical model (figure D.5) clearly show the Pageland granite contact as well as dikes. Most of the solutions are less than 500 m below sea level.

www.manaraa.com

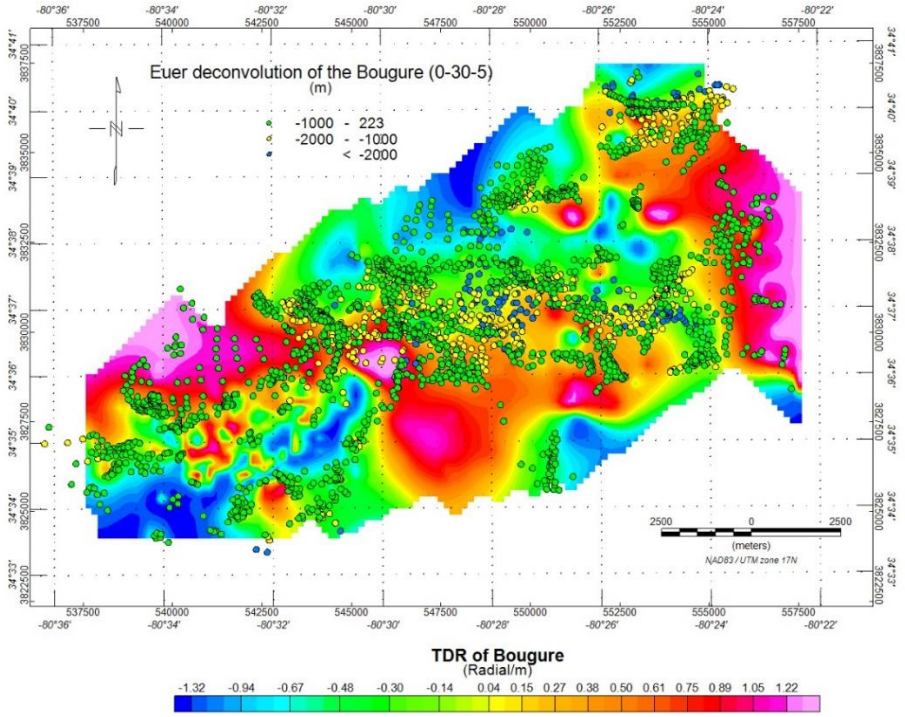

Figure D.1: The ED solutions for the gravity field superimposed on the TDR. The SI is 0 which represents a sill/dike/step. The window size is 30. The results of the ED method follow the positive TDR. The green color indicates depths ranging between 223 and 1000 m below sea level.

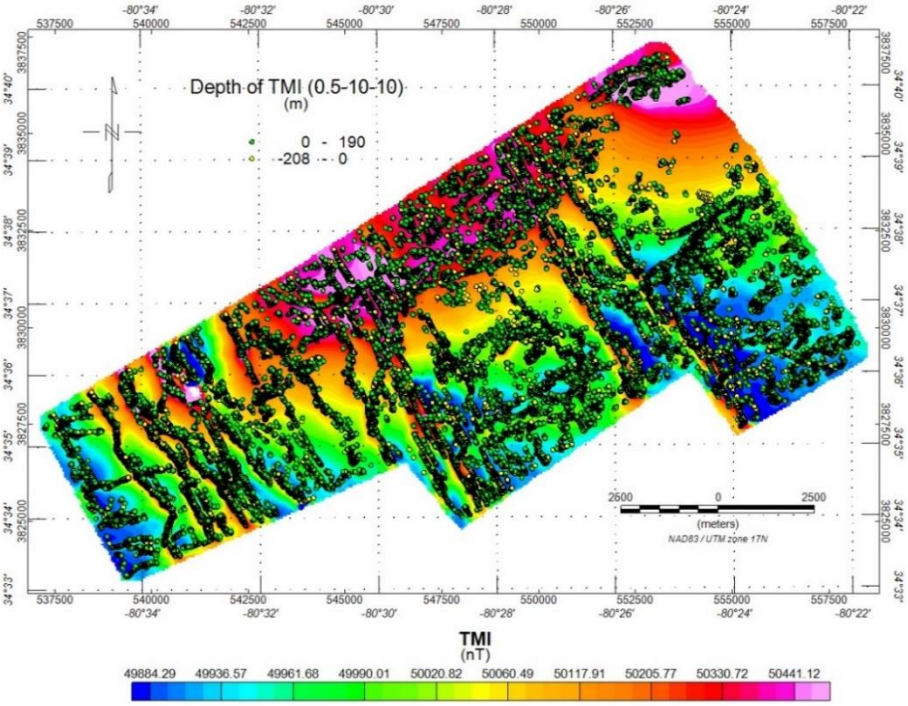

Figure D.2: The ED solutions plotted on the TMI map. The window size is 10. SI is 0.5.

www.manaraa.com

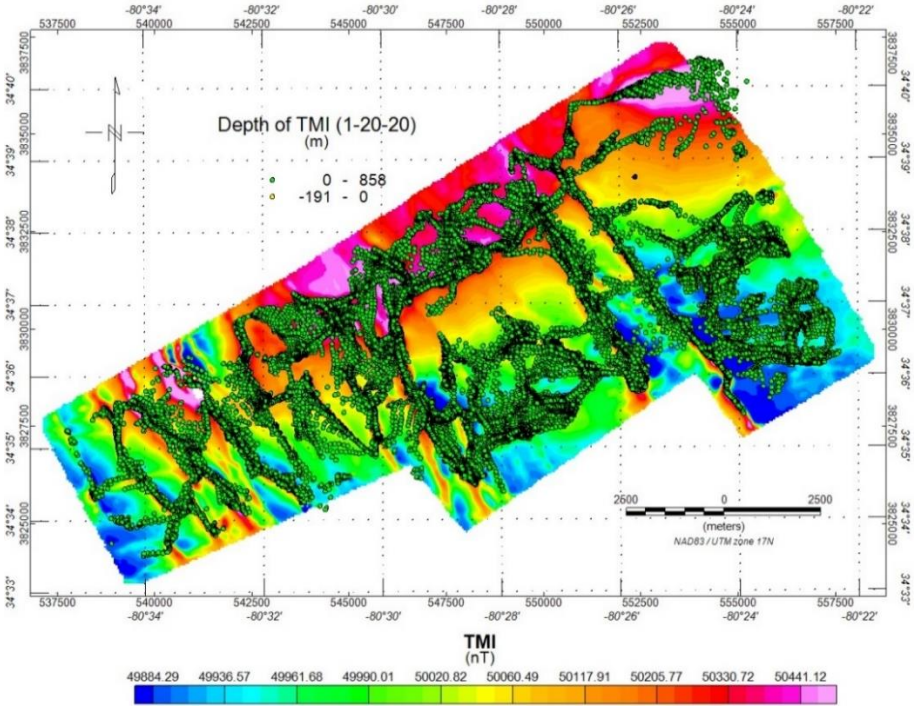

Figure D.3: The Euler deconvolution solutions plotted on the TMI map. The window size is 20. The SI is 1.

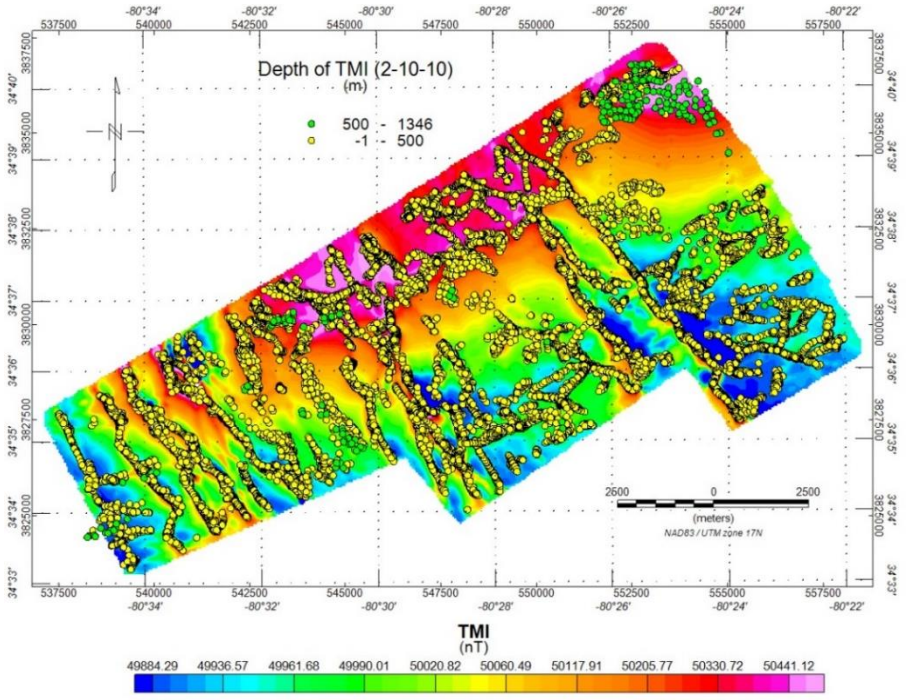

Figure D.4: The Euler deconvolution solutions plotted on the TMI map. The window size is 10. The SI is 2.

www.manaraa.com

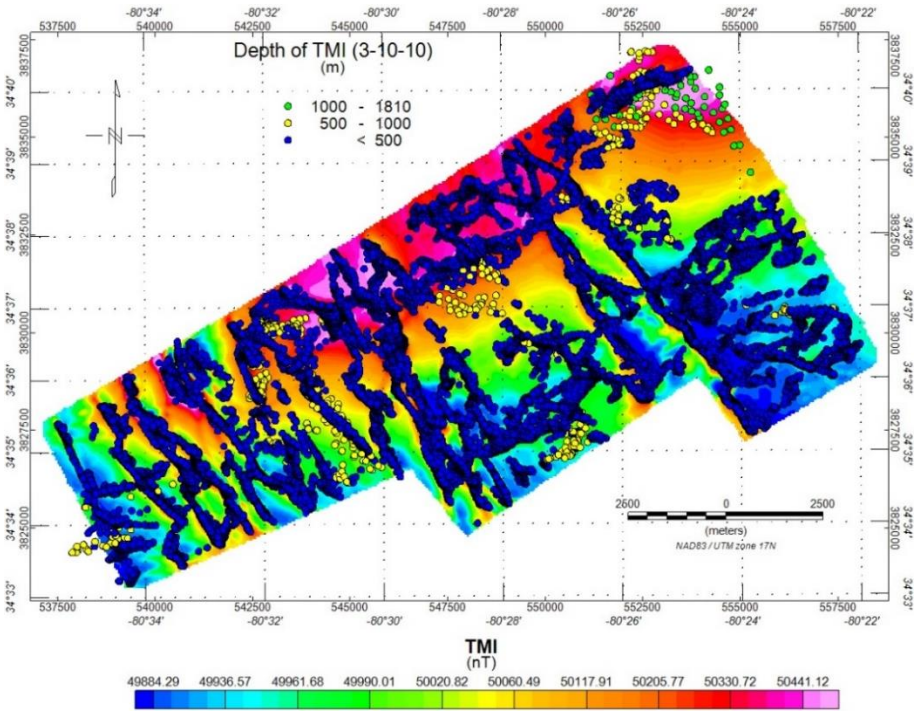

Figure D.5: The Euler deconvolution solutions plotted on the TMI map. The window size is 10. The SI is 3.

www.manaraa.com